

Nuclear magnetic resonance on laboratory and field scale for estimating hydraulic parameters in the vadose zone

vorgelegt von
Diplomingenieur für Angewandte Geophysik
Stephan Costabel
aus Rostock

von der Fakultät VI - Planen Bauen Umwelt
der Technischen Universität Berlin
zur Erlangung des akademischen Grades

Doktor der Naturwissenschaften
- Dr. rer. nat. -

genehmigte Dissertation

Promotionsausschuss:

Vorsitzender: Prof. Dr. U. Tröger

Berichter: Prof. Dr. U. Yaramanci

Berichter: Prof. Dr. G. Wessolek

Berichter: Prof. Dr. R. Knight (Stanford University, USA)

Tag der wissenschaftlichen Aussprache: 9. Dezember 2011

Berlin 2011
D83

Abstract

The method of nuclear magnetic resonance (NMR) is sensitive to water-filled pores and to pore-space properties, respectively. Geophysical NMR applications allow for estimating water content and saturated hydraulic conductivity on laboratory and field scale, as well as the pore size distribution (PSD) on laboratory scale. Thus, these applications are expected to have also a great potential for estimating effective hydraulic parameters in the vadose zone. This potential is investigated and assessed in this work on the laboratory and on the field scale, respectively. The theoretical analysis of the underlying mathematical-physical concepts describing the NMR relaxation phenomenon in simple pore geometries shows that the relaxation characteristics of partially saturated pores significantly depends on the assumption how the remaining pore water is kept in the pore during the desaturation. On the laboratory scale, NMR measurements with artificial and natural soil samples were conducted to test the reliability of the NMR-based PSD to be an estimate of the water retention curve (WRC). It is shown that this estimation is only possible for samples with clay contents smaller than approximately 10%. NMR methods are sensitive to the pore bodies, which is contrary to the pore-throat sensitivity of conventional WRC measurements and leads thus to an increasing difference between NMR-PSDs and WRCs with increasing clay content. It must be concluded that a plausible estimation of hydraulic parameters from the NMR-PSD is possible for sandy soils only. Based on the well known Brooks-Corey model, an empirical approach is developed, which relates the relative relaxation time at partial saturation to the relative hydraulic conductivity K_{rel} , i.e., the ratio of the unsaturated and the saturated conductivities. This approach is verified in the laboratory for T_2 measurements with conventional NMR and, in a modified form, for T_2^* measurements with earth's field NMR, respectively. The estimation of K_{rel} from T_2^* can, in principle, also be adapted for the field application of NMR, the magnetic resonance sounding method (MRS), which is shown with a field example. However, this approach still exhibits conceptional and technical limitation and must be investigated further. As alternative, an additional inversion approach for MRS is introduced, which uses only the NMR signal amplitudes and parameterizes directly the capillary fringe in the subsurface by using the Brooks-Corey model. A further MRS field example shows that this approach also allows for a plausible prediction of K_{rel} under the assumption that the capillary fringe is in a state of equilibrium.

Zusammenfassung

Die Methode der Kernspinresonanz (Nuclear Magnetic Resonance - NMR) ermöglicht die Analyse des wassergefüllten Porenraumes. Geophysikalische NMR-Verfahren erlauben die Abschätzung des Wassergehaltes und der gesättigten hydraulischen Leitfähigkeit des Porenraumes im Labor- und Feldmaßstab sowie die Porengrößenverteilung (PGV) im Labormaßstab. Es ist zu erwarten, dass diese Verfahren ebenso zur Abschätzung effektiver hydraulischer Parameter in der vadosen Zone potentiell geeignet sind. In der vorliegenden Arbeit wird dieses Potenzial auf Labor- und Feldskala untersucht und bewertet. Auf der Grundlage einfacher Porenmodelle, für die das mathematisch-physikalische Problem der NMR-Relaxation analytisch gelöst werden kann, wird der Zusammenhang zwischen Relaxationszeit und Sättigungsgrad des Porenraumes untersucht. Es zeigt sich dabei, dass die Annahme darüber, wie das Restwasser im Porenraum gebunden ist, die Relaxationscharakteristik entscheidend beeinflusst. Im Labormaßstab wurde anhand künstlicher und natürlicher Proben getestet, ob die NMR-basierte PGV eine Abschätzung der Wasserretentionsfunktion (WRF) darstellt. Es wird gezeigt, dass die Übereinstimmung von NMR-PGV und WRF nur für Lockersedimente mit einem Tonanteil von weniger als 10% gültig ist. Die bevorzugte Empfindlichkeit der NMR-Methode für die Porenbäume sorgt für eine mit dem Tonanteil zunehmende Abweichung im Vergleich zu konventionellen WRF Messungen, welche ihrerseits auf Porenhäule sensitiv sind. Eine glaubwürdige Abschätzung hydraulischer Parameter aus NMR-PGVs ist also nur für sandige Böden möglich. Auf der Grundlage des gut bekannten Brooks-Corey-Modells wird ein empirischer Ansatz entwickelt, der die relative Relaxationszeit bei Teilsättigung mit der relativen hydraulischen Leitfähigkeit K_{rel} (Verhältnis aus ungesättigter und gesättigter Leitfähigkeit) verknüpft. Dieser Ansatz wird mithilfe konventioneller Labor-NMR durch T_2 Messungen und in modifizierter Form für T_2^* Messungen im Erdmagnetfeld bestätigt. Die Abschätzung von K_{rel} aus T_2^* Messungen kann im Prinzip für die NMR-Feldanwendung, also für Magnetische Resonanz Sondierungen (MRS), adaptiert werden, was an einem Feldbeispiel gezeigt wird. Allerdings hat die praktische Anwendung dieses Ansatzes im Feldmaßstab noch technische und konzeptionelle Grenzen und muss in zukünftiger Forschungsarbeit weiter untersucht werden. Alternativ dazu wird ein neues Inversionsverfahren für die MRS-Methode eingeführt, welches ausschließlich die NMR-Amplituden benutzt und direkt den kapillaren Aufstieg mithilfe des Brooks-Corey-Modells parametrisiert. Ein weiteres Feldbeispiel zeigt, dass auch dieser Ansatz unter der Voraussetzung, dass der Kapillarraum im Gleichgewicht ist, eine plausible Abschätzung von K_{rel} erlaubt.

Contents

1	Introduction	1
2	Soil physical basics	4
2.1	Water dynamics in the vadose zone	4
2.2	Capillary pressure and water retention	5
2.3	Water retention models and unsaturated hydraulic conductivity	7
2.4	Water retention curve (WRC) estimation from soil texture	10
3	Basics of nuclear magnetic resonance	12
3.1	The NMR phenomenon	12
3.1.1	Nuclear magnetization	12
3.1.2	Longitudinal and transverse NMR relaxation	13
3.2	NMR relaxation in restricted environments	17
3.2.1	Analytical solutions for simple pore geometry	17
3.2.2	General relations between NMR and pore space properties	21
3.2.3	Multi-exponential relaxation - NMR data approximation	25
3.3	NMR on field scale - magnetic resonance sounding (MRS)	27

4	NMR relaxation in partially saturated pores	29
4.1	Theoretical considerations for simple pore geometries	29
4.1.1	NMR saturation degree	29
4.1.2	Analytical solutions for planar, cylindrical, and spherical cases . .	30
4.1.3	NMR response of partially saturated angular pores	33
4.2	Data examples with mono-exponential NMR response	38
4.3	Adaptation of the Brooks-Corey model	41
5	Estimation of WRC parameters from NMR on the laboratory scale	43
5.1	Pore size distribution from NMR compared with differential WRC	43
5.2	Assessment of conventional WRC estimation for artificial samples	46
5.2.1	Material and methods	46
5.2.2	Water retention parameters in dependency on clay content	47
5.2.3	Correlation of VG and BC parameters	50
5.2.4	Comparison of WRC measurements and estimations by ROSETTA	50
5.3	WRC estimation from NMR relaxation time distribution at saturation . .	52
5.3.1	Material and methods	52
5.3.2	Dependency of T_1 and T_2 distributions on matric potential	58
5.3.3	Comparison of WRC predictions from NMR and ROSETTA . . .	62
5.4	Discussions and conclusions	67
6	Column experiments - K_{rel} estimation with earth's field NMR	69
6.1	Material and methods	70
6.1.1	Sample characterization and NMR data acquisition	70
6.1.2	Time step inversion	73
6.1.3	Brooks-Corey parameterization of the capillary fringe	74
6.1.4	Hydraulic parameters from drainage experiments	74
6.2	Results and interpretation	76
6.2.1	Estimation of the residual water content with NMR	76

6.2.2	Test of the inversion schemes with synthetic data	77
6.2.3	Dependency of T_2 and T_2^* from the saturation degree	79
6.2.4	Prediction of K_U from T_2 and T_2^* at partial saturation	84
6.2.5	Prediction of K_U from capillary fringe parameterization	84
6.3	Discussions and conclusions	87
7	MRS with focus on the vadose zone - on <i>in situ</i> K_{rel} prediction	91
7.1	Adaptation of laboratory interpretation schemes for field strategies	91
7.2	K_{rel} estimation from T_2^*	93
7.2.1	Blocky time step inversion with fixed groundwater table	93
7.2.2	Real data example from test field Haldensleben	94
7.3	K_{rel} estimation based on parameterization of the capillary fringe	100
7.3.1	MRS inversion based on Brooks-Corey parameterization	100
7.3.2	Feasibility study with synthetic data	100
7.3.3	Real data example from test field Nauen	108
7.4	Discussions and conclusions	114
8	Conclusions	116
	Bibliography	119
	Acknowledgements	127
	Appendices	129
A		130
B		139

Dedicated
to my sons Ciaro and Lucian,
little fellows, but strong characters
and great researchers!

Please do never stop asking 'Why'!

Chapter 1

Introduction

Hydrogeological objectives such as ground water recharge and ground water protection are directly linked to water and solute transport processes in the vadose zone. Thereby, the vadose zone acts as a natural buffer between the surface and the groundwater reservoir in the subsurface, and its hydraulic characterization and assessment is of particular interest. Usually, in hydrogeology and soil sciences the vadose zone can only be investigated by laboratory measurements at small samples with dimensions of a few cm^3 from wells or diggings (detailed explanations in Chapter 2). A successful upscaling of the laboratory results to the field scale and a corresponding prediction of flow and transport processes depends on the number of the samples, on their quality, and on the extent of the natural heterogeneity at the site of investigation. To have a direct look at the involved dynamic processes on larger spatial scales, monitoring strategies are an adequate choice. However, such methods can be applied for scientific purposes only, because great effort must be undertaken, e.g., the preparation of lysimeters or the installation of tensiometers in the field. In any case, all these strategies demand invasive operations, which may change and disturb the natural structure of the material to be investigated.

Geophysical field methods are noninvasive or, at least, minimum-invasive, and their application for the characterization of the vadose zone is very desirable. However, so far, geophysical methods that directly provide effective hydraulic parameters in the unsaturated zone and their spatial distribution have not been developed. Recent research activities focussing the application of water-sensitive geophysical methods for investigations in the vadose zone concentrate on monitoring strategies (Rucker and Ferre, 2004; Kowalsky et al., 2005; Hinnell et al., 2010). In principle, such methods can provide estimates of hydraulic parameters, but only in an indirect manner: Methods such as electrical resistivity tomography (ERT) and ground penetrating radar (GPR) allow the observation of water content changes by measuring the corresponding effects on the electrical conductivity (ERT) and on the dielectric permittivity (GPR). But these measurement parameters significantly depend also on additional structural parameters, which may lead to a large extent of non-uniqueness in practice.

Geophysical applications of the nuclear magnetic resonance (NMR) method have the advantage to measure the water content directly. As described in Chapter 3, these applications are available on the laboratory and on the field scale, respectively. Conventional NMR methods (in lab and in boreholes) use artificial permanent magnetic fields with a strength of about 0.050 up to 100 Tesla. Beside the water content, they also provide estimates of the hydraulic conductivity (K_S) and the pore size distribution (PSD) from the NMR relaxation data of the saturated material (Coates et al., 1999; Dunn et al., 2002). The field application of NMR, the magnetic resonance sounding method (MRS), works the earth's magnetic field (about 20 to 50 μ Tesla). It is established for groundwater assessment (Yaramanci and Hertrich, 2006; Yaramanci and Müller-Petke, 2009), and, under ideal measurement conditions, it also allows for estimating K_S (Legchenko et al., 2002). Regarding the investigation of the vadose zone, NMR techniques are expected to have a great potential, on the laboratory scale (Bird et al., 2005; Ioannidis et al., 2006), as well as on the field scale (Lubczynski and Roy, 2003; Roy and Lubczynski, 2005).

So far, reliable strategies to estimate hydraulic parameters under unsaturated conditions from NMR data are not available, though the NMR relaxation behaviour encodes relevant information about the water filled pore space, even at partial saturation (Bird et al., 2005; Hertzog et al., 2007). In Chapter 4, analytical derivations for simple pore geometries are developed to analyze the principle behavior of the NMR relaxation time under partially saturated conditions. It is well known that a multi-exponential representation of NMR relaxation data measured in consolidated material in the laboratory and in boreholes can be correlated with capillary pressure curves (Kleinberg, 1996; Kenyon, 1997; Volokitin et al., 2001). Regarding the prediction of flow and transport processes in soils, the key is the soil water retention curve (WRC), which is a synonym of the term 'capillary pressure curve' (Kutilek and Nielson, 1994; Warrik, 2003). The correlation of multi-exponential NMR data of saturated soils and the WRC at the laboratory scale is an objective of this work. In Chapter 5 the potential of the NMR relaxation time distribution to be a plausible estimation of the WRC is investigated for natural and artificial samples.

Chen et al. (1994) proposed a formula to estimate the relative hydraulic conductivity K_{rel} from NMR relaxation times. K_{rel} is the ratio of the unsaturated (K_U) and saturated (K_S) conductivities. The approach of Chen et al. (1994) was verified for glass beads by Ioannidis et al. (2006). The key for an estimation of K_U from NMR relaxation data is the dependence of the relaxation times on the saturation degree S , which is still not fully understood. Mattea et al. (2004) showed a simple linear relationship for a wetting fluid phase in nano- and microporous silica glasses. However, the data of Ioannidis et al. (2006) show that this linear behavior can not be considered to be the general case. Thus, important objectives of this work (Chapter 6) are, on the one hand, to find models that describe the dependence of the NMR relaxation times on S at the laboratory scale (for conventional NMR and for earth's field NMR, respectively) and, on the other hand, to derive estimates of K_{rel} from these models.

The main objective of this work is to develop the basis of strategies to estimate K_{rel}

from MRS data. Below the groundwater table and under ideal noise conditions, MRS allows for estimating the spatial K_S distribution using the MRS relaxation times T_1 and T_2^* (Legchenko et al., 2002; Mohnke and Yaramanci, 2008). Roy and Lubczynski (2005) showed that determining the mobile water content in the vadose zone with MRS is possible. However, estimating the transport properties of partially saturated soils is still not solved. MRS measurements with a focus on the vadose zone are often an additional challenge due to the technical limitations of commercially available MRS equipment, such as long instrumental dead times and low signal-to-noise ratios (Roy and Lubczynski, 2005; Mohnke and Yaramanci, 2005). Recent MRS instrumentation improvements seems promising regarding this matter, e.g. decreased instrumental dead times and new noise compensation strategies (Walsh, 2008). In Chapter 7, two approaches for estimating K_{rel} from MRS data are suggested.

Chapter 2

Soil physical basics

Soil physical concepts try to solve the complicated problem of water transport in partially saturated loose sediments by introducing acceptable simplifications and by establishing effective model assumptions and parameters. This chapter gives an overview of basic measuring and interpreting techniques for soil physical parameters, as far as these are relevant for this work.

2.1 Water dynamics in the vadose zone

In general, the vadose zone is subdivided into three individual zones (Stephens, 1996), which are schematically depicted in Figure 2.1:

1. The root zone with increased water retention due to portions of organic matter and clay as alteration residues.
2. The intermediate zone with different fractions of residual and seepage water depending on the pore size distribution of the interbedded lithological units.
3. The capillary fringe with increasing water content up to saturation near the ground water table. The capillary rise depends on the pore size distribution.

The water dynamics under partially saturated conditions is primarily affected by capillary forces given as the potential of the pore space to retain the water in the pores. This potential is called the matric potential. It has to be taken into account when predicting the water transport characteristics in the vadose zone. In general, the spatial distribution of soil physical properties must be considered to be heterogeneous and anisotropic. Therefore, water flow in the vadose zone is actually a three-dimensional process. The natural consequences are phenomena such as preferential flow and interflow (Cullen et al.,

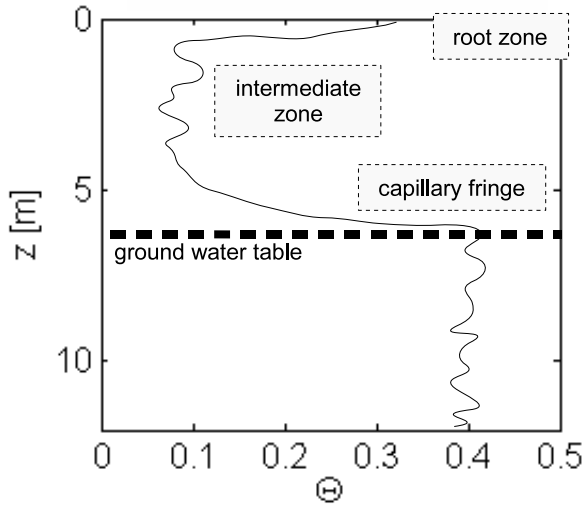


Figure 2.1: Characteristical water content distribution in the vadose zone.

1995; Wierenga, 1995; Steenhuis et al., 1995). However, in the most cases detailed *in situ* information about the subsurface structure is not available, and simplifications are needed when developing water flow models. Often, the flow modeling is concentrated only towards the vertical direction z , whereby the soil heterogeneity is accounted for by statistical considerations, and flow processes along x and y directions are interpreted as additional source and sink terms (Wierenga, 1995; Steenhuis et al., 1995).

The governing equation to describe water flow processes in vertical direction z under unsaturated conditions is given by the one-dimensional Richards equation (Warrik, 2003):

$$\frac{\partial \Theta(h)}{\partial h} \frac{\delta h}{\delta t} = \frac{\delta}{\delta z} \left[K_U(\Theta) \frac{\delta h}{\delta z} \right] - \frac{\delta K_U(\Theta)}{\delta z} + s \quad (2.1)$$

In general, the Richards equation is solved numerically by including as *a priori* the source term s and the water retention curve (WRC) that describes the volumetric water content Θ as a function of the matric pressure head h . The unsaturated hydraulic conductivity K_U as a function of Θ consequently depends on the WRC. Thus, the WRC can be considered as the key for predicting flow processes in the unsaturated pore system.

2.2 Capillary pressure and water retention

The matric pressure head h , also called capillary pressure head, is a suitable measure of the matric potential expressed as energy per unit weight, i.e., as units of length (Warrik, 2003; Kutilek and Nielson, 1994). In contrast to the hydraulic pressure head below the water table, the matric pressure head h is defined negatively to account for the suction

effect of the capillary forces against the gravity force. In a state of equilibrium, the absolute value of h corresponds to the height of the water rise above the water table. The soil pore space behaves like a bundle of capillaries, whereby h is associated with the reciprocal effective capillary radius r_{eff} (Warrik, 2003):

$$h = \frac{C}{r_{eff}}. \quad (2.2)$$

The proportionality parameter C includes the physical properties of the interface between the wetting fluid and the pore surface, such as the surface tension, contact angle, and fluid density. The smaller r_{eff} is, the higher the potential is for the capillary to retain the water. At a certain h all pores larger than the associated r_{eff} are empty, and the remaining water content is given by the water in the capillaries equal to or smaller than r_{eff} (Warrik, 2003).

In practice, the WRC can only be reconstructed in the laboratory using soil samples. Depending on the desired h range to be observed, either a pressure plate apparatus (Figure 2.2a), or a tension plate in combination with a 'hanging' water column (Figure 2.2b) can be used (Warrik, 2003; Kutilek and Nielson, 1994). The pressure plate apparatus provides an h spectrum ranging from about -100 to -15000 cm (equivalent to a pressure range of -10 kPa to -1.5 MPa). The samples are placed on a porous plate inside a pressure vessel. Both the samples and the porous plate are saturated at the beginning of the experiment. During the measurement a certain overpressure p_{in} is applied to the vessel and the samples begin to drain via the porous plate that is connected to an outlet with atmospheric pressure (p_{atm}). The pore size of the plate must be small enough to block any air entry into it.

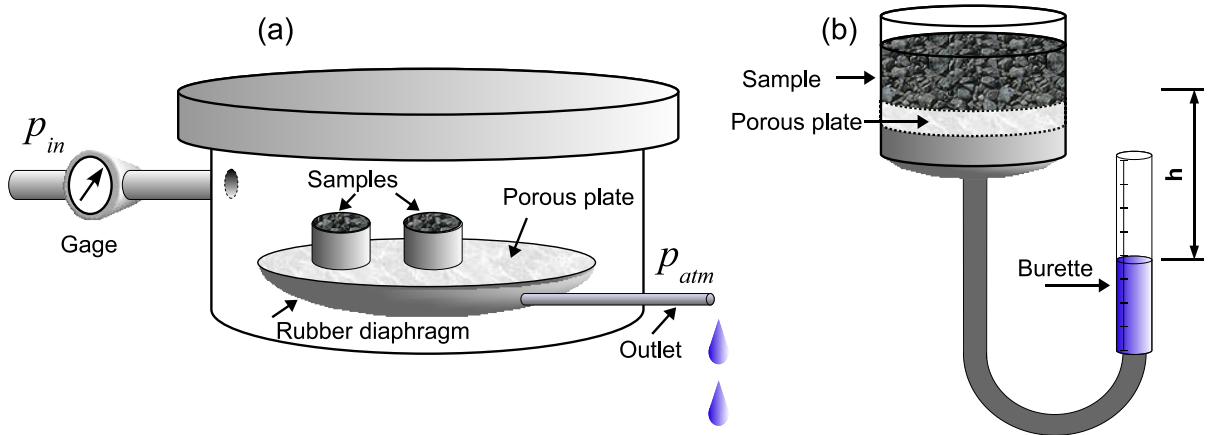


Figure 2.2: Experimental setup for measuring the WRC: (a) Pressure plate apparatus, (b) Hanging water column.

After reaching the equilibrium, which is achieved when no more water drops out of the outlet, the samples are weighed to determine the remaining water content. The absolute value of the capillary pressure that holds the remaining water content in the pores is equal to the value of the overpressure. In contrast to this principle, the method using the hanging water column works with underpressure, i.e., with tension (Figure 2.2b). The tension is applied quite simply by placing an outflow vessel, which is connected with the porous plate, at a certain depth beneath the sample. The sample begins to drain until the state of equilibrium is achieved. The corresponding capillary pressure equals the tension value, and the related water content is determined either by weighing the sample or by observing the water volume in the outflow. The advantage of this principle is to realize very small h values ranging from 0 to a few hundreds of cm depending on the experimental setup and on the height of the laboratory ceiling.

For *in situ* observations of the capillary pressure, tensiometers are used, which are installed in the field. However, because the water content is usually not available simultaneously, a reconstruction of the WRC is not possible in this way. The use of tensiometers in the laboratory can provide high resolved WRCs when combined with water content measurements (Schindler et al., 2010).

2.3 Water retention models and unsaturated hydraulic conductivity

Analytical WRC models are usually defined as functions of the effective water saturation S_E :

$$S_E = \frac{\Theta - \Theta_R}{\Theta_S - \Theta_R}, \quad (2.3)$$

where Θ is the volumetric water content, Θ_S is the water content at saturation, and Θ_R is the residual water content. The residual water content Θ_R is the fraction of the water in the smallest pores whose participation in any water transport processes is negligible. The shape of the WRC depends on various parameters, e.g., grain size distribution, bulk dry density, and contents of clay and organic matter (Vereecken, 1995; Saxton and Rawls, 2006). Assuming the capillary bundle model to characterize the pore space of the soil, one may intuitively understand the WRC as a cumulative pore size distribution. However, a strictly physical formulation of the WRC is very difficult. Thus, in soil physics empirical models are the common choice. An often used model for the WRC is the model of van Genuchten (1980), hereafter referred to as the VG model:

$$S_E = \left(\frac{1}{1 + |\alpha h|^n} \right)^m \quad (2.4)$$

The parameters α , n and m are empirical parameters that are found in practice by fitting WRC measurements. In the data base of Hammecker et al. (2004), the parameter n

ranges from 1.1 up to 8 and α ranges from about 0.0004 to 0.11 cm⁻¹. In most cases the relationship $m = 1 - 1/n$ is used, which is referred to as the constrained form (Peters and Durner, 2006). In general, m is positive and ranges up to 1.

Another frequently used model for the WRC is the model of Brooks and Corey (1964), hereafter abbreviated with BC. It describes the relationship of S_E and h as a simple power law:

$$S_E = \begin{cases} \left(\frac{h_0}{h}\right)^\lambda, & |h| > |h_0| \\ 1, & |h| \leq |h_0| \end{cases} \quad (2.5)$$

The governing parameter in this equation is the so-called pore-size-distribution (PSD) index λ , which is always positive and increases with increasing homogeneity of the pore space up to values of about 3 to 4 (Haverkamp et al., 2005). The critical pressure head h_0 represents the air-entry point: In equilibrium, the absolute value of h_0 corresponds to the height above the water table completely saturated with water. In general, h_0 is not identical to the water table $h = 0$. With Equation 2.2, the BC model can also be expressed as a function of r_{eff} :

$$S_E = \begin{cases} \left(\frac{r_{eff}}{r_0}\right)^\lambda, & |r_{eff}| < |r_0| \\ 1, & |r_{eff}| = |r_0| \end{cases} \quad (2.6)$$

In this case, r_0 represents the effective radius of the saturated medium. Once the WRC is parameterized, the relative hydraulic conductivity K_{rel} can be derived, that is, the ratio of the unsaturated (K_U) and the saturated conductivities (K_S). Van Genuchten (1980) suggested a K_{rel} approximation following Mualem (1976), which is often called the van-Genuchten-Mualem model (VGM model):

$$K_{rel} = \sqrt{S_E} \left[1 - \left(1 - S_E^{\frac{1}{m}} \right)^m \right]^2 \quad (2.7)$$

with $m = 1 - \frac{1}{n}$.

At the base of the BC model, K_{rel} is given with (Šimůnek and van Genuchten, 1999):

$$K_{rel} = \frac{K_U}{K_S} = S_E^{a + \frac{2}{\lambda}} \quad (2.8)$$

The parameter a is an empirical parameter depending on the tortuosity of the medium: in the literature a is given within the range of 2 to 4 (Šimůnek et al., 2009), and mostly it is set to 2.5 (Assouline and Tartakovsky, 2001; Zhu and Mohanty, 2002; Ioannidis et al., 2006).

Now, I want to investigate and compare characteristic relationships of the hydraulic parameters provided by these models. In Figure 2.3, the influence of the VG and BC

parameters on the shape of the WRC is shown. The WRCs are depicted as absolute values of the capillary pressure head ($|h|$) in cm on the y-axes versus saturation degree S on the x-axes. For both models, the parameter $S_R = \Theta_R/\Theta_S$ controls the asymptotic value for increasing absolute values of h . The parameters α (VG) and h_0 (BC) shift the whole WRC along the h axis. The third parameter, that is, $n = 1/(1 - m)$ in the case of the VG model (constrained form) and the PSD index λ in the case of the BC model, controls the slope of the WRC in the intermediate region between $S = 1$ and S_R . Obviously, the only characteristic difference between both models is the shape of the WRC closed to the air entry point, i.e., near the saturated region, whereas the general influence of the parameters on the curves is very similar. Regarding real WRC data, the BC model would be the better choice, if a sharp air entry point is observed, otherwise the VG model should be preferred. The VG model in the unconstrained form with m and n being independent parameters (see equation 2.4) also allows for increasing the sharpness of the air entry point. However, regarding possible ambiguities when estimating the WRC parameters the parameter space should be as small as possible, therefore the VG model in this work is solely used in the constrained form. In Chapter 5, the parameters of both models are directly compared to each other at the base of real WRC data from artificial sand-clay mixtures.

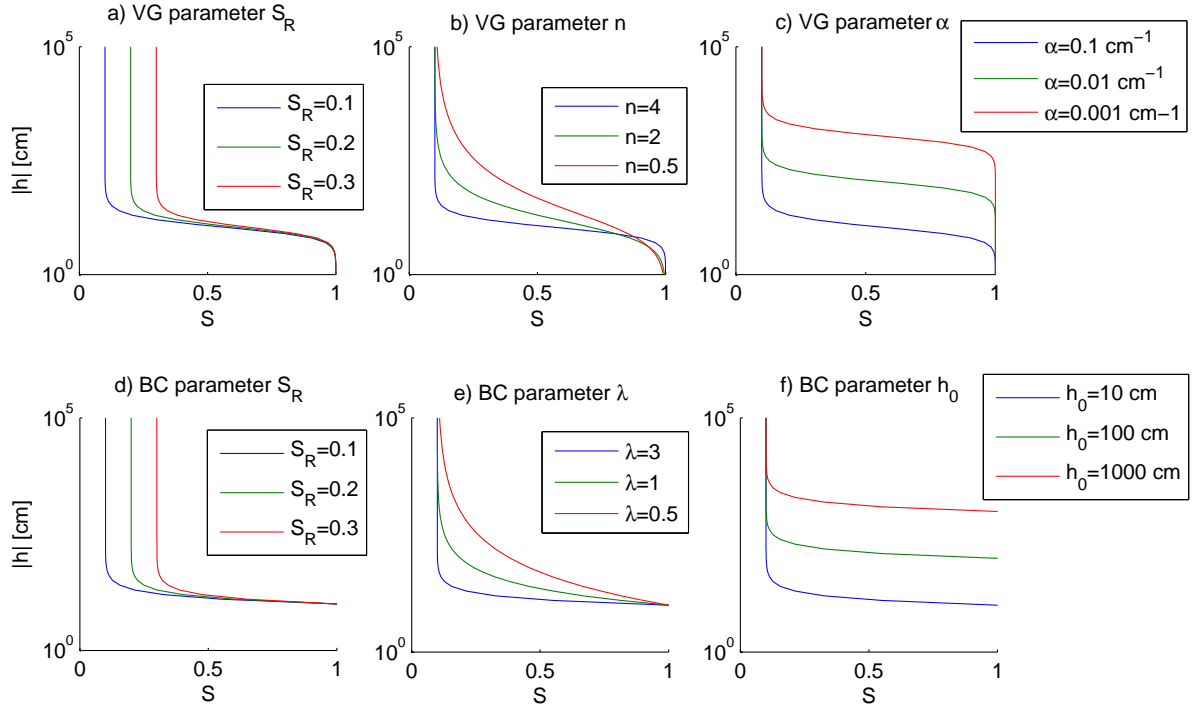


Figure 2.3: Example WRCs resulting from the parameterization following (a-c) van Genuchten (1980) and (d-f) Brooks and Corey (1964).

As alternatives to the WRC models introduced here, many others can be found in the literature, e.g., in Šimůnek et al. (2009), Peters and Durner (2006), and the references therein. However, almost all of these models are pure empirical models with an increased parameter space compared to the BC and VG models. Finally, for this work, I have chosen two simple but fundamental and widely used models to avoid unnecessary ambiguities due to a large number of parameters to be fitted during the NMR-based approaches introduced and discussed later. All examples studied in this work have quite simple WRCs complying with the VG and/or the BC model.

2.4 Water retention curve (WRC) estimation from soil texture

Usually, measurements of WRCs are very time consuming. Thus, in the past, many soil physical research activities were undertaken to estimate WRC parameters from texture data that can be analyzed much easier, i.e., the contents of clay, silt, sand, soil organic matter, and bulk dry density (Vereecken, 1995; Nemes et al., 2001; Wösten et al., 2001). These estimation methods, also called pedotransfer functions, are mostly based on statistical regression analysis using large datasets. A very popular database is the UNSODA database, which consists of broad texture and mineralogic information of soils from Northamerica and Europe (Leij et al., 1996).

In addition to the WRC measurements in this work, also the free software ROSETTA is used to predict WRC parameters. ROSETTA works with a neural network algorithm and predicts the VG parameters (equation 2.4), whereby the calibration of the neural network is based on the UNSODA database (Schaap et al., 2001). In the simplest case, the textural class of the soil of interest is accepted as input. If more textural information of the soil is available, the accuracy of the ROSETTA predictions is expected to increase. Table 2.1 shows an overview of the ROSETTA prediction models that are used in this work. Schaap et al. (2001) showed that the uncertainties of the ROSETTA prediction decrease with increasing number of input parameters, i.e., the model ROS-TH1500 is expected to provide the best results.

Table 2.1: Abbreviations of the ROSETTA prediction models used in this work.

Model	Sand	Silt	Clay	Bulk density	Θ at $h=-330$ cm (or $p_{in}=-33$ kPa)	Θ at $h=-15000$ cm (or $p_{in}=-1500$ kPa)
ROS-SSC	x	x	x	-	-	-
ROS-BD	x	x	x	x	-	-
ROS-TH33	x	x	x	x	x	-
ROS-TH1500	x	x	x	x	x	x

A study on the plausibility of ROSETTA predictions is conducted and introduced in Chapter 5. The VG parameters predicted by ROSETTA are used in this work to test the plausibility of the VG parameters estimated by NMR. In principle, ROSETTA allows also for predictions of K_{rel} and K_U . These parameters should be preferred for the direct comparison with NMR parameters, because the main objective of this study is the estimation of K_U with NMR. However, Schaap et al. (2001) investigated the uncertainties of the ROSETTA prediction using the UNSODA database and showed that the uncertainty interval of the hydraulic conductivity prediction is about one order of magnitude. With this uncertainty range the ROSETTA predictions for K_U are not adequate to provide reference values for assessing the NMR-based estimations.

Chapter 3

Basics of nuclear magnetic resonance

Proton NMR techniques are well established in geophysics, in particular in the hydrocarbon exploration. For the use of proton NMR methods for groundwater-exploration purposes, the measuring and interpreting schemes can, in principle, directly be adapted. This chapter introduces the NMR relaxation phenomenon and its mathematical-physical description. Thereby, the behavior of excited proton spins in porous media is, of course, of special interest, because this behavior is the basis for the unique and beneficial properties of NMR techniques among other geophysical methods. The underlying basic processing methods to interpret NMR relaxation data with the focus on the pore space properties are described, as far as they are relevant for this work. Finally, the field application of NMR, which allows for a completely non-invasive investigation of the subsurface, is introduced.

3.1 The NMR phenomenon

3.1.1 Nuclear magnetization

Hydrogeophysical NMR methods are based on the fact that the ^1H protons in water molecules have a magnetic dipole moment caused by their nuclear spin angular momentum. In a static magnetic field \vec{H}_0 the nuclear spins align with \vec{H}_0 , which results in an additional macroscopic magnetization \vec{M} that amplifies \vec{H}_0 . A secondary magnetic field \vec{H}_1 forces the spins and, consequently, \vec{M} to tilt away from their equilibrium positions. After terminating the secondary field, \vec{M} precesses around $\vec{H}_0 = (H_x, H_y, H_z)^T$:

$$\frac{\delta}{\delta t} \vec{M}(t) = \vec{M}(t) \times \gamma(\vec{H}_0). \quad (3.1)$$

When considering ^1H proton spins, the gyromagnetic ratio γ is 0.267518 Hz/nT. The coordinate system is defined by convention such that the z-direction equals the direction of \vec{H}_0 , i.e., $H_x=H_y=0$. The precessing frequency is the Larmor frequency $\omega_L = 2\pi f_L$, which linearly depends on $H_0 = |\vec{H}_0|$:

$$\omega_L = \gamma H_0. \quad (3.2)$$

After transforming Equation 3.1 into the so-called rotating frame (Torrey, 1949; Hahn, 1950), which is a coordinate system rotating with $\omega_L = \gamma H_0$ around the z-direction, the solution of Equation 3.1 gives a stationary \vec{M} . This transformation significantly simplifies all following equations.

For the excitation of the spin system, \vec{H}_1 is applied as an oscillating field for a certain duration τ_p , which is referred to as the energizing radiofrequency (rf) pulse. Its frequency equals ω_L to fulfill the resonant condition of the spin system. During the excitation, the spins and, consequently, \vec{M} are affected by the superposition of both fields \vec{H}_0 and \vec{H}_1 :

$$\frac{\delta}{\delta t} \vec{M}(t) = \vec{M}(t) \times \gamma(\vec{H}_0 + \vec{H}_1). \quad (3.3)$$

By solving Equation 3.3 by means of the rotating frame, one can show that the flip angle θ , which is the angle of \vec{M} with respect to \vec{H}_0 , depends on (Levitt, 2002):

$$\theta = \omega_L \tau_p = \gamma |H_1| \tau_p. \quad (3.4)$$

Normally, in conventional laboratory NMR relaxometry, flip angles of 90° and 180° are applied, and the corresponding pulses are referred to as the 90° -pulse and the 180° -pulse, respectively.

It should be noted that the magnitude of \vec{M} is too small compared with H_0 , so that it cannot be measured directly. However, the precessing movement of \vec{M} around \vec{H}_0 induces a measurable voltage in a receiver coil, whereby only components perpendicular to \vec{H}_0 are detected. Thus, in conventional laboratory NMR devices the axis of the receiver coil is installed perpendicular to \vec{H}_0 , so that the maximum signal is induced from the x-y-plane, i.e., after the application of a 90° -pulse.

3.1.2 Longitudinal and transverse NMR relaxation

In this section, the effect of relaxation is taken into account. In Equations 3.1 and 3.3, an unlimited precession of the nuclear magnetization \vec{M} was considered. Actually, the precession of \vec{M} around \vec{H}_0 is damped by interactions of the spins that cause an energy exchange, and thus, force the whole system to get back to its equilibrium state. This effect is called relaxation. Regarding the NMR response of fluids, e.g., water or oil, two energy exchange processes and, consequently, two different kinds of relaxation are considered (Bloch, 1946):

- **The thermal energy exchange of the spins with their environment:** After the excitation of the spin system by the rf-pulse, a part of the induced energy is transformed to thermal energy, i.e., to kinetic energy of the surrounding atoms. Because this effect can also be observed in solid materials, where the precessing spins exchange their energy with the atomic lattice, the corresponding effect on \vec{M} is called spin-lattice relaxation. A synonym for it is also the term 'longitudinal' relaxation, because it is the only damping effect observed for the z-component of \vec{M} .
- **The energy exchange between the precessing spins:** Internuclear interactions between the precessing spins, i.e., between their magnetic moments, lead to perturbations of the precession movement. This feature solely affects the x- and y-components of \vec{M} , and the total energy of the entire spin system remains unchanged. The corresponding effect is called transverse relaxation or spin-spin relaxation. There may be some other features having a similar phenomenological effect on the transverse component of \vec{M} . Irregular inhomogeneities of H_0 on the molecular scale and the presence of paramagnetic ions inside the system cause additional magnetic moments interacting with the observed spin system. It is quite difficult or even impossible to differentiate between these effects and thus, all of them are phenomenologically considered in the process of transverse relaxation. Because the transverse components of \vec{M} are also affected by the thermal exchange, the transverse relaxation rate is always faster in comparison to the longitudinal one when compared for the same material.

The effects discussed above can be explained in detail only by quantum-mechanical models, which, however, have not necessarily to be accounted for when describing their principle influence on the nuclear magnetization phenomenon. The general evolution of the magnetization vector \vec{M} with time is satisfyingly described, if Equation 3.3 is extended by components introducing the relaxation and diffusion effects following Bloch (1946) and Torrey (1949):

$$\frac{\delta}{\delta t} \vec{M}(t) = \vec{M}(t) \times \gamma(\vec{H}_0 + \vec{H}_1(t)) - \begin{pmatrix} M_x(t)/T_2 \\ M_y(t)/T_2 \\ (M_z(t) - M_0)/T_1 \end{pmatrix} + D \nabla^2 \vec{M}(t) \quad (3.5)$$

with

- T_2 - transverse relaxation time
- T_1 - longitudinal relaxation time
- M_0 - magnitude of the nuclear magnetization
- D - diffusivity.

The last term of Equation 3.5 accounts for the fact that spin-containing molecules undergo Brownian motion (i.e., self diffusion with D), which is the case when fluids are the objects to be investigated. In the next section, solutions for Equation 3.5 are derived for the case of NMR relaxation in restricted environments, i.e., in porous media, and the important role of the diffusion will be emphasized. In contrast to Equation 3.3, in Equation 3.5 $\vec{H}_1(t)$ is defined as a function of time. If it is terminated, i.e., for $t > \tau_p$, the damped precession movement of \vec{M} around \vec{H}_0 (i.e., the relaxation back to the equilibrium state) takes place as described above. However, I want to remark important consequences when considering the relaxation times T_2 and T_1 during the excitation process. It should be noted that Equation 3.4 defining the flip angle θ is only valid if $\tau_p \ll T_1, T_2$, otherwise the relaxation processes during the rf-pulse appear to be non-negligible and the excitation is corrupted. In conventional laboratory NMR relaxometry this condition is always fulfilled, because rf-pulses of a few μs are applied. In some cases, however, the relaxation of \vec{M} during the excitation pulse must be accounted for, e.g., when applying surface NMR Walbrecker et al. (2009), or when applying so-called adiabatic pulses, which is necessary when dealing with earth's field NMR on the laboratory scale (Tannus and Garwood, 1997; Melton and Pollak, 2002).

Because of their different physical meaning and phenomenological behavior, both the transverse and the longitudinal relaxations can be described independently. Neglecting for the moment any diffusion processes, the focus on the z-component of Equation 3.5 by means of the rotating frame gives:

$$\frac{\delta}{\delta t} M_z(t) = -\frac{M_z(t) - M_0}{T_1}. \quad (3.6)$$

A similar equation can be found, when focussing on the x-y-plane with $M_{\perp} \equiv M_x + iM_y$:

$$\frac{\delta}{\delta t} M_{\perp}(t) = -\frac{M_{\perp}(t)}{T_2}. \quad (3.7)$$

Equations 3.6 and 3.7 are referred to as the Bloch equations (Abragam, 1983; Levitt, 2002), which have quite simple solutions:

$$\begin{aligned} M_z(t) &= M_0 \left[1 - \exp\left(-\frac{t}{T_1}\right) \right] \\ M_{\perp}(t) &= M_0 \exp\left(-\frac{t}{T_2}\right). \end{aligned} \quad (3.8)$$

Now, I want to expand the discussion of the Bloch equations for the case of an inhomogeneous \vec{H}_0 , i.e., for the case of a field gradient ΔH leading to variations of \vec{H}_0 in dependence on the spatial position \vec{r} . Following Bloch (1946), any changes in direction of \vec{H}_0 due to field gradients are not considered, because their distortion is negligible. Consequently, $\Delta H \vec{r}$ contributes only to the magnitude of \vec{H}_0 :

$$H(\vec{r}) = H_0 + \Delta H \vec{r}, \quad (3.9)$$

which leads to a spatial variation of the Larmor frequency (see Equation 3.2). Let ω_0 be the center frequency of the resulting distribution of precessing frequencies:

$$\gamma H(\vec{r}) = \gamma(H_0 + \Delta H \vec{r}) = \omega_0 + \Delta\omega_L(\vec{r}). \quad (3.10)$$

After the transformation into the rotating frame, which is realized using ω_0 as reference frequency, the transverse component of \vec{M} appears to have a rotating moment varying in dependency on its spatial position:

$$\vec{M} \times \gamma \Delta H \vec{r} = \vec{M} \times \Delta\omega_L(\vec{r}). \quad (3.11)$$

The longitudinal component of \vec{M} remains unaffected, because the inhomogeneity is considered to affect only the magnitude, i.e., the z-component of \vec{H}_0 . The impact on the transverse component leads to a modification of Equation 3.7:

$$\frac{\delta}{\delta t} M_{\perp}(t) = -\frac{M_{\perp}(t)}{T_2} + i\Delta\omega_L(\vec{r}) \quad (3.12)$$

with the solution

$$M_{\perp}(\vec{r}, t) = M_0 \exp\left(-\frac{t}{T_2}\right) \exp(-i\Delta\omega(\vec{r})). \quad (3.13)$$

The distortion of the transverse relaxation given by the term $\exp(-i\Delta\omega(\vec{r}))$, referred to as the dephasing angle, is called dephasing effect. After a single rf-pulse, the NMR response is a superposition of induced signals with varying Larmor frequencies according to Equation 3.13, and will relax apparently much faster than the undisturbed T_2 -relaxation. Such an NMR experiment is referred to as the free induction decay (FID). The FID is of particular interest in this work, because it is measured by default when using the magnetic resonance sounding method (MRS, see Chapter 3.3). However, in laboratory and borehole NMR applications, the distortion of the transverse relaxation described above is compensated by introducing an 180° -pulse that follows the initial 90° -pulse after a certain duration. This leads to a dephasing angle with opposite sign that refocuses the magnetic moments and causes the so-called spin echo (Hahn, 1950). If a pulse sequence of successive 180° -pulses is applied (the so-called CPMG-sequence, after Carr and Purcell (1954) and Meiboom and Gill (1958)), a corresponding sequence of echos (echo train) is observed, and the undisturbed T_2 relaxation is reconstructed by the envelope of these echos.

Measurements of the longitudinal relaxation also demand the application of special pulse sequences. These start either with a 90° -pulse (the so-called saturation recovery experiment), or with a 180° -pulse (the so-called inversion recovery experiment). After a certain duration, a second 90° -pulse follows that tilts the z-component of \vec{M} into the x-y plane to read it out. (As described in the last subsection, NMR response signals can only be measured in the x-y-plane.) This procedure is repeated with varying durations between

the two pulses to reconstruct the evolution of the longitudinal relaxation of \vec{M} towards its state of equilibrium.

At the end of this section, I want to emphasize again the fact that the frequency distribution of an FID signal encodes the distribution of field inhomogeneities in \vec{H}_0 as well as the transverse relaxation time T_2 . This is quite important, because the FID is the simplest and always available experiment in magnetic resonance sounding (MRS) measurements, while strategies to measure undisturbed T_1 and T_2 relaxation times cannot be realized straightforwardly and are objectives of recent research. For simplicity, the FID in MRS measurements is considered to be an exponentially decaying signal with T_2^* similar to the undisturbed transverse relaxation (Walbrecker et al., 2009). Stricly speaking, this consideration is only valid for two special cases: First, any inhomogeneities in \vec{H}_0 are negligible and the FID represents the real transverse relaxation process. Second, the gradient fields in \vec{H}_0 cause a Lorentz-distribution of Larmor frequencies (Michel, 1981). The first point is seldom realized. At least, on the microscale, always fields gradients appear, and thus, significant differences between T_2 and T_2^* are observed (Müller et al., 2005; Legchenko et al., 2002). The second point is actually quite unlikely: Rather than a Lorentz distribution, a more 'natural' distribution such as a Gaussian one might be considered. However, an objective for future research should be the investigation of alternative ways for approximating FID as measured with surface NMR methods or, at least, the investigation of the conceptual limitations coming along with the assumption of exponentially decaying FIDs.

3.2 NMR relaxation in restricted environments

3.2.1 Analytical solutions for simple pore geometry

As extension of the discussions in the previous section, diffusional aspects and the influence of pore walls are now taken into account. After the excitation, the total nuclear magnetization $M = |\vec{M}|$ inside a pore with volume V is given by the integral of all infinitesimal magnetic moments $m(\vec{r}, t)$ over V :

$$M(t) = \int_V m(\vec{r}, t) dV \quad (3.14)$$

Following Brownstein and Tarr (1979), $M(t)$ can be understood as the reduced magnetization when measuring the spin-lattice relaxation in inversion or in saturation recovery experiments:

$$E(t) = E_0[1 - 2M(t)] \quad (\text{inversion recovery}) \quad (3.15)$$

$$E(t) = E_0[1 - M(t)] \quad (\text{saturation recovery}). \quad (3.16)$$

Here, $E(t)$ is the measured NMR signal at time t with the initial amplitude E_0 . In the case of spin-spin relaxation measurements $M(t)$ is simply given by

$$E(t) = E_0 M(t). \quad (3.17)$$

The governing equation for the underlying diffusional problem as found by reformulation of Equation 3.5 by means of the rotating frame is

$$\frac{\delta m(\vec{r}, t)}{\delta t} = D \nabla^2 m(\vec{r}, t) - \frac{m(\vec{r}, t)}{T_B} \quad (3.18)$$

with the initial condition

$$m(\vec{r}, 0) = \frac{M(0)}{V} \quad (3.19)$$

and with the boundary conditions for active and passive surfaces, A and \tilde{A} , respectively:

$$\begin{aligned} [\vec{n} D \nabla m(\vec{r}, t) + \rho m(\vec{r}, t)]_A &= 0 \\ [\vec{n} D \nabla m(\vec{r}, t)]_{\tilde{A}} &= 0. \end{aligned} \quad (3.20)$$

T_B is the relaxation time of the pure pore fluid und ρ is the average sink strength of the active surface A , i.e., the surface relaxivity or surface relaxation velocity (McCall et al., 1991). A passive surface means a surface assumed to have no or negligible surface sinks, for instance the interface between water and air.

Strictly speaking, Equation 3.18 is only true for the spin-spin-relaxation when neglecting any gradients in the primary magnetic field. In geophysical NMR relaxation applications, additional relaxation effects caused by internal gradient fields must be accounted for if rocks exhibits high contents of paramagnetic minerals such as magnetite (Keating and Knight, 2007, 2008). A comprehensive description and discussion of the effects caused by field inhomogeneities at the pore scale can be found in Coates et al. (1999); Kleinberg et al. (1994); Dunn et al. (2002). Mohnke and Klitzsch (2010) investigated these effects with the help of numerical finite element modelings. However, in the most cases, these effects can be neglected, which yields the opportunity to analyze the relaxation effects analytically with the help of simple pore geometries.

The diffusional problem above (Equation 3.18) has a general solution of the form

$$m(\vec{r}, t) = \sum_n R_n(\vec{r}) A_n e^{-(1/T_B + 1/T_n)t} \quad (3.21)$$

and, consequently, the magnetization M in dependency on the observed time has generally a multi-exponential behavior:

$$M(t) = M(0) \sum_n I_n e^{-(1/T_B + 1/T_n)t} \quad (3.22)$$

Equation 3.18 can be solved by separating the variables \vec{r} and t , which leads to an eigenvalue problem for the spatial components (Brownstein and Tarr, 1979):

$$D\nabla^2 R_n(\vec{r}) = -\frac{1}{T_n} R_n(\vec{r}), \quad (3.23)$$

whereby R_n are the eigenfunctions and $1/T_n$ are the corresponding eigenvalues. The n -th eigenvalue is considered to be the reciprocal relaxation time of the n -th relaxation mode. The boundary conditions of this eigenvalue problem derived from Equations 3.20 are

$$\begin{aligned} [\vec{n}D\nabla R_n(\vec{r}) + \rho R_n(\vec{r})]_A &= 0 \\ [\vec{n}\nabla R_n(\vec{r})]_{\tilde{A}} &= 0. \end{aligned} \quad (3.24)$$

The relative intensities I_n in Equation 3.22 can now be calculated from the eigenfunctions with

$$I_n = \frac{1}{V} \frac{(\int R_n(\vec{r}) dv)^2}{\int R_n^2(\vec{r}) dv} \quad \text{with} \quad \sum_{n=0}^{\infty} I_n = 1. \quad (3.25)$$

Brownstein and Tarr (1979) presented and discussed solutions of Equation 3.23 for the cases depicted in Figure 3.1, i.e., for planar, cylindrical, and spherical geometry. The corresponding equations are summarized in Table 3.1. For these example solutions, the region of interest is placed in an environment surrounded by active surfaces only. The pore size in each case is given with a , i.e., for the case of a slit (left hand side in Figure 3.1) a represents the distance between the center of the slit and the pore walls, and for the cylindrical and spherical cases (middle and right hand side in Figure 3.1) a represents the radius of the pore. From the geological point of view, the examples in Figure 3.1 represent different cases of pores: the planar case may represent fissures in solid rocks, while cylindrical capillaries and spherical pores are often assumed for both consolidated and loose sediments, as well as for soils (Davies and Packer, 1990; Tuller et al., 1999; Godefroy et al., 2001; Tuller and Or, 2002).

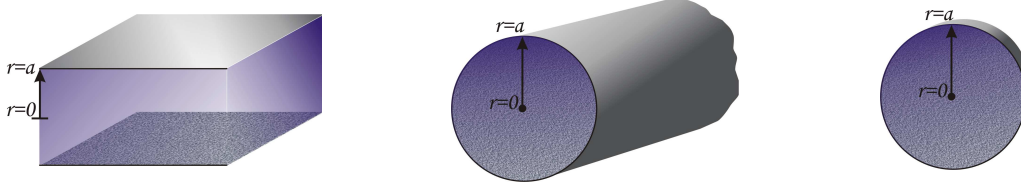


Figure 3.1: The diffusional problem for the description of NMR relaxation inside a restricted environment can analytically be solved for planar (left), cylindrical (middle), and spherical (right) geometry (Brownstein and Tarr, 1979). The parameter a represents the active surface.

Table 3.1: The analytical solutions for planar, cylindrical, and spherical geometries (Brownstein and Tarr, 1979).

	planar	cylindrical	spherical
eigenfunctions	$R_n(r) = \cos\left(\xi_n \frac{r}{a}\right)$	$R_n(r) = J_0\left(\eta_n \frac{r}{a}\right)$	$R_n(r) = \frac{\sin\left(\zeta_n \frac{r}{a}\right)}{\zeta_n \frac{r}{a}}$
eigenvalues	$T_n = \frac{a^2}{D\xi_n^2}$	$T_n = \frac{a^2}{D\eta_n^2}$	$T_n = \frac{a^2}{D\zeta_n^2}$
roots problem	$\xi_n \tan \xi_n = \frac{\rho a}{D}$	$\eta_n \frac{J_1(\eta_n)}{J_0(\eta_n)} = \frac{\rho a}{D}$	$1 - \zeta_n \cot \zeta_n = \frac{\rho a}{D}$

Brownstein and Tarr (1979) analysed the derived solutions for the saturated cases in terms of different diffusional exchange limits. They defined the sink strength parameter $\rho a/D$ to be the measure for different diffusion regimes:

- The **fast diffusion region** is characterized by $\rho a/D \ll 1$. The relaxation process is completely dominated by the lowest mode T_0 , i.e., the intensity I_0 is very close to 1.
- The **intermediate diffusion region** is characterized by $1 < \rho a/D < 10$. The relaxation process is dominated by the lowest mode, whereas higher modes with $T_n < T_0$ appear with a view percent of the total intensity. With increasing sink

strength parameter $\rho a/D$ the multi-exponential behavior of the NMR signal increases.

- The **slow diffusion region** is characterized by $\rho a/D \gg 1$. The relaxation components of the different modes have arived their asymptotic values for T_n and I_n . The lowest mode I_0 still holds the main part of the signal, and the higher modes contibute up to 40% depending on the geometry of the pore.

3.2.2 General relations between NMR and pore space properties

As shown in the previous section, the NMR signal in porous media is, in general, a multi-exponentially decaying signal (Equation 3.22). In the case of observing the longitudinal relaxation, the detected NMR signal is given by combining Equations 3.22 and 3.16:

$$E(t) = E_0 \left[1 - 2 \sum_n I_n \exp\left(-\frac{t}{T_{1,n}}\right) \right] \quad (\text{inversion recovery}) \quad (3.26)$$

$$E(t) = E_0 \left[1 - \sum_n I_n \exp\left(-\frac{t}{T_{1,n}}\right) \right] \quad (\text{saturation recovery}). \quad (3.27)$$

When observing the transverse relaxation, one detects a signal according to:

$$E(t) = E_0 \sum_n I_n \exp\left(-\frac{t}{T_{2,n}}\right). \quad (3.28)$$

The initial signal amplitude E_0 linearly depends on the amount of protons in the pore space, i.e., E_0 is proportional to the volumetric water content in a sample. The water content Θ_{NMR} can be found by calibration, e.g., with a sample of pure water yielding the reference signal amplitude $E_0(\text{calibration})$:

$$E_0 \propto \Theta_{NMR} \Rightarrow \Theta_{NMR} = \frac{E_0(\text{sample})}{E_0(\text{calibration})}. \quad (3.29)$$

In the case of a completely saturated pore space, Θ_{NMR} represents the porosity. The subscript '*NMR*' in Θ_{NMR} accounts for the fact that the amount of water measured with NMR does not necessarily match the real water content. Particularly NMR devices working in the earth's magnetic field underestimate the water content due to long measurement dead times (Legchenko et al., 2002; Boucher et al., 2011). However, conventional laboratory and borehole NMR measurements in magnetic fields at least 1000 times higher than the earth's magnetic field usually provides the water content with very high accuracy (Coates et al., 1999; Dunn et al., 2002).

The simplest NMR experiment is the FID experiment (free induction decay, see Chapter 3.1.2) with the relaxation rate

$$\frac{1}{T_2^*} = \frac{1}{T_2} + \frac{1}{T_{2,deph}} \quad (3.30)$$

An exact physical description of the distortion of the T_2 relaxation in an FID experiment is derived and discussed in Chapter 3.1.2. For simplification, this distortion is now considered to be an additional relaxation rate $1/T_{2,deph}$ (referred to as the dephasing relaxation rate) accelerating the transverse relaxation rate $1/T_2$. The T_2 relaxation rate of a water saturated sample consists of three components:

$$\frac{1}{T_2} = \frac{1}{T_{2,bulk}} + \frac{1}{T_{2,surf}} + \frac{1}{T_{2,diff}}. \quad (3.31)$$

$T_{2,bulk}$ is the bulk fluid relaxation time, which is, in the most cases, long in comparison with the other components of Equation 3.31 (e.g. water with more than 2 seconds) and is considered to be insignificant. The so-called surface relaxation rate $1/T_{2,surf}$ is the component describing the influence of the pore walls (see details in the previous section). The diffusion relaxation rate $1/T_{2,diff}$ occurs when significant \vec{B}_0 field gradients appear and the spins diffuse through this gradient field during the relaxation process. Compared to the distortion of the T_2 relaxation by $1/T_{2,deph}$, the diffusion relaxation rate cannot be compensated by any pulse sequences and must be taken into account, for instance, when the material to be investigated contains iron-bearing minerals (Keating and Knight, 2007, 2008). However, the longitudinal relaxation is not influenced by such diffusion effects:

$$\frac{1}{T_1} = \frac{1}{T_{1,bulk}} + \frac{1}{T_{1,surf}}. \quad (3.32)$$

The surface relaxation rate $1/T_{1,2,surf}$ is related to the pore space by the following equation:

$$\frac{1}{T_{1,2,surf}} = \rho_{1,2} \frac{A}{V} = \rho_{1,2} \frac{a}{r_{pore}} \quad (3.33)$$

The surface relaxation depends on the pore surface-to-volume ratio A/V and a material constant ρ_i ($i = 1, 2$), which is the surface relaxivity characterizing the influence of paramagnetic impurities at the pore surface (Dunn et al., 2002). The ratio A/V is proportional to the reciprocal pore size r_{pore} . The geometry factor a depends on the pore shape, e.g., $a=1$ for planar, $a=2$ for cylindrical, and $a=3$ for spherical pore geometry. Consequently, $T_{1,2}$ is proportional to the pore radius r_{pore} :

$$T_{1,2,surf} \propto r_{pore}. \quad (3.34)$$

This proportionality is the key of NMR interpretation in petrophysics: Having a material with a wide distribution of different pore sizes, each pore will contribute to the NMR

signal with its characteristic relaxation time. One might now introduce a new interpretation of the multi-exponential behavior formulated in Equations 3.26 to 3.28. So far, the multi-exponential approach was considered only for the possible case of a single pore being in the slow-diffusion regime and thus exhibiting different relaxation modes (see Chapter 3.2.1). The NMR signal of a sample being in the fast-diffusion regime might also relax multi-exponentially, when the signal is given by the superposition of different relaxation regimes corresponding to different pore sizes. Although the pore space geometry of geologically relevant porous material is very complicated, the average A/V ratio of the material and the corresponding mean pore radius (see Equations 3.33 and 3.34) are effective and adequate quantities regarding the estimation of the permeability (Seevers, 1966; Kenyon, 1997; Coates et al., 1999; Dunn et al., 1999). However, NMR techniques in the lab and in boreholes are also used to discover the pore size distribution (PSD). In this way, further useful information such as residual water and capillary pressure estimates can be provided by NMR (Kleinberg, 1996; Volokitin et al., 2001). Concepts of determining PSDs are based on characteristic model assumptions. In soil physics, the assumption of a capillary bundle is adequate (Kutilek and Nielson, 1994; Warrik, 2003). When dealing with consolidated material such as sandstones, the pore space is usually considered to consist of spherical pores connected to each other by pore throats. One may imagine the throats to be of cylindrical shape or just openings from one pore to another. Because NMR is mainly sensitive to the pore bodies, the throats cannot be directly accounted for, when interpreting NMR data in terms of PSD estimations. There exists, however, a statistical relationship between the distribution of pore bodies and throats which allows for comparing NMR relaxation time distributions and PSDs, at least in sandstones and carbonates (Coates et al., 1999; Dunn et al., 2002). In the literature, many examples can be found that show an agreement of the PSDs estimated from NMR with those measured with the mercury injection method (Kenyon et al., 1989; Howard and Kenyon, 1992).

The principle of PSD estimation from NMR is depicted in Figure 3.2. Due to the linearity between $T_{1,2}$ and the pore size (Equation 3.34), the distribution of the relaxation times can simply be shifted on the logarithmic scale to find the pore size distribution. Thereby, the shifting value includes the surface relaxivity ρ and the pore geometry value a (see Equation 3.33). These parameters are usually not available, however, the shifting factor can be found by calibration. When interpreting NMR well loggings, the calibration is done by mercury injection measurements at cores. Jaeger et al. (2009) tried to find a similar calibration method for estimating WRCs (water retention curves) from T_2 relaxation measurements for soil samples. They found that a representation of the WRC from the NMR relaxation time distribution is only possible, if two different ρ 's are considered, one for macro- and the other one for micropores. Concluding their results, they described their approach to suffer from a very time-consuming procedure unfavorable for practical use, because the effort for a reliable calibration of the NMR data is equivalent to those of simple WRC measurements.

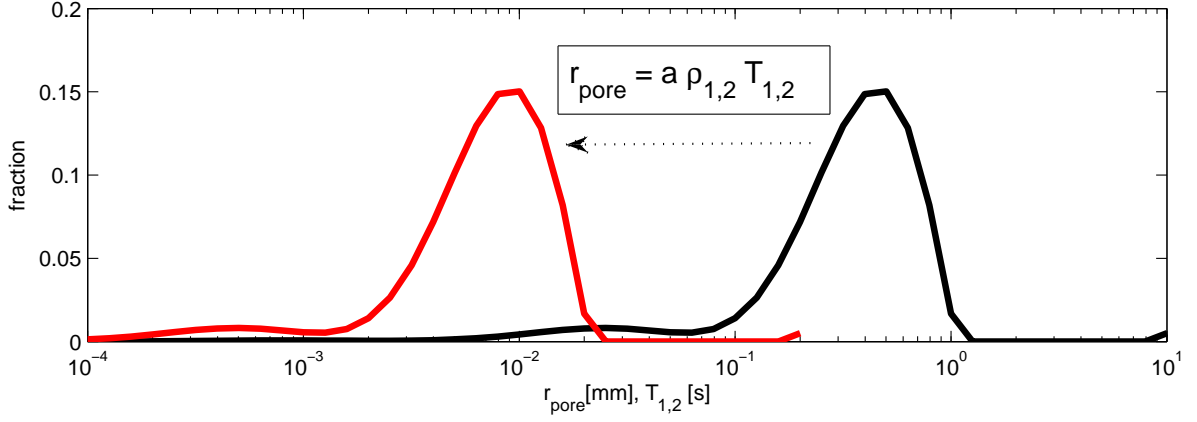


Figure 3.2: The pore size distribution (PSD) is reconstructed from the NMR relaxation time distribution simply by shifting the NMR distribution on the logarithmic scale by the product of the pore-geometry parameter a and the surface relaxivity $\rho_{1,2}$.

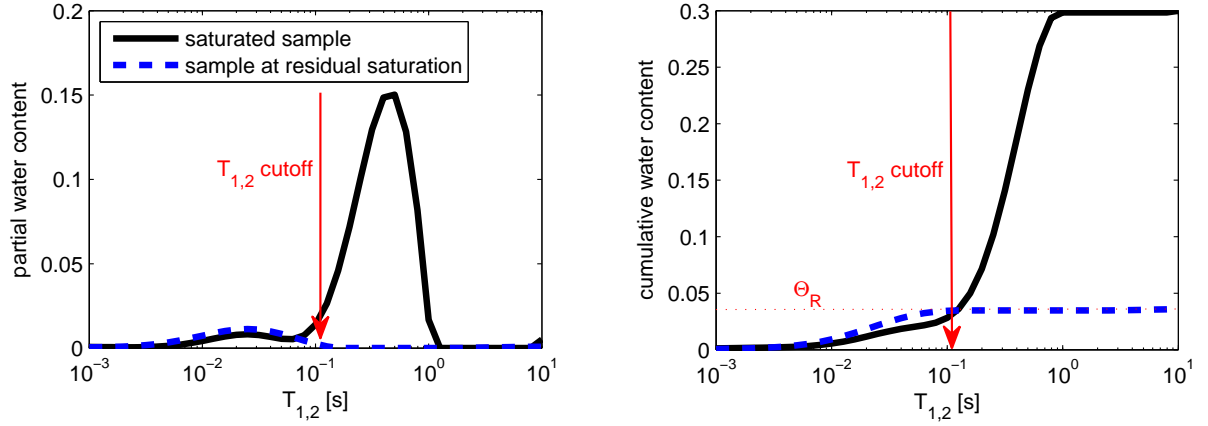


Figure 3.3: The cutoff value, which is the threshold in the NMR relaxation time distribution determining the residual water content Θ_R , is found by calibration: After desaturation (e.g., by centrifuging), the part of the distribution that represents Θ_R is identified (left hand side). When plotting the cumulative distributions of both the saturated and the unsaturated states, the threshold is given by the intersection of both curves (right hand side).

Beside the PSD, the amount of capillary-bound water, i.e., the residual water content Θ_R , is of high interest in oil exproation, as well as in soil physics. In well-logging practice, this parameter is found by the so-called cutoff (CO) method. A threshold $T_{2,CO}$ is defined that splits the T_2 distribution: The water content represented by T_2 times longer than $T_{2,CO}$ (bigger pores) is considered to be free, i.e., to consist of moveable water, whereas the part of the distribution shorter than $T_{2,CO}$ is considered to be Θ_R . Although depending strongly on the lithology (texture, fluid chemistry, ferro- and paramagnetic

components, etc.), the threshold is often considered to be a constant value with 33 ms for sandstones (Schlumberger, 1997; Coates et al., 1999) and with 30 ms for loose sediments (Schirov et al., 1991; Legchenko et al., 2002). However, for a plausible estimation of Θ_R , a calibration accounting for the specific nature of the material to be investigated is surely necessary, no matter if estimated from borehole NMR data for oil exploration or from laboratory NMR data for soil assessment. For consolidated sediments this is often done with centrifuge techniques. The moveable water content is removed and the remaining NMR distribution is measured, from which the actual cutoff value is determined (Coates et al., 1999). The procedure is depicted in Figure 3.3. When working with unconsolidated material, centrifuge techniques are not a good choice due to the compaction of the sediment, therefore soil physical methods as described in Chapter 2 should be applied. A main objective of this work is the adaptation of the principles described above for calibrating NMR measurements to estimate the WRC and Θ_R for the use in soil physics.

3.2.3 Multi-exponential relaxation - NMR data approximation

To interpret NMR signals by means of pore size distributions, it is necessary to reconstruct the multi-exponential behavior. This is usually done using an inverse Laplace transform algorithm to invert Equations 3.26 to 3.28. I show the underlying principle here only for the transverse relaxation. However, the adaptation of the inversion algorithms for the longitudinal relaxation is analog to the following description. One might change the notation of Equation 3.28 to account for the discrete time sampling, i.e., the detected signal E_i at time t_i is given by:

$$E_i = E_0 \sum_n I_n \exp\left(-\frac{t_i}{T_n}\right) + N_i, \quad (3.35)$$

whereby N_i is the noise that superposes the NMR response signal. For inverting this equation to get the distribution I_n as a function of T_n , one has to solve the following minimizing problem by means of least squares:

$$F_{min}(I) = \sum_{i=1}^m \left[\sum_{j=1}^n I_j \exp\left(\frac{-t_i}{T_j}\right) - E_i \right]^2. \quad (3.36)$$

Due to the ill-posed character of this problem, one has to regularize the inversion. This can be realized by including smoothness constraints to account for the fact that geologically relevant porous material naturally exhibits statistically distributed pores of different sizes. Various strategies for including smoothness constraints can be applied (Dunn et al., 2002). I use the so-called norm smoothing:

$$F_{min}(I) = \sum_{i=1}^m \left[\sum_{j=1}^n I_j \exp\left(\frac{-t_i}{T_j}\right) - E_i \right]^2 + \lambda_{smooth} \sum_{j=1}^n I_j^2. \quad (3.37)$$

The parameter λ_{smooth} controls the weighting of the smoothness constraints. It has to be chosen considering the actual noise level of the data. When λ_{smooth} is too small, the problem is under-regularized and the noise will be misinterpreted as a part of the model. With increasing λ_{smooth} , the smoothness of the model increases such that the data approximation suffers and the result gets more and more unplausible. The usual trade-off is the convention-like assumption that the optimal distribution of relaxation times should show the highest degree of smoothness within the plausibility range given by the noise level of the measurement.

I want to show this principle with two examples. Figure 3.4a shows a transverse relaxation measurement of a saturated sand sample, and Figure 3.4b the corresponding optimal T_2 distribution compared with a mono-exponential representation of the very same data. In Figure 3.4c, the relative root mean square error (RMS) of further smooth inversion results is plotted against the smoothness parameter λ_{smooth} . The asymptotic value for decreasing λ_{smooth} represents the relative noise level of the data. When λ_{smooth} increases, the RMS curve always exhibits an immediate increase at a certain λ_{smooth} . This is the point, where the data approximation becomes unplausible. Often, the λ_{smooth} value corresponding to the highest curvature in the neighborhood of this point is chosen to identify the optimal multi-exponential approximation to the data automatically. However, in this work the optimal λ_{smooth} is chosen by determining manually the largest λ_{smooth} representing the asymptotic value (black circle in Figure 3.4). Beside the multi-exponential approximation of the data example in Figure 3.4, a mono-exponential fit was applied to test the necessity of using a multi-exponential model. The red dotted line in Figure 3.4 represents the corresponding RMS value. Obviously, the quality of the mono-exponential fit is quite similar to the optimal multi-exponential one, i.e., in the case of the sand sample at hand a mono-exponential approximation would explain the NMR data accurate enough within the noise level.

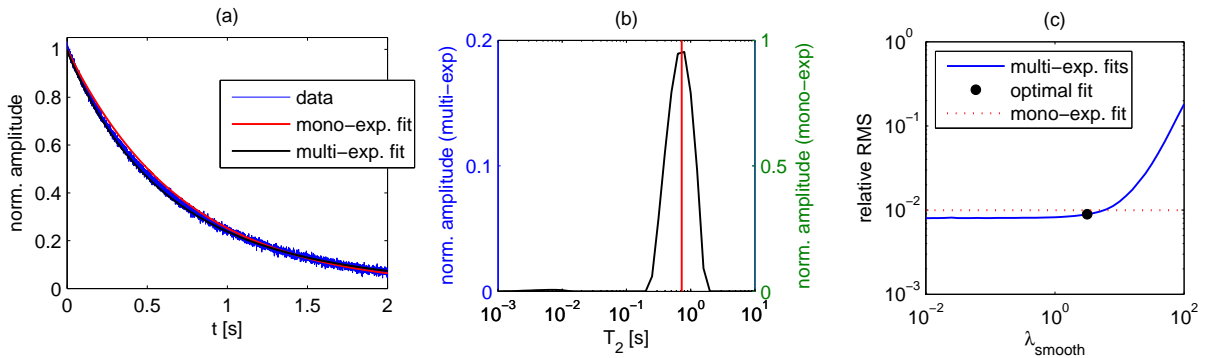


Figure 3.4: Measurement of the transverse NMR relaxation of a saturated pure sand sample: (a) approximation of the data by both multi- and mono-exponential fits, (b) T_2 distribution compared to the mono-exponential representation, (c) root mean square values (RMS) from various data approximations vs. corresponding smoothness parameter λ_{smooth} .

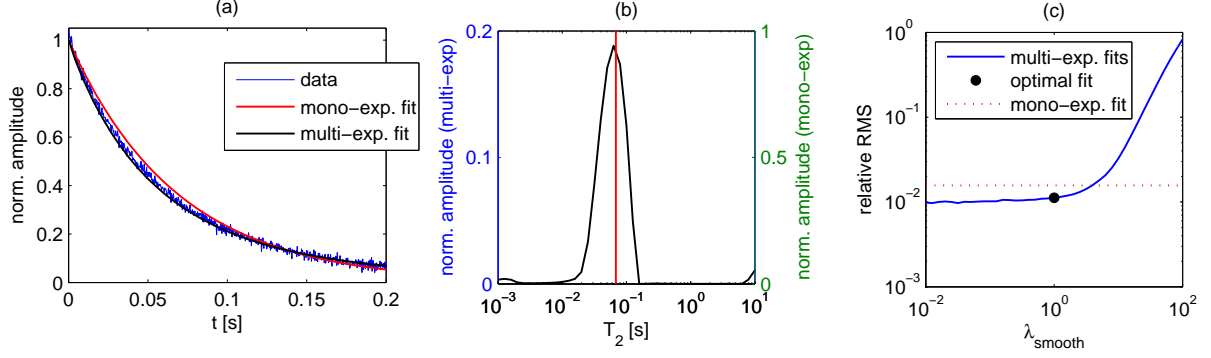


Figure 3.5: Measurement of the transverse NMR relaxation of a saturated sandy silt sample: (a) approximation of the data by both multi- and mono-exponential fits, (b) T_2 distribution compared to the mono-exponential representation, (c) root mean square (RMS) values from various data approximations vs. corresponding smoothness parameter λ_{smooth} .

However, this is not the general case, as depicted in Figure 3.5. Here, the data approximation of an NMR measurement with a sandy silt sample was investigated. The resulting RMS value of the optimal multi-exponential approximation is significantly smaller than the RMS resulting from the mono-exponential fit.

3.3 NMR on field scale - magnetic resonance sounding (MRS)

In MRS, the earth's magnetic field is used as \vec{H}_0 field, and \vec{H}_1 is generated using a circular or square loop as transmitter on the surface. In standard MRS applications for 1D-investigations, the same loop is used as receiver (Legchenko et al., 2002). Similar to laboratory NMR applications, the loop is energized for a certain duration τ_p with a pulse of an alternating current I that generates the exciting field \vec{H}_1 in the subsurface:

$$I(t) = I_0 \cos(2\pi f_L \tau_p) \quad (3.38)$$

The intensity of excitation is given by the pulse moment $q = I_0 \tau_p$. Reminding the definition of the flip angle (Equation 3.4), it is obvious that q controls the flip angle θ of the nuclear magnetization \vec{M} caused by the proton spin in the subsurface. The main difference of the MRS principle compared to NMR applications in the laboratory is the fact that the NMR response is generated in the outside of the loop, i.e., the magnitude of \vec{H}_1 varies depending on the spatial position under the loop. Thus, many different flip angles are generated within the excited volume depending on their spatial position inside the \vec{H}_1 field. After the excitation, the NMR response signal, which induces a voltage in the receiver loop, is given by the components of \vec{M} perpendicular to the earth's magnetic

field. Thereby, the main part of the signal is given by subsurface water in regions with $\theta \approx \pi/2$ with respect to \vec{H}_0 . During an MRS sounding, an increase of q leads to a shift of these regions to larger depths and thus to an NMR response from deeper regions. The induced voltage of the signal is a function of the observation time t and q , respectively:

$$E(t, q) = E_0(q) \sum_n w_n(q) \exp \left[-\frac{t}{T_{2,n}^*(q)} \right] \cos [2\pi f_L t + \phi(q)] \quad (3.39)$$

$T_{2,n}^*$ is the relaxation time of the n -th relaxation regime. Its fraction on the signal is given with w_n , ϕ_0 is the phase shift of the signal with respect to the energizing pulse, and E_0 is the initial amplitude of the signal, which is directly proportional to the amount of excited protons, i.e., proportional to the pore water content. Assuming a 1D-distribution of the subsurface water content $\Theta(z)$ and neglecting for the moment any NMR relaxation aspects, the initial amplitude E_0 after the excitation is a function of q (Legchenko and Shushakov, 1998):

$$E_0(q) = \int_z \kappa_{1D}(q, z) \Theta_{NMR}(z) dz \quad (3.40)$$

The kernel function $\kappa_{1D}(q, z)$ describes the contribution of the subsurface regions to the signal (Hertrich, 2005). It depends on the electrical resistivity distribution of the subsurface and the chosen measurement configuration, i.e., the loop geometry and the applied sequence of pulse moments q (Legchenko and Valla, 2002; Weichman et al., 2002). Because $\kappa_{1D}(q, z)$ defines the sensitivities of the MRS measurements, it represents the basis of the inversion to obtain the NMR water content as a function of depth $\Theta_{NMR}(z)$. The inverse problem can be solved in different ways, which are discussed in the literature (Legchenko and Shushakov, 1998; Mohnke and Yaramanci, 2002; Weichman et al., 2002).

The characterization of the subsurface by T_2^* necessitates an enhanced formulation of the MRS forward problem, which includes the occurrence of multi-exponential NMR relaxation with time (Mohnke and Yaramanci, 2005):

$$E(t, q) = \int_z \int_{T_2^*} \kappa_{1D}(q, z) \Theta_{NMR}(z, T_2^*) \exp \left[-\frac{t}{T_2^*(z)} \right] dT_2^* dz \quad (3.41)$$

Θ_{NMR} appears now as a function of both z and T_2^* , i.e., it represents the distribution of the water within different relaxation regimes. Different relaxation regimes inside the investigated volume may exist on the pore scale (e.g. due to the pore size distribution), as well as on the macroscopic scale as a function of z (e.g. layers with different lithology). Inversion strategies for Equation 3.41 are proposed by Mohnke and Yaramanci (2005) (time-step inversion) and Müller-Petke (2009) (QT inversion).

Chapter 4

NMR relaxation in partially saturated pores

This chapter aims on the developement of physically plausible model assumptions about the NMR relaxation behavior of water in partially saturated pore spaces. Principle considerations and analytical calculations are introduced that start at simple single pores with the focus on the special role of pore geometry and move towards the analysis of a pore ensemble represented by an empirical pore-size-distribution index as usual in soil physics. These theoretical findings are the fundamental basis for the interpretation of the experiments reported and discussed in the following chapters.

4.1 Theoretical considerations for simple pore geometries

4.1.1 NMR saturation degree

When characterizing the water-filling state of a soil sample, it is adequate to use the saturation degree S . The proportionality between NMR amplitude and water content allows the definition the NMR saturation degree S_{NMR} as follows:

$$E_0 \propto \Theta_{NMR} \Rightarrow S_{NMR} = \frac{E_{0,S<1}}{E_{0,S=1}}, \quad (4.1)$$

where $E_{0,S<1}$ is the NMR signal amplitude at partial saturation and $E_{0,S=1}$ the amplitude at saturation. Following the common soil physical concept using the effective saturation (Equation 2.3), I define the effective NMR saturation as follows:

$$S_{E,NMR} = \frac{\Theta_{NMR} - \Theta_{R,NMR}}{\Theta_{S,NMR} - \Theta_{R,NMR}} = \frac{S_{NMR} - S_{R,NMR}}{1 - S_{R,NMR}}. \quad (4.2)$$

4.1.2 Analytical solutions for planar, cylindrical, and spherical cases

Coming from the analytical solutions showed in Chapter 3.2.1, I want to derive here solutions for pore systems under the assumption of partial saturation, that is, additional passive boundaries in the interior of the pores. For the case of a pore filled with both a vapor and a liquid phase, the interphase between both has negligible surface sinks. This interface must be taken into account with zero surface relaxivity $\rho = 0$. In Figure 4.1, this situation is shown for pores with planar, cylindrical, and spherical geometries. Let us assume the liquid phase to behave as wetting phase to the pore walls, which is normally the case for water inside silicious rocks and soils. After the entering of a gas bubble into the pore, the liquid in the interior of the pore is displaced, whereas liquid films remain on the pore surface. The thickness of the liquid layer is given by $a - \tilde{a}$, where a represents the active and \tilde{a} the passive surface, respectively. The following solutions are given as functions of S , whereby S is defined individually as a function of a and \tilde{a} for each case depicted in Figure 4.1. The underlying eigenvalue problem describing the NMR relaxation response was already introduced and discussed for saturated pores in Chapter 3.2.1 (Equations 3.22 to 3.25).

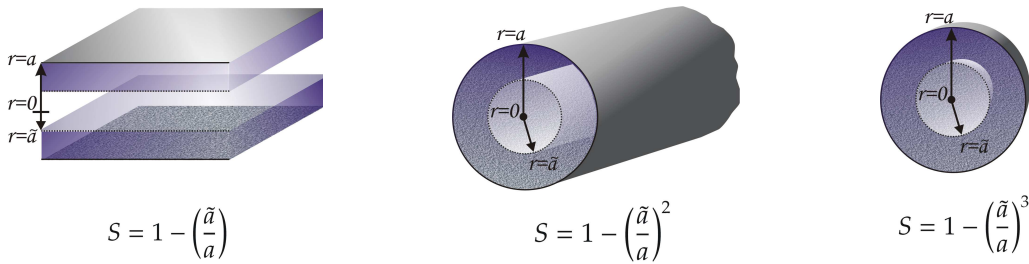


Figure 4.1: Simple pore geometries with analytical solutions for the NMR relaxation under partially saturated conditions (water film on the pore surface). Compared with the pore models in Figure 3.1, an additional passive surface at \tilde{a} is introduced representing the vapor-liquid interface. Consequently, the saturation degree S given as the ratio of the liquid phase volume and the total pore volume is a function of a and \tilde{a} , respectively.

Planar geometry

In the planar case, the thickness of the liquid film on the surface is given by $a - \tilde{a} = Sa$. The solution of the eigenvalue problem in Equation 3.23 in Cartesian coordinates is (see also Table 3.1):

$$R_n(r) = \cos\left(\xi_n \frac{r}{a}\right). \quad (4.3)$$

Compared to the saturated case shown in Table 3.1, the resulting relaxation times are modified with respect to S :

$$T_n = \frac{a^2 S^2}{D \xi_n^2}, \quad (4.4)$$

where ξ_n are given by the positive roots of the following equation:

$$\frac{\rho a}{D} = \frac{\xi \tan \xi_n}{S}, \quad (4.5)$$

which results from the substitution of $R_n(r)$ in the boundary conditions for a and \tilde{a} (Equations 3.24).

Cylindrical geometry

The eigenvalue problem in Equation 3.23 expressed in terms of cylindrical coordinates has the form of a Bessel's differential equation with the solution

$$R_n(r) = \alpha_n J_0\left(\eta_n \frac{r}{a}\right) + \beta_n Y_0\left(\eta_n \frac{r}{a}\right). \quad (4.6)$$

J_0 and Y_0 are the Bessel functions of the first and second kind, respectively. The solution for the cylindrical pore in the saturated state as given in Table 3.1 is simplified with $\beta_n = 0$, because the limit of Y_0 for $r \rightarrow 0$ would be $-\infty$, which is actually not possible from the physical point of view. For the unsaturated case the minimum value of r is given with $\tilde{a} > 0$ and, consequently, one has to take into account that $\beta_n \neq 0$. The ratio α_n/β_n is given by the passive boundary condition at \tilde{a} with

$$\frac{\alpha_n}{\beta_n} = -\frac{Y_1(\tilde{\eta}_n)}{J_1(\tilde{\eta}_n)}, \quad (4.7)$$

whereby

$$\tilde{\eta}_n = \eta_n \sqrt{1 - S} = \eta_n \frac{\tilde{a}}{a}. \quad (4.8)$$

The absolute determination of α_n and β_n is not possible. However, regarding the relative intensities of the relaxation modes in Equation 3.25, the constants α_n and β_n do not

necessarily have to be determined exactly as long as the ratio of both is known. With the corresponding eigenfunctions

$$R_n(r) = J_0\left(\eta_n \frac{r}{a}\right) - \frac{J_1(\eta_n \sqrt{1-S})}{Y_1(\eta_n \sqrt{1-S})} Y_0\left(\eta_n \frac{r}{a}\right) \quad (4.9)$$

the intensities in Equation 3.25 can be calculated. The corresponding relaxation times for the unsaturated cylinder are

$$T_n = \frac{a^2}{D\eta_n^2}, \quad (4.10)$$

and can be calculated from the positive roots η_n of

$$\frac{\rho a}{D} = \eta_n \frac{Y_1(\tilde{\eta}_n)J_1(\eta_n) - J_1(\tilde{\eta}_n)Y_1(\eta_n)}{Y_1(\tilde{\eta}_n)J_0(\eta_n) - J_1(\tilde{\eta}_n)Y_0(\eta_n)}. \quad (4.11)$$

Spherical geometry

When expressing the eigenvalue problem in Equation 3.23 in terms of spherical coordinates, the solution is given by

$$R_n(r) = \alpha_n \frac{\sin(\zeta_n \frac{r}{a})}{\zeta_n \frac{r}{a}} + \beta_n \frac{\cos(\zeta_n \frac{r}{a})}{\zeta_n \frac{r}{a}}. \quad (4.12)$$

Similar to the cylindrical case, the solution for a sphere completely saturated with water postulates $\beta_n = 0$ regarding the physical plausibility, i.e., regarding the limits for $r \rightarrow 0$. For the unsaturated sphere, we note here again that $r \geq \tilde{a} > 0$ and, consequently, $\beta_n \neq 0$. The ratio α_n/β_n can be found with

$$\frac{\alpha_n}{\beta_n} = \frac{1 + \tilde{\zeta}_n \tan(\tilde{\zeta}_n)}{\tilde{\zeta}_n - \tan(\tilde{\zeta}_n)} \quad (4.13)$$

with

$$\tilde{\zeta}_n = \zeta_n(1-S)^{1/3}. \quad (4.14)$$

The eigenfunctions are given with

$$R_n(r) = \frac{\sin(\zeta_n \frac{r}{a})}{\zeta_n \frac{r}{a}} + \frac{\tilde{\zeta}_n - \tan(\tilde{\zeta}_n)}{1 + \tilde{\zeta}_n \tan(\tilde{\zeta}_n)} \cdot \frac{\cos(\zeta_n \frac{r}{a})}{\zeta_n \frac{r}{a}}. \quad (4.15)$$

The relaxation times expressed by

$$T_n = \frac{a^2}{D\zeta_n^2} \quad (4.16)$$

are determined by the positive roots of

$$\frac{\rho a}{D} = \frac{\tilde{\zeta}_n - \zeta_n + (1 + \zeta_n^2(1-S)^{1/3}) \tan(\zeta_n - \tilde{\zeta}_n)}{\tan(\zeta_n - \tilde{\zeta}_n) + \tilde{\zeta}_n}. \quad (4.17)$$

Diffusion regimes in dependence on the saturation degree

In Chapter 3.2.1, the relaxation behavior of saturated pores in terms of different diffusional exchange limits is described according to Brownstein and Tarr (1979). With the solutions for the unsaturated cases as derived above, I want to extend this analysis with respect to the saturation degree S . On the left column of Figure 4.2, the relative intensity of the lowest relaxation mode is plotted as a function of the sink strength parameter $\rho a/D$ and of S for planar, cylindrical, and spherical geometries. With decreasing S , the limits for the different diffusional regions are continuously shifted towards higher sink strength parameters. Consequently, a pore being in the slow or in the intermediate diffusion regime at saturation will tend to get into the fast diffusion regime when desaturated, i.e., the relaxation behavior is more and more dominated by the lowest relaxation mode. The right column of Figure 4.2 shows the relaxation time of the lowest mode T_0 as a function of S normalized with $T_0(S = 1)$ to values between 0 and 1. Obviously, in the fast diffusion regime, $T_0(S < 1)$ linearly depends on S . This linearity can simply be shown analytically. Assuming the pore surface to remain wetted during the entering of the vapor phase into the pore space, Equation 3.33 is modified by multiplying the pore volume V with S (Mattea et al., 2004):

$$\frac{1}{T_0(S < 1)} = \rho_{1,2} \frac{A}{VS}. \quad (4.18)$$

Mattea et al. (2004) have experimentally shown this linear relationship between the spin-lattice relaxation time and S for water filled nano- and microporous silica glasses. In the slow and intermediate diffusion regime the ratio $T_0(S < 1)/T_0(S = 1)$ differs from linearity.

4.1.3 NMR response of partially saturated angular pores

For the derivations above, the governing basis was the assumption that the pore surface remains wetted all the time during the desaturation and that the water films are permanently in diffusive contact. This assumption is expected to be valid in material with large pore-to-surface ratios such as clay and silt. In contrast, regarding the water content in sandy material the adsorbed water films play a minor role due to their small volume compared to the capillary water bounded in the corners between the grains. An adequate pore model to describe such systems is the angular pore model as suggested by Ransohoff and Radke (1988) and by Tuller et al. (1999). This model is based on capillaries with angular cross-sections.

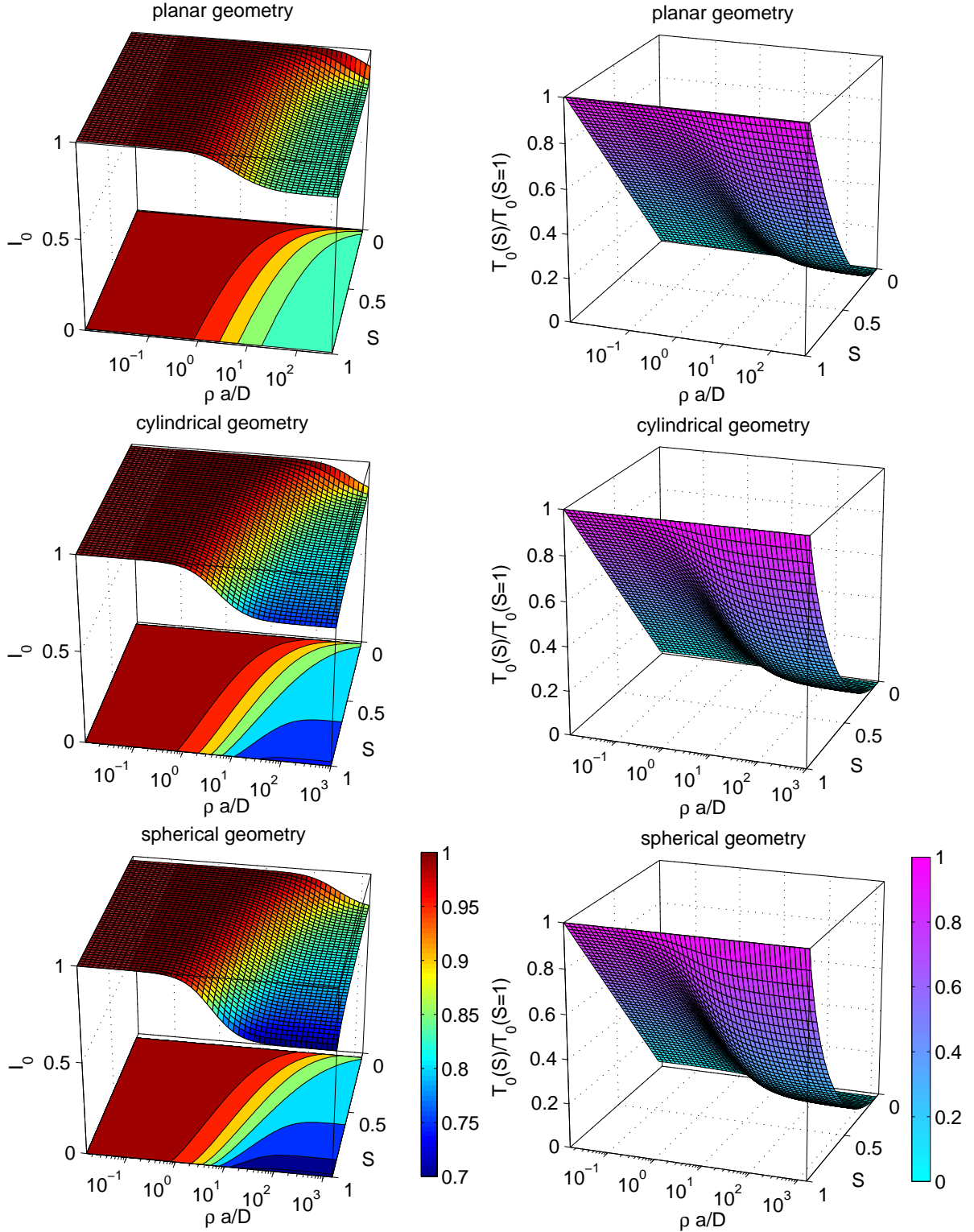


Figure 4.2: On the left hand side, the relative intensity of the lowest mode I_0 as a function of both the sink strength parameter $\frac{\rho a}{D}$ and the saturation degree S is depicted. On the right hand side, the relaxation time of the lowest mode T_0 (normalized by T_0 at saturation $S = 1$) is shown as a function of $\frac{\rho a}{D}$ and S .

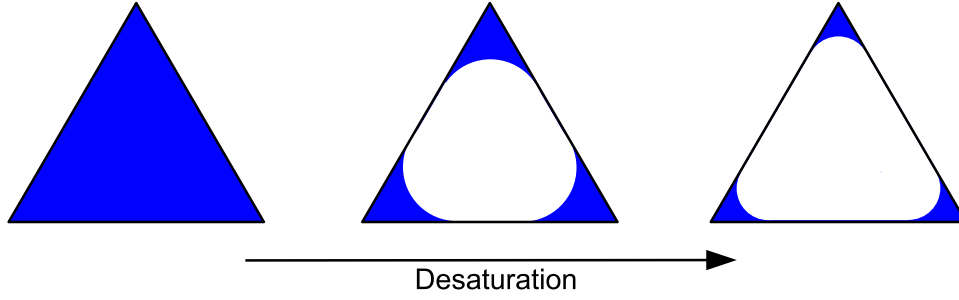


Figure 4.3: Desaturation of an angular pore model. The model is based on the assumption of a capillary with angular cross-section, e.g., with an equilateral triangle.

In Figure 4.3, the cross-section of an equilateral triangle is depicted as an example to show how such pore systems are expected to desaturate. During desaturation, water remains in the corners due to capillary forces. As long as the entering of the vapor phase is proceeding, the water is more and more displaced by gas bubbles. The radius of the meniscus curvature r_{mc} corresponds to the capillary pressure (Tuller et al., 1999) and consequently S must be defined as a function of r_{mc} . The NMR response of such a pore system during desaturation will now be derived under the assumption that, first, water films on the pore walls are negligible and, second, the system is in the fast diffusion regime (see Chapter 3.2.1 and 4.1.2). In contrast to the linear relationship between $T_0(S < 1)$ and S as discussed in the previous section (Equation 4.18), one must account for the fact that in an angular pore model the wetted pore surface A depends on S . Thus, the relaxation rate for an angular pore is of the form:

$$\frac{1}{T(S < 1)} = \rho \frac{A(S)}{VS} = \rho \frac{A(r_{mc})}{V(r_{mc})}. \quad (4.19)$$

For the sake of clarity, I omit now the index '0' compared to the notation in Equation 4.18 for the zeroth relaxation mode, which is the only relevant mode when assuming the fast diffusion regime (see Chapter 3.2.1).

In general, the cross-sectional area of the capillary is considered to be an irregular polygon with n corners. The total water content is given by the sum of the water in each corner, and is a function of the radius of the meniscus curvature r_{mc} , which is equal in each corner. The water filled area of the i -th corner after the entering of the vapor phase is given by (Tuller et al., 1999)

$$V_i(r_{mc}) = r_{mc}^2 \left[\frac{1}{\tan\left(\frac{\gamma_i}{2}\right)} - \frac{\pi - \gamma_i}{2} \right], \quad (4.20)$$

where γ_i is the angle of the i -th corner in radian.

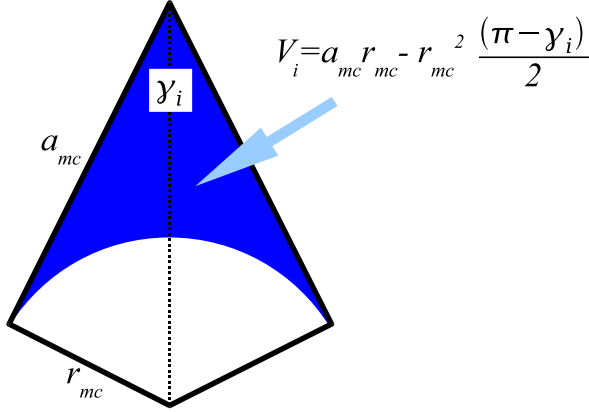


Figure 4.4: Geometrical inspection of the water volume in a single corner of an angular pore.

The wetted pore surface of the i -th corner can be found with (Figure 4.4):

$$A_i(r_{mc}) = 2a_{mc} = \frac{2r_{mc}}{\tan\left(\frac{\gamma_i}{2}\right)} \quad (4.21)$$

Now, the NMR relaxation response of a corner with angle γ_i can be defined as a function of r_{mc} :

$$\frac{1}{T_{i,U}(r_{mc})} = \rho \frac{A_i(r_{mc})}{V_i(r_{mc})} = \frac{\rho}{r_{mc} \left(\frac{1}{2} - \left[\frac{\pi - \gamma_i}{4} \tan\left(\frac{\gamma_i}{2}\right) \right] \right)} \quad (4.22)$$

Assuming the pore space to consist of a wide spectrum of different γ_i , the NMR response signal of such a pore system would become multi-exponentially after desaturation, even if the coupling of the entire pore space at saturation causes a mono-exponential signal. The entering gas bubbles would isolate the capillary bound water in each corner and consequently each corner would behave like an individual relaxation regime.

$$E(t) = E_0 \sum_n I_n \exp\left(-\frac{t}{T_{i,U}}\right) \quad (4.23)$$

However, to best of the author's knowledge, such a behavior of a porous medium during desaturation was never reported in the literature. Thus, it seems to be legitimate to assume γ_i to be very similar for all corners of the pore space, i.e., to assume the cross-sections of the capillaries to be regular polygons. The NMR signal of such a pore system is mono-exponentially at saturation and remains mono-exponentially during desaturation. Any multi-exponential character at saturation, as well as at partial saturation would be caused by the natural pore size distribution (see Chapter 3.2.2).

Let us consider an angular capillary pore with regular polygonal cross-section, with n corners, and with the side length L . The relaxation rate at saturation $1/T_S$ is given by the ratio of the surface nL and the volume $nL \cot(\pi/n)/4$ multiplied with the surface relaxivity ρ :

$$\frac{1}{T_S} = \rho \frac{n}{L \Lambda_n}. \quad (4.24)$$

Λ_n is referring to as the area factor following Tuller et al. (1999):

$$\Lambda_n = \frac{n}{4} \cot\left(\frac{\pi}{n}\right). \quad (4.25)$$

The geometry factor a (see Equation 3.33) of the regular angular pore is given with $a = 1/4 \cot\left(\frac{\pi}{n}\right)$. After the entry of the vapor phase the total water volume is found with

$$V(r_{mc}) = \sum_{i=1}^n V_i(r_{mc}) = r_{mc}^2 \Psi_n \quad (4.26)$$

with the so-called angularity factor Ψ_n (Tuller et al., 1999):

$$\Psi_n = \sum_{i=1}^n \left[\frac{1}{\tan\left(\frac{\gamma_i}{2}\right)} - \frac{\pi - \gamma_i}{2} \right]. \quad (4.27)$$

Analog to the total water volume in Equation 4.26, the total wetted surface $A(r_{mc})$ after the desaturation is given by the sum

$$A(r_{mc}) = \sum_{i=1}^n A_i(r_{mc}) = 2r_{mc}\Gamma_n \quad (4.28)$$

with

$$\Gamma_n = \sum_{i=1}^n \cot\left(\frac{\gamma_i}{2}\right) \quad (4.29)$$

When defining S with respect to the given geometrical properties, we note that, at partial saturation, S is limited to a certain maximum value due to the fact that

$$r_{mc} < \frac{L}{2} \tan\left(\frac{\gamma_i}{2}\right), \quad (4.30)$$

and consequently

$$S < \frac{\Psi_n}{4\Lambda_n} \tan^2\left(\frac{\gamma_i}{2}\right). \quad (4.31)$$

Tuller et al. (1999) defined additional thresholds for S with respect to the dependency of γ_i on the capillary pressure head. However, these are irrelevant for the considerations in this work and thus, the highest possible value of S is defined here solely for geometrical reasons. Keeping the upper limit of S in mind, one may define the saturation degree for the angular pore with:

$$S = \frac{r_{mc}^2 \Psi_n}{L^2 \Lambda_n}. \quad (4.32)$$

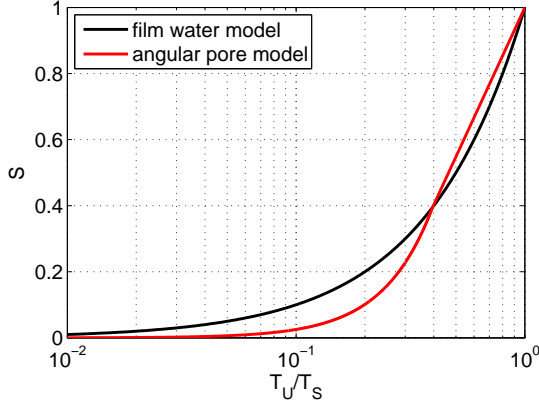


Figure 4.5: The relative relaxation time as a function of S for the angular model (capillary with equilateral-triangle-shaped cross-section) compared with the linear relation of the film water model.

The relaxation rate of the angular pore at partial saturation $1/T_U$ defined as a function of r_{mc} yields

$$\frac{1}{T_U} = \rho \frac{2\Gamma_n}{r_{mc}\Psi_n}. \quad (4.33)$$

Combining Equations 4.24, 4.32, and 4.33, one will find the general ratio T_U/T_S of an arbitrary angular pore with:

$$\frac{T_U}{T_S} = S^{1/2} \frac{n}{2\Gamma_n} \sqrt{\frac{\Psi_n}{\Lambda_n}}. \quad (4.34)$$

In Figure 4.5, this ratio for the case of a capillary with a cross-sectional area being an equilateral triangle is plotted against S and compared with the linear relationship of T_U/T_S and S for the water film models (Equation 4.18). Please note that the x-axis is plotted with logarithmic scale according to the usual way of presenting relaxation times and their relationships to other quantities. For the equilateral triangle, Equation 4.34 simplifies to:

$$\frac{T_U}{T_S} = S^{1/2} \tan\left(\frac{\pi}{6}\right) \sqrt{3 - \frac{\pi}{\sqrt{3}}} \quad (4.35)$$

with

$$S < \left(3 - \frac{\pi}{\sqrt{3}}\right) \tan^2\left(\frac{\pi}{6}\right). \quad (4.36)$$

4.2 Data examples with mono-exponential NMR response

In the previous section, theoretical considerations were made about the NMR relaxation response of partially water-filled pores. It was shown that, on the one hand, linearity exists between the NMR relaxation time and the saturation degree S , if the water content consists of water films on the pore walls. On the other hand, a square root relationship

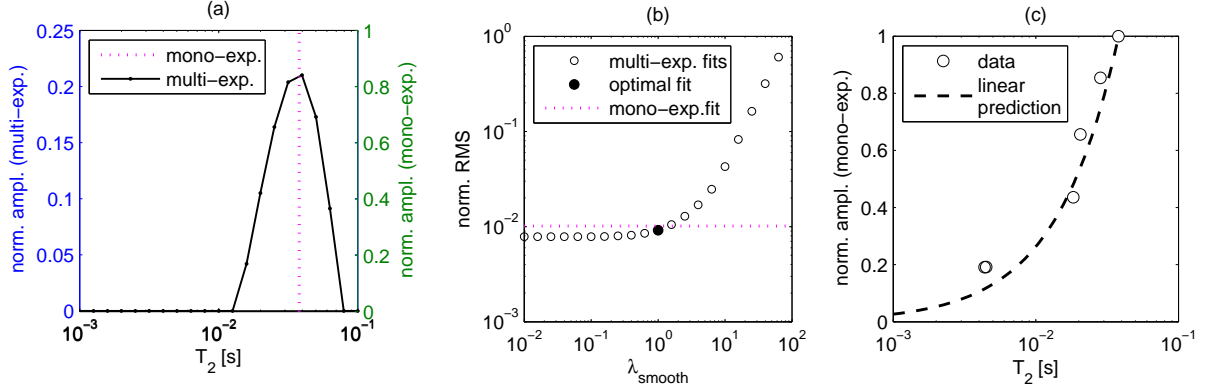


Figure 4.6: (a) NMR T_2 distribution of the saturated sand-clay mixture (30% clay content) compared with the spectral line representing the mono-exponential approximation. (b) Determination of the optimal smoothness parameter λ_{smooth} (according to the procedure described in Chapter 3.2.3) and comparison with the relative root mean square value resulting from the mono-exponential fitting. (c) Saturation dependency of the T_2 times compared with the linear prediction (after Equation 4.18).

between both quantities exists, if the influence of water films are negligible and the water content at partial saturation consists only of capillary bound water in the corners between the grains. It is expected that a combination of both features have to be considered when investigating natural soil samples. However, in this section two examples are shown that almost satisfy the extremal conditions and are thus used to demonstrate the principle feasibility of the models derived above. One sample consists of pure quartz sand with a grain diameter of about 100 to 300 μm . The other one was artificially prepared by mixing the same sand with kaolinite clay (30% clay content). Both samples were completely saturated with deionized water under vacuum and afterwards desaturated in different steps. After each desaturation step NMR measurements were conducted using the CPMG pulse sequence (see Chapter 3.1.2). The pure sand was desaturated with different steps using a pressure plate apparatus (see Chapter 2.2), whereas the sand-clay mixture was desaturated by evaporation under atmospheric conditions. Unfortunately, samples with high clay content could not be desaturated with the used pressure plate apparatus, because the maximum pressure that could be applied was 2000 hPa (equivalent to a capillary pressure head of 20 m), which is too low to desaturate samples with high clay contents completely.

In Figure 4.6a, both the multi- and the mono-exponential approximations of the T_2 relaxation data for the saturated sand-clay mixture are shown. The maximum of the T_2 distribution and the T_2 time of the mono-exponential fit are in agreement with about 0.035 s. Figure 4.6b shows the RMS values of different data approximations as a function of the smoothness parameter λ_{smooth} . The horizontal line depicts the RMS value of the mono-exponential fit, which is almost identical to the RMS value of the optimal

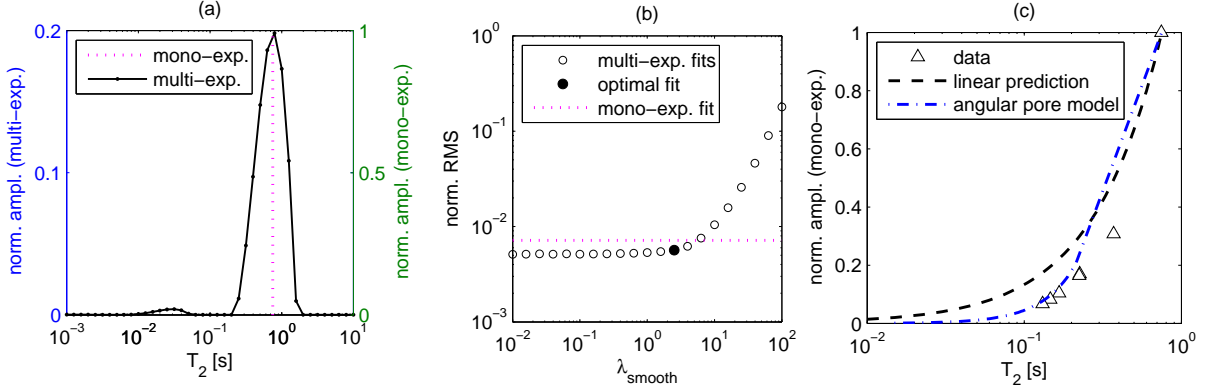


Figure 4.7: (a) NMR T_2 distribution of the saturated sand sample compared with the spectral line representing the mono-exponential approximation. (b) Determination of the optimal smoothness parameter λ_{smooth} (according to the procedure described in Chapter 3.2.3) and comparison with the relative root mean square value resulting from the mono-exponential fitting. (c) Saturation dependency of the T_2 times compared with both the linear prediction (Equation 4.18) and the prediction given by the assumption of an angular pore space (Equation 4.35).

smoothness-constrained approximation. Obviously, the data of this sample is sufficiently represented by a mono-exponential fit, i.e., all pores are of almost similar size for the entire sample. In Figure 4.6c, the T_2 times after mono-exponential fitting of the NMR measurements during the desaturation are plotted against S . The relationship between both is nearly linear. The clay particles completely fill the pore space between the sand grains such that the water content at partial saturation consists only of film water adsorbed at the clay surface. During desaturation, the thickness of these water films decreases. Consequently, the T_2 time decreases linearly with S according to the theory developed in the previous section. This result is in agreement with the data of Mattea et al. (2004) who also described a linear relationship between T_1 and S for nano- and microporous silica gels. However, because the volume of the film water depends on the internal surface of the pore system, its influence on the relaxation time is expected to be of minor relevance when coarser material is investigated.

The data of the pure sand example as shown in Figure 4.7 clearly differs from the linear relationship. In the saturated state, this sample also shows a predominantly mono-exponential behavior (Figures 4.7a and 4.7b). The T_2 times for different S are in agreement with the prediction from the desaturated angular pore model, i.e., the remaining water is bounded by capillary forces in the corners between the quartz grains. For the prediction, the cross-section of the angular pore was assumed to be an equilateral triangle, i.e., the prediction was calculated with Equations 4.35 and 4.36. The T_2 value at $S=0.32$ is an outlier that is likely caused by a non-uniform spatial distribution of the water content inside the sample. During the desaturation of quite coarse material, wa-

ter might accumulate at the bottom of the sample due to gravitational forces, as long as the sample has not yet reached the residual saturation. Thus, at the bottom of the sample the pore space might remain nearly saturated. Consequently, the contribution of these saturated parts leads to an overestimation of the T_2 time compared to the model assumption.

4.3 Adaptation of the Brooks-Corey model

So far, the discussions in this chapter and the data examples in the previous section were focussed on the NMR relaxation behavior of single pores. Now, the pore size distribution is taken into account, which is made by empirical consideration. Assuming the capillary bundle model discussed in Chapter 2.2 and 2.3, the logarithmic mean value of the NMR relaxation time distribution at partial saturation might be expected to be proportional to the effective radius r_{eff} of the partially saturated pore space:

$$T_{i,U} \propto r_{eff} \quad \text{with} \quad i = 1, 2. \quad (4.37)$$

The term $T_{i,U}$ (with $i=1$ for the longitudinal and with $i=2$ for the transverse relaxation, respectively) will from now on be used meaning the effective relaxation time at partial saturation. The expectation in Equation 4.37 is conform to Equation 3.33 for the full saturated pore space, if r_{pore} is considered to be the mean pore radius of the pore size distribution. According to the principle of estimating the saturated hydraulic conductivity K_S from the mean r_{pore} (i.e., mean T_i) following Kenyon (1997); Coates et al. (1999); Dunn et al. (1999), at partial saturation r_{eff} (i.e., $T_{i,U}$) is considered to be the governing quantity for the unsaturated conductivity K_U . The proportionality between r_{eff} and $T_{i,U}$ allows the assumption of a relationship according to the BC model (Equation 2.6):

$$S_{NMR} = \left(\frac{T_{i,U}}{T_{i,S}} \right)^\lambda = T_{i,rel}^\lambda \quad (4.38)$$

$T_{i,S}$ denotes the log mean value of the relaxation time distribution at saturation and $T_{i,rel}$ the relative relaxation time. The dependency of $T_{i,U}$ from S_{NMR} can then be formulated as a modification of Equation 3.33:

$$\frac{1}{T_{i,U}} = \frac{1}{T_{i,S}} \frac{1}{S_{NMR}^{1/\lambda}} = \rho_i \frac{A}{V} \frac{1}{S_{NMR}^{1/\lambda}} \quad (4.39)$$

Reminding the theoretical considerations in the previous sections, Equation 4.39 can be interpreted as a general formulation accounting for arbitrary pore size distributions with λ representing the usual BC pore-size-distribution index, as well as for different models to describe remaining pore water in desaturated single pores such as water films with $\lambda = 1$ (see Chapter 4.1.2) and meniscoid water with $\lambda = 2$ (see Chapter 4.1.3). The results of

Mattea et al. (2004) show that Equation 4.39 with $\lambda=1$ is valid for the T_1 relaxation in micro- and nano-porous silica glasses with quite homogeneous pore spaces, i.e., a linear relationship of $T_{1,U}$ and S_{NMR} . In contrast, the data of Ioannidis et al. (2006) exhibit a non-linear relationship for glass beads (300 μm diameter) with $\lambda > 1$.

An important issue of this work is to verify Equations 4.38 and 4.39 for more natural pore spaces. Regarding the analogy to the BC model, typical values for λ are assumed within the range of about 0.1 for inhomogeneous material up to at least 2 for homogeneous and coarse material when fitting $T_{2,U}$ as a function of S_{NMR} . With Equations 2.8 and 4.38 and assuming S_{NMR} to be similar to S_E , the following relationship of K_{rel} in dependency on the relative relaxation time $T_{i,rel}$ can be derived:

$$K_{rel} = \frac{K_U}{K_S} = S_{NMR}^a T_{i,rel}^2. \quad (4.40)$$

Following this derivation, it is possible to estimate K_{rel} from NMR relaxation times at partial saturation. Equation 4.40 was already proposed by Chen et al. (1994), who derived a model of K_{rel} as a function of $T_{1,rel}$ using Archie's law. Ioannidis et al. (2006) showed that Equation 4.40 is valid for glass beads with 300 μm diameter. So far, the application of Equation 4.40 for geologically relevant material is not validated. In this work, Equation 4.40 is tested for quartz, i.e., non-magnetic sand (see Chapter 6).

However, the standard NMR measurement in MRS is the FID experiment, which provides the T_2^* relaxation, i.e., the transverse relaxation rate enhanced by an additional component (see Equation 3.30). In addition to the discussion above, the relaxation rate $1/T_{2,deph}$ has to be taken into account when formulating the relationship between $T_{2,U}^*$ and S_{NMR} :

$$\frac{1}{T_{2,U}^*} = \frac{1}{S_{NMR}^{1/\lambda} T_{2,S}} + f(T_{2,deph}, S_{NMR}) \quad (4.41)$$

An exact physical description of $f(T_{2,deph}, S_{NMR})$ is quite complicated and an important objective for future research. In this work, an empirical approach is derived from laboratory NMR measurements in the earth's magnetic field (see Chapter 6).

Chapter 5

Estimation of WRC parameters from NMR on the laboratory scale

Normally, measurements recovering the water retention curve (WRC) of soil samples demand much time and effort. As described in Chapter 2.2, the WRC is considered to be a cumulative pore size distribution (PSD). For investigation and characterization of dynamic processes in the vadose zone, it would be a great benefit to find a method that provides the PSD, i.e., the WRC of soil samples in the laboratory much faster than conventional methods. As described in Chapter 3.2.2, laboratory and borehole NMR relaxometry has successfully been applied to recover PSDs of sandstones and limestones. In this chapter, the potential of this method to recover the WRC of loose sediments is assessed. Following the theory in Chapter 3.2.2, the NMR measurement of a saturated sample should provide all relevant information about the PSD, and the multi-exponential analysis should directly lead to an estimation of the WRC. Natural and artificial soils are investigated in this chapter with T_1 and T_2 measurements, and an interpretation scheme is suggested to estimate WRC parameters according to the VG model (see Chapter 2.3 and Equation 2.4) from the NMR relaxation time distributions. Thereby, the VG parameter n is of particular interest, because it is the essential parameter for the prediction of the relative hydraulic conductivity (Equation 2.7).

5.1 Pore size distribution from NMR compared with differential WRC

Alali (2006) investigated the dependence of NMR parameters of artificial sand-clay mixtures with various clay contents (CC). He found that the relaxation time distribution is very narrow for pure sand and higher CCs, respectively (Alali et al., 2007), whereas for smaller CCs of 1 to 10% the width of the distribution increases with increasing CC. This

feature was observed for montmorillonite (a swelling clay mineral) and kaolinite (almost non-swelling), respectively (Alali, 2008, pers. comm.) For the following introducing considerations, I use the transverse NMR relaxation data of Alali (2008, pers. comm.). These measurements were conducted with mixtures of industrial quartz sand and kaolinite clay. The CC of the samples was varied from 0 to 100 mass% (see Table 5.1). The samples were saturated with distilled water under vacuum. The NMR data was fitted with an inverse Laplace transform algorithm using the optimization toolbox of MATLAB[®] (MathWorks, 2007) to get the relaxation time distributions as estimates of the pore size distributions (PSD). Using the ROSETTA software with model ROS-BD (see Chapter 2.4 and Table 2.1), the VG parameters of the samples were predicted and the WRCs were calculated from this parameterization. Because the WRC is considered to be a cumulative PSD (see Chapter 2.2), the WRCs are differentiated for the comparison with the T_2 distributions.

Both the T_2 distributions and the differentiated WRCs as functions of the CC are plotted in Figure 5.1 for comparison. We note that the T_2 distributions of material with CCs higher than 10% are much narrower than the differentiated WRCs for the same material. When considering a complex constricted pore space rather than simple geometrical models as introduced in Chapter 4.1, the narrow NMR-PSD can be explained by the fact that NMR is much more sensitive to the pore bodies than to the pore throats. In contrast to the NMR-PSD, WRC measurements under pressure are strongly related to the pore throats; that is, a relatively big pore would hold its water during drainage, if the entry to this pore is too small for the air bubbles at a certain pressure.

Table 5.1: Textural properties of the sand-clay mixtures of Alali (2008, pers. comm.): sand content (SC), clay content (CC), and bulk density (BD).

Sample number	SC [mass%]	CC [mass%]	BD [g/cm ³]
1	100	0	1.72
2	99	1	1.69
3	97	3	1.66
4	95	5	1.71
5	93	7	1.66
6	90	10	1.65
7	88	12	1.64
8	85	15	1.65
9	80	20	1.57
10	70	30	1.55
11	50	50	1.43
12	30	70	1.26
13	0	100	1.06

When the pressure increases, the air will enter the pore immediately, while the pore drains almost completely. Consequently, the drainage behavior of the entire pore space in dependency from the applied pressure is dominated completely by the constrictions of the pore space. Obviously, an increasing content of finer material in the pore space of loose sediments leads predominantly to a broadening of the pore throat distribution, whereas the distribution of the pore bodies remains relatively narrow. However, for a CC up to 10% the shape of the T_2 distributions in Figure 5.1 is quite similar to those of the corresponding differential WRCs. In this range an estimation of the WRC from NMR seems reliable. In this chapter, the potential of NMR to estimate WRC parameters from the relaxation time distributions for full saturated material is investigated. For this objective, sand-clay mixtures with CCs ranging from 0 to 10% equivalent to the samples of Alali (2008, pers. comm.) and natural samples, respectively, were investigated with NMR and desaturated using a pressure plate apparatus under controlled conditions. Beforehand, in the following section, the reliability of the ROSETTA prediction is assessed, because the predicted parameters from ROSETTA are later used as references for assessing the NMR estimates.

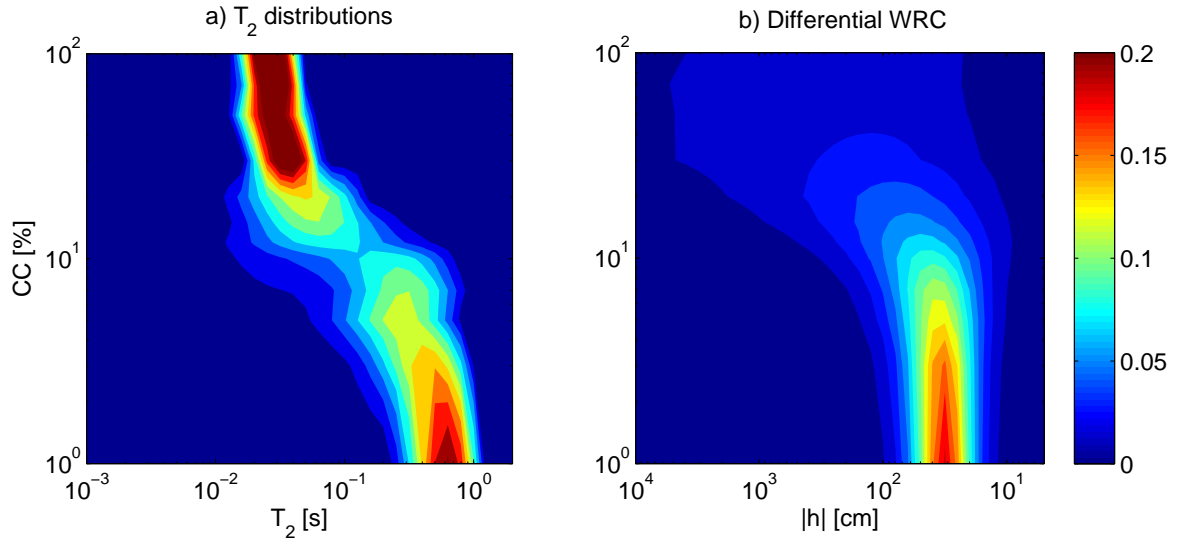


Figure 5.1: T_2 distributions of sand-clay mixtures (a) compared to the corresponding differential WRCs (b) as predicted by the ROSETTA software using the model ROS-BD (see Table 2.1).

5.2 Assessment of conventional WRC estimation for artificial samples

5.2.1 Material and methods

Various artificial samples were prepared with different portions of industrial quartz sand (F32, Quarzwerke GmbH, Germany) and kaolinite clay (Kaolin Calypso Pro 83, Caminauer Kaolinwerk GmbH) with CCs ranging from 0 - 100 mass%. Water retention measurements were conducted using a combination of both a pressure plate apparatus and a hanging water column (Facklam, pers. comm.). The applied pressure ranges from 33 to 15000 hPa, related to capillary pressure heads from -33 to -15000 cm. In Table 5.2, the soil physical properties of the sand-clay mixtures are specified. Compared to the samples listed in Table 5.1, the bulk (dry) density (BD) of the material is different due to unavoidable differences in packing during the preparation of the samples. Because the shape of the WRC depends strongly on the BD, one must expect significant deviations when comparing WRCs for the same material, but with different BDs. The WRC measurements with the sand-clay mixtures were approximated with the van-Genuchten (VG) and with the Brook-Corey (BC) model, respectively, whereby the optimization toolbox of MATLAB[®] (MathWorks, 2007) was used to minimize the corresponding objective function by means of least squares. In addition to the approximated WRC measurements, the VG param-

Table 5.2: Textural and soil physical properties of the sand-clay mixtures prepared for testing the reliability of ROSETTA predictions of WRC parameters: clay content (CC), bulk density (BD), Θ at $h=-330$ hPa (TH33), and Θ at $h=-15000$ hPa (TH1500).

Sample number	CC [mass%]	BD [g/cm ³]	TH33 [%]	TH1500 [%]
1	0	1.47	3.07	0.59
2	1	1.46	1.66	0.59
3	3	1.52	3.58	1.67
4	5	1.55	5.29	2.94
5	7	1.57	6.79	4.08
6	10	1.62	10.28	6.15
7	12	1.63	11.69	7.31
8	15	1.66	14.58	9.48
9	20	1.71	18.97	13.20
10	30	1.83	28.87	19.91
11	50	1.63	36.60	30.30
12	70	1.45	44.48	35.46
13	100	1.26	53.71	42.14

ters were also predicted by the software ROSETTA for comparison (Schaap et al., 2001). The parameters specified in Table 5.2 are used as input parameters for the ROSETTA predictions. In Table 2.1, the applied ROSETTA prediction models are listed.

5.2.2 Water retention parameters in dependency on clay content

In Figure 5.2, the WRC measurements and corresponding VG and BC approximations are compared to ROSETTA predictions for four examples (0, 5, 20, and 100% CC). The absolute value of the capillary pressure head $|h|$ is plotted on the y-axis against the saturation degree S on the x-axis.

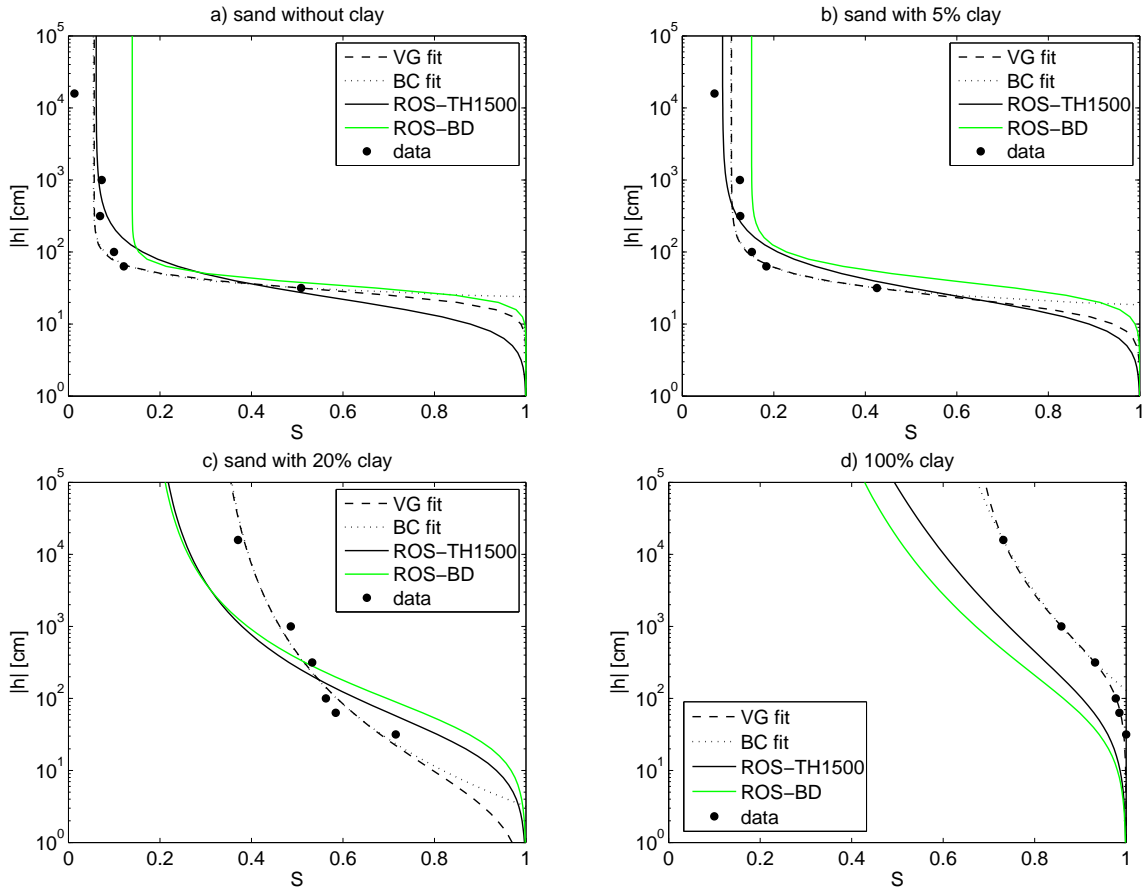


Figure 5.2: WRC measurements (black circles) of artificial sand-clay mixtures and the corresponding approximations after van Genuchten (1980) (VG, dashed lines) and after Brooks and Corey (1964) (BC, dotted lines), for comparison: the WRC predictions by ROSETTA (Schaap et al., 2001) using the models ROS-TH1500 (black solid line) and ROS-BD (green solid line), abbreviations are detailed in Table 2.1.

Similar plots of all samples investigated in this study are plotted in Appendix A (Figures A.1 and A.3) together with the predictions for all applied ROSETTA models, whereas in Figure 5.2 only the results from the models ROS-BD and ROS-TH1500 (see Table 2.1 for details) are shown. Obviously, these predictions fail for increasing CC. However, the quality of the WRC prediction by ROSETTA will be investigated later.

At first, I will focus the investigation on the dependence of the real VG and BC parameters on the CC. Figure 5.3 shows the correlations of the CC and the WRC parameters as found by fitting the measurements. The CC is plotted with logarithmic scaling on the x-axis. The pure sand sample in the plots of Figure 5.3 is accounted for at a CC value of 0.1, otherwise it could not be included at the logarithmic scale. The errorbars are calculated from the standard error multiplied by 2, i.e., they represent the 95% uncertainty intervals. As one would expect, the residual saturation degree S_R as found with both the VG (Figure 5.3a) and the BC model (Figure 5.3d) increases with increasing CC, from about 5% for 0 - 3% CC to about 65% (VG) and 55% (BD) for the pure clay. The differences in S_R of both WRC models can be explained by the natural uncertainty of the estimates for higher CCs: Because samples with high CC remain saturated also at relatively high pressures (see as example the data of the pure clay sample in Figure 5.2d), the 'effective' information content of the measured WRC decreases. Consequently, the quality of the parameter approximation gets worse. A further problem is the asymptotic nature of the parameter S_R in both models. For the case that the measurements of S at higher pressures do not include this asymptotic behavior, the fitting parameter S_R will be determined by the fitting algorithm almost randomly, at least with large uncertainty. This is also the reason for the unrealistic small values of S_R at a CC of 30% and 70% as fitted by both the VG and the BC model.

The parameters representing the PSD indices in both models (i.e., n for the VG model, Figure 5.3b and λ for the BC model, Figure 5.3e) tend to decrease with increasing clay content, which was also expected beforehand. Both parameters are the larger, the more homogeneous the pore space is. Thus, with increasing CC the decrease of both n and λ is reasonable, and these parameters are obviously positively correlated to each other. However, the decreasing trend of both with increasing CC is nonlinear. We observe a very slight decrease for n and λ from 0 to 7% CC, whereby the values of n decreases from about 4 down to 3 and the values of λ from about 2.5 down to 1.7. At CCs in the range of 7 to 30% the decrease is much stronger, whereas for CCs higher than 30% the parameters n and λ do not change significantly. With a CC of 30%, the entire pore space of the sand is completely filled with clay, and therefore the effective pore size of the material is solely controlled by the interspace between the clay particles. With CCs higher than 30% the pores do not change in size, only in number, that is, only the amount of water that is bounded to these pores (represented by S_R) increases. Also the air entry point h_0 of the BC model (Figure 5.3f) and the corresponding parameter α in the VG model (Figure 5.3c) do not significantly change for CCs higher than 30% for the same reason like the parameters n and λ . Both h_0 and α are expected to be strongly related to the effective

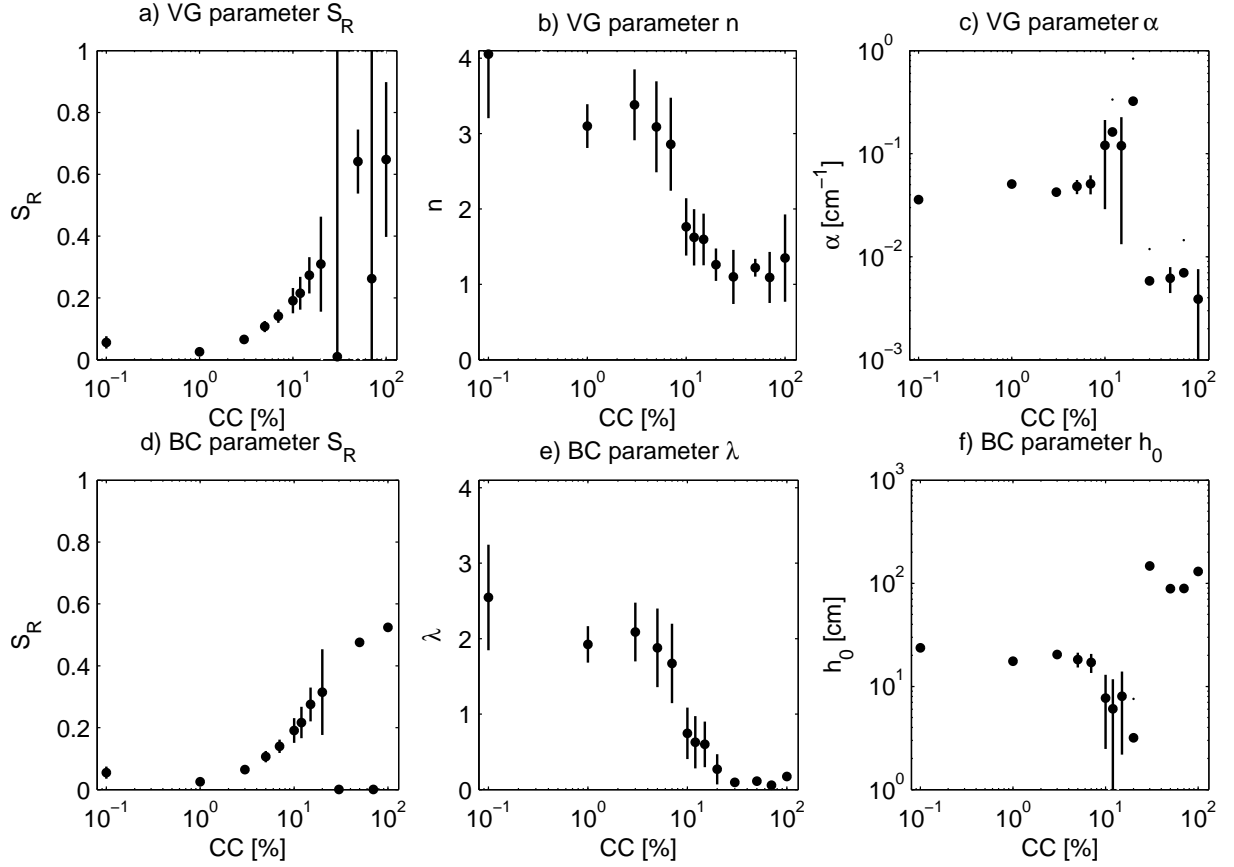


Figure 5.3: WRC parameters resulting from the approximation of the WRC measurements after van Genuchten (1980) (VG, top) and after Brooks and Corey (1964) (BC, bottom) in dependence on the clay content (CC).

pore size coming along with varying CCs. It is further expected that α is negatively correlated with h_0 , which is indeed the case here as proved in the next section. Because water is kept in the pores against the entering air with capillary forces being the stronger, the smaller the pore is, h_0 is generally expected to increase with decreasing effective pore size, at least for CCs smaller than 30%. However, this expectation is not verified by the data in Figure 5.3c and 5.3f, because the WRCs close to $S=1$, i.e., close to the air entry point, are generally sampled much too rough to fit the corresponding parameters α and h_0 adequately. This is clearly visible for the example in Figure 5.2c and for the others in the Appendix (Figures A.1 to A.3), respectively.

5.2.3 Correlation of VG and BC parameters

The parameters of the VG and the BC model are correlated in Figure 5.4,. The error bars represent their 95% confidence intervals. The correlation coefficient R_{corr} is shown in the title of each subplot. The parameter P_0 in the brackets represents the result of testing the probability of the no-correlation hypothesis for each data set (using the T-test, Schönwiese (2000)). The smaller the quantity P_0 is, the larger the significance of the correlation is. Usually, a value of $P_0 < 0.05$ is considered to represent the failure of the no-correlation hypothesis, that is, the probability of the hypothesis of no correlation is smaller than 5%. In this case, the hypothesis that a significant correlation really exists is considered to be verified.

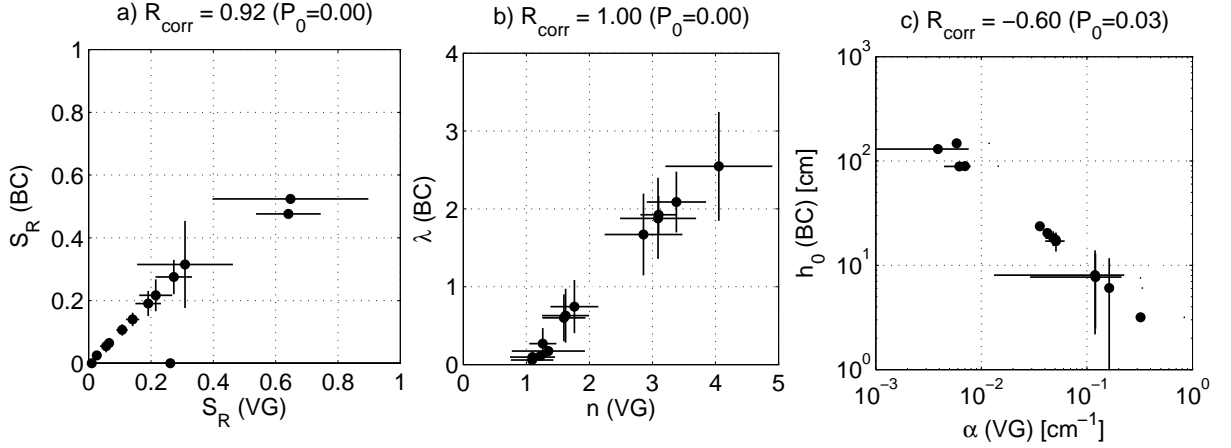


Figure 5.4: Correlation of fitted VG and BC parameters for artificial sand-clay mixtures.

Obviously, the S_R values of both models, as well as the PSD indices (n for the VG and λ for the BC model) are positively correlated. The parameter S_R is identically determined by both models within the uncertainty intervals. Between n and λ the relationship $n = \lambda + 1$ exists, which corresponds to the expectation for the constraint VG model (Haverkamp et al., 2005). For the parameter h_0 (BC) and α (VG), a negative correlation is found, which also corresponds to the expectation (Morel-Seytoux et al., 1996).

5.2.4 Comparison of WRC measurements and estimations by ROSETTA

In the following section, VG parameter predictions by ROSETTA are used as references to assess the NMR based estimations. In this section, the plausibility of ROSETTA predictions in dependence on the CC is tested with the data base introduced above. Beside the contents of sand and clay, also the bulk dry density and the water contents at

certain capillary pressures resulting from the WRC measurements presented above were used as input parameters for the ROSETTA predictions (see Tables 2.1 and 5.2).

In Figure 5.5, the results of the ROSETTA prediction using the models ROS-BD and ROS-TH1500 (see table 2.1) are correlated with the parameters found by fitting the real WRC measurements. In the legend of each subplot, the correlation coefficient R_{corr} is shown, as well as the probability of the no-correlation hypothesis P_0 . The results from the models ROS-SSC and ROS-TH33 can be found in the Appendix (Figure A.4). These are very similar to the results of ROS-BD, and are not further discussed here. Except for α , the correlation between the ROSETTA predictions and the real values is verified. However, the only parameter that is reliably estimated, i.e., that matches the identity compared to the real values within the error bars (i.e., 95% uncertainty intervals) is the parameter n as predicted with model ROS-BD (Figure 5.5b). For the other parameters, prediction and reality are not identical meaning that systematic deviations must be considered here. Schaap et al. (2001) have also shown that the prediction of n with ROSETTA is much more accurate compared to Θ_R , Θ_S , and α . For S_R , the ROSETTA prediction tends to overestimate S_R for small CCs, whereas for a CC higher than 30% S_R

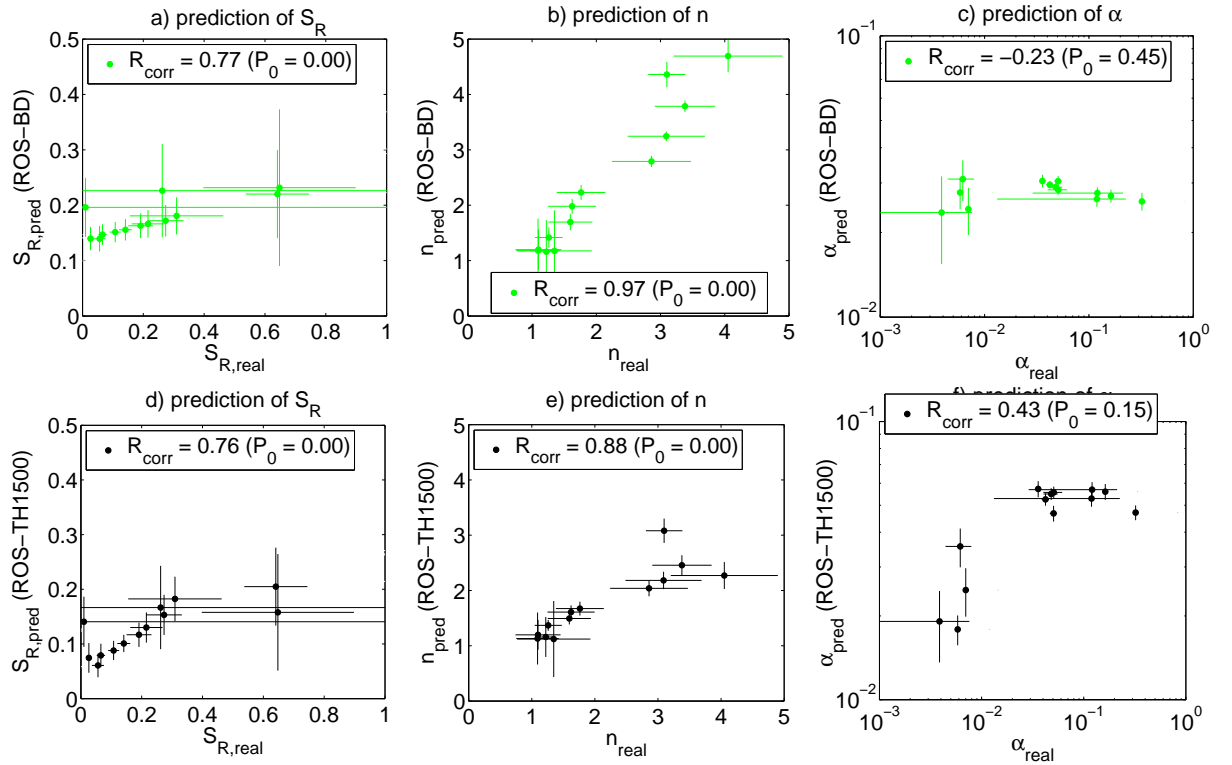


Figure 5.5: VG parameters predicted by ROSETTA compared to the 'real' parameters as found by fitting the corresponding WRC measurements of artificial sand-clay mixtures, predictions with ROSETTA models ROS-BD (top) and ROS-TH1500 (bottom), abbreviations are detailed in Table 2.1.

is underestimated. Model ROS-TH1500 shows a better agreement with the real values in the CC range of 3 to 30% (Figure 5.5d). However, the n prediction using this model obviously tends to underestimations (Figure 5.5e) for the artificial samples of this study. This is contrary to the results of the study of Schaap et al. (2001), who concluded that the uncertainties of the ROSETTA prediction for all VG parameters should decrease with increasing number of input parameters. Although for the α prediction of all ROSETTA models a correlation of the predicted and the real parameters cannot doubtlessly be verified, the P_0 value for model ROS-TH1500 indicates a smaller probability of the no-correlation hypothesis compared to model ROS-BD. However, for both models one must consider α to be unpredictable by ROSETTA, when working with artificial sand-clay mixtures. S_R also seems to be a parameter that cannot be reliably predicted by ROSETTA without systematic errors. Thus, in practice it is always recommended to determine this parameter by corresponding measurements, rather than to trust in predictions. One may remind here the usual estimation of Θ_R from NMR measurements as described in Chapter 3.2.2. For determining the cutoff value in the relaxation time distributions, calibration measurements of S_R are also recommended rather than using default cutoff values.

For the further investigations in this work, I conclude that the VG parameters S_R and α predicted by ROSETTA are not qualified for the use as reference values. However, regarding the prediction of the parameter n , which behaves almost independently from S_R and α when approximating WRC measurements (Haverkamp et al., 2005), the ROSETTA software provides accurate results. I conclude that the use of the ROSETTA models ROS-SSC, ROS-BD, and ROS-TH33 can provide n values that allow for assessing the NMR-based estimations of n . For this reason, and because n is the governing VG parameter when estimating the relative hydraulic conductivity from the VG model (see Equation 2.7), the discussion in the next section is only focussed on that parameter. As already mentioned in Chapter 2.4, the direct prediction of the unsaturated hydraulic conductivity with ROSETTA is, in principle, also possible. However, the uncertainty intervals of these predictions are about one order of magnitude making them unacceptable for the use as references here (Schaap et al., 2001).

5.3 WRC estimation from NMR relaxation time distribution at saturation

5.3.1 Material and methods

Industrial quartz sand was mixed with different portions of kaolinite clay from 0 to 10% just as for the investigations discussed above. In addition, seven natural samples were taken from different test locations. The textural and soil physical specifications of the samples are listed in the Tables 5.3 and 5.4 (see also the Tables 5.1 and 5.2 for comparison

of the sand-clay mixtures). The grain size distribution curves of the natural samples are depicted in Figure 5.6. The test sites Nauen and Buch are located near Berlin, Germany. Schillerlage is in the north of Hannover, Germany. The soil samples from these locations are characteristic for the northern germany and consist mainly of fluvial Quaternary sand. The location Gasthof is located in Saxonia, Germany, where the geology is characterized by aluvial Quaternary sediments (loess), i.e., loamy soils with high clay and silt contents.

The investigations were focussed on the direct comparison of NMR and common WRC measurements. Thus, the samples were prepared such that both methods could be applied to the same sample with the same material. In this way, systematic errors resulting from variations of the bulk density (i.e., initial water content at saturation Θ_S) of different samples with the same material are avoided.

Table 5.3: Textural properties of the sand-clay mixtures prepared for the combined investigations of NMR and WRC measurements: clay content (CC), bulk density (BD), and Θ at $h=-330$ hPa (TH33).

Sample number	CC [%]	BD [g/cm ³]	TH33 [%]
1	0	1.61	6.43
2	1	1.58	6.68
3	3	1.56	8.71
4	5	1.62	8.60
5	7	1.56	10.28
6	10	1.60	12.56

Table 5.4: Textural properties of the natural samples for the combined investigations of NMR and WRC measurements: Contents of clay, silt, and sand, bulk density (BD), and Θ at $h=-330$ hPa (TH33).

Sample name	Location -	Depth [m]	Clay [%]	Silt [%]	Sand [%]	BD [g/cm ³]	TH33 [%]
nau02	Buch	0.2	0	26	74	1.71	18.28
nau07	Buch	0.7	0	10	90	1.67	4.96
buch02	Nauen	0.2	0	11	89	1.39	13.59
buch07	Nauen	0.7	0	7	93	1.73	4.14
sch05	Schillerslage	0.5	0	4	96	1.64	3.65
gast005	Gasthof	0.05	8	79	13	1.47	31.75
gast05	Gasthof	0.5	8	62	30	1.51	28.48

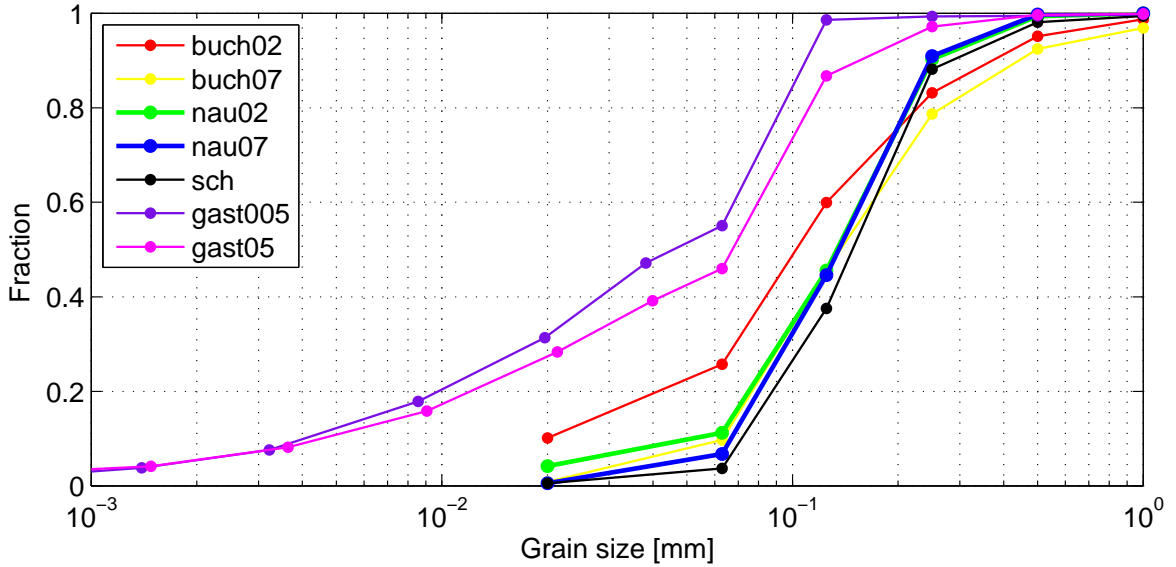


Figure 5.6: Grain size distribution of the natural samples.

Although not usual for WRC measurements using a pressure plate apparatus, the sample holders were made of polycarbonate tubes of 3.6-cm diameter with a height of 5.5 cm fitting the dimension of the sample inlet of the Maran Ultra NMR apparatus (Resonance Instruments, UK), which was used in this work for the NMR measurements. Filters made of microfiber tissues were mounted at the bottom of the sample holders to realize the hydraulic contact of the sample material and the ceramic plate of the pressure plate apparatus. The samples were saturated with distilled water under vacuum to avoid residual air bubbles during the saturation process. After the initial NMR measurements at saturation, the samples were drained under controlled overpressure according to the usual pressure plate experiment (see Chapter 2.2). During the pressure plate experiments, the top of the sample tubes were open to allow air entry into the pore space, whereas sealing covers at top and bottom during the NMR experiments avoided additional unwanted water losses due to evaporation.

The pressure plate apparatus used in the study is depicted in Figure 5.7. The equipment consists of commercially available components with a self-built pressure reducing installation. The overpressure was applied using a high-pressure vessel with compressed air. Depending on the applied pressure, either one or two pressure reducers could manually be switched on demand. Two different ceramic plates with air entry points of 1000 and 3000 hPa were used depending on the actual pressure step. The applied pressure for the natural samples and for the pure sand sample, respectively, ranges from 63 hPa to 2000 hPa in six logarithmically equidistant steps.



Figure 5.7: Pressure plate apparatus and pressure reducing installation used in combination with NMR measurements at sample tubes of 3.6-cm diameter with a height of 5.5 cm.

For the WRC measurements of the sand-clay mixtures, the pressure steps at 63 and 2000 hPa were applied only. As described below, these two steps are sufficient to calibrate the NMR data for the estimation of the WRCs from the relaxation time distribution at saturation. To reach a state of equilibrium after the application of each pressure step, a waiting period of up to a view days (about 14 to 21 days depending on the actual pressure) was necessary until no more water was observed at the outlet of the pressure vessel. After each pressure step, the samples were weighed to determine water content and saturation degree. Afterward, they were sealed to conduct the NMR measurements. Except for the Gasthof samples, this measurement scheme could be successfully applied. The two Gasthof samples exhibit water retention properties that could not be investigated with the equipment described above, because a pressure of up to 15000 hPa was necessary to desaturate them adequately. Thus, the WRC measurements for these samples were conducted similar to the procedure described in Chapter 5.2 (Facklam, pers. comm), and the NMR measurements for these two samples were conducted only at the state of saturation.

The NMR measurements were conducted using the CPMG sequence for the transverse relaxation and using the inversion recovery sequence for the longitudinal relaxation (see Chapter 3.1.2 for details). The duration during the 180° -pulses of the CPMG sequence was set to $150 \mu\text{s}$. To achieve an adequate signal-to-noise ratio of the NMR response signals, the stacking rate was initially set to 100 for the measurements of the transverse relaxation and to 8 for the measurements of the longitudinal relaxation. During the experiments, the number of stacks were adjusted upward to account for the decreasing signal due to the decreasing water content. Finally, the maximal number of stacks for the measurements at residual saturation was 900.

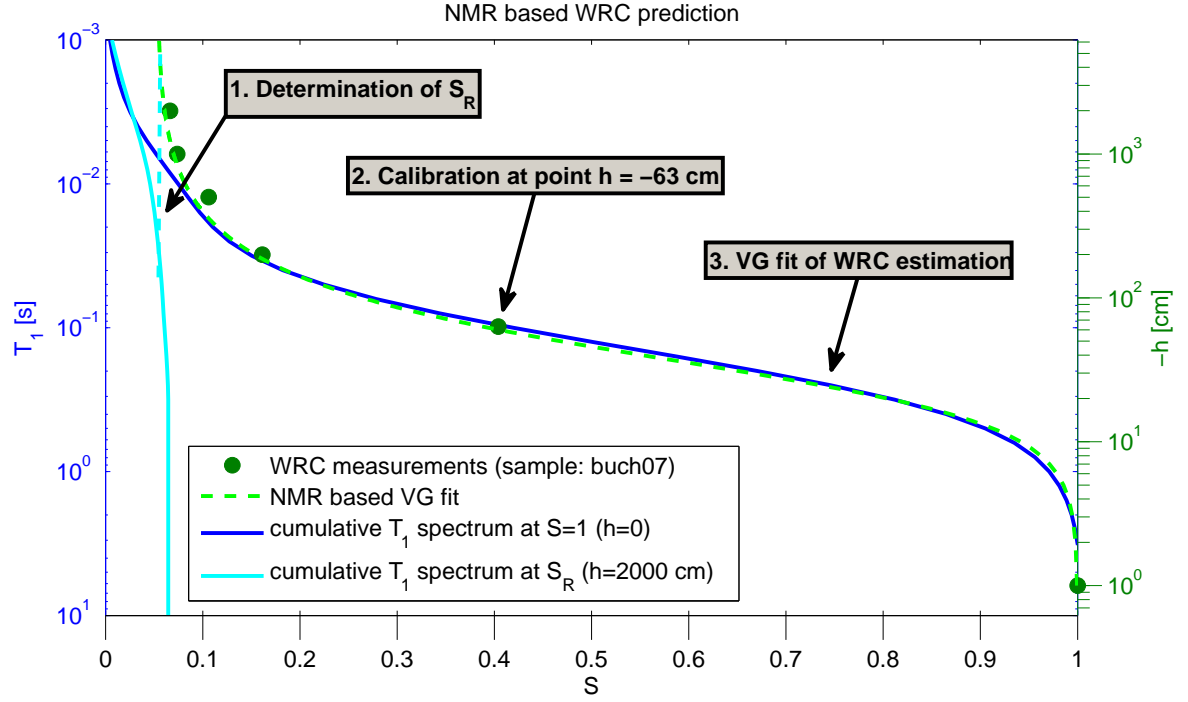


Figure 5.8: Description of the procedure for estimating the WRC from the cumulative NMR relaxation time distribution exemplarily for the sample buch07, see detailed explanations in the text below.

The NMR data approximation (an inverse Laplace transform according to the principle described in Chapter 3.2.3) and the approximation after van Genuchten (1980) to the processed NMR data, respectively, were realized with a conjugated gradient algorithm using the MATLAB[®] optimization toolbox (MathWorks, 2007). The inverse Laplace transform results in a spectral analysis of the NMR data of the form $I_n = f(T_n)$. For simplification, the notation T is used here for both the transverse and the longitudinal relaxation time. The VG fit is realized at the base of the cumulative distribution at saturation for each sample. Thereby, the distribution is normalized with respect to the NMR signal amplitude $E_{0,S=1}$ to values between 0 and 1, i.e., to values representing S_{NMR} according to Equation 4.1:

$$S_{NMR}(T_n) = \frac{1}{E_{0,S=1}} \sum_{m=1}^n I_m(T_m). \quad (5.1)$$

The WRC for the samples was estimated in two steps that are adapted from the usual procedure of estimating the pore size distribution (PSD) from NMR for sandstones (see Chapter 3.2.2). In Figure 5.8, the applied processing steps are depicted at the sample buch07 exemplarily.

1. **Determination of the residual saturation degree S_R :** The water saturation degree at $h = -2000$ cm (highest pressure step in this experiment) was interpreted as the residual saturation degree S_R and was determined according to Equation 4.1. This procedure is equivalent to the scheme described in Chapter 3.2.2 (Figure 3.3) to discover the cutoff value for determining the residual water content of sandstones. After the determination of S_R , the cumulative distribution is modified such that the relaxation times in the distribution smaller than the cutoff value T_{co} are associated with S_R :

$$S_{NMR}(T_n) = \begin{cases} S_{R,NMR} + \sum_{m=co}^n I_m(T_m), & T_m > T_{co} \\ S_{R,NMR}, & T_m < T_{co} \end{cases} \quad (5.2)$$

2. **Calibration of the distribution at the base of the pressure step with $h = -63$ cm:** In Chapter 3.2.2, the common procedure was described for estimating PSDs of sandstones from NMR data calibrated at the base of the mercury induction measurements (Figure 3.2). Similar to this procedure, the cumulative relaxation time distributions in this work are shifted such that they cross the point $S(h = -63 \text{ cm})$ found by the measurement with the pressure plate apparatus. The shifting of the distributions at the logarithmic scale can be considered as a kind of calibration legitimated by combining Equations 2.2 and 4.37, i.e., the proportionality between the relaxation times and the reciprocal capillary pressure:

$$T_{1,2} \propto \frac{1}{|h|}. \quad (5.3)$$

3. **Approximation with the van Genuchten (VG) model:** The NMR based WRC estimations resulting from 1. and 2. are finally fitted using the VG model according to Equation 2.4.

The VG fitting parameters derived from the NMR data are compared to the predictions by the ROSETTA software. The corresponding input parameters for ROSETTA as derived from the texture and the WRC measurements, respectively, are listed in the Tables 5.3 and 5.4. A direct approximation of the WRC measurements was not possible, because the resulting WRC data base consists of only three data points for each artificial and six for each natural sample in a range too small for a reliable VG fit.

5.3.2 Dependency of T_1 and T_2 distributions on matric potential

The application of the inverse Laplace transform at the NMR data yields the T_1 and T_2 relaxation time distributions. In Figure 5.9, these distributions are shown for the investigated natural samples. For each sample and relaxation type (i.e., T_1 on the left hand side and T_2 on the right hand side of Figure 5.9), seven distributions are depicted corresponding to the desaturation steps at $h = -63, -100, -200, -500, -1000, -2000$ cm, and the measurement at saturation. The distributions are normalized with respect to the initial NMR amplitude E_0 at saturation, i.e., the areas under the spectral curves equal the individual NMR saturation degree (see Equation 4.1). We note that, according to the theory, the desaturation for all samples starts in the bigger pores related to longer relaxation times of the distributions, whereby no significant differences between the T_1 and the T_2 relaxation can be observed.

Considering the derivations in Chapter 4.1, one might expect the appearance of new relaxation regimes corresponding to residual water remaining as films or meniscoid water at the pore walls. As shown in Chapter 4.2, this is the case if the NMR signal at saturation is predominantly of mono-exponential shape (see Figures 4.6 and 4.7). Such a behavior cannot be doubtlessly observed for the natural samples investigated here, neither for the T_1 , nor for the T_2 relaxation. For the samples from Schillerslage (depth: 0.5 m) and Nauen (depth: 0.7 m), water appears at about 0.02 to 0.05 s in the desaturated T_1 distributions and at about 0.01 to 0.02 s in the desaturated T_2 distributions, whereas the distribution at saturation does not show any water in this range. However, it cannot be decided whether these features are of physical origin or just inversion artefacts. Thus, one might consider that the relaxation during desaturation for the natural samples investigated here is dominated by the natural pore size distribution, i.e., the drainage starts with the bigger pores, while the smaller ones remain completely filled. Capillary water bounded at the pore surface as film or meniscoid water can be neglected. This is, however, not the general case, which can be shown with the following examples.

In Figure 5.10, the relaxation time distributions of three examples among the artificial samples are shown. An overview of the distributions of all sand-clay mixtures is given with the Figures A.5 and A.5 in the Appendix. Figure 5.10a shows the results for the pure sand without any clay, and Figure 5.10b and 5.10c the results for the sample with 5% clay and with 10% clay, respectively. Regarding the spectral behavior of the desaturation steps, no significant deviations between the T_1 and the T_2 distributions can be found as observed for the natural samples shown above. Comparing the T_1 and T_2 distributions for the pure sand sample, the curves show a slightly different width, which is due to the different noise levels of the T_1 and T_2 measurements. This causes different smoothness constraints for the approximation of the NMR data (see Chapter 3.2.3). Such an obvious difference between the broadness of T_1 and T_2 distributions is expected only for predominantly mono-exponential signals, i.e., the NMR signal could also adequately be approximated by a mono-exponential approach (see Figures 4.6 and 4.7 and the cor-

5.3. WRC estimation from NMR relaxation time distribution at saturation

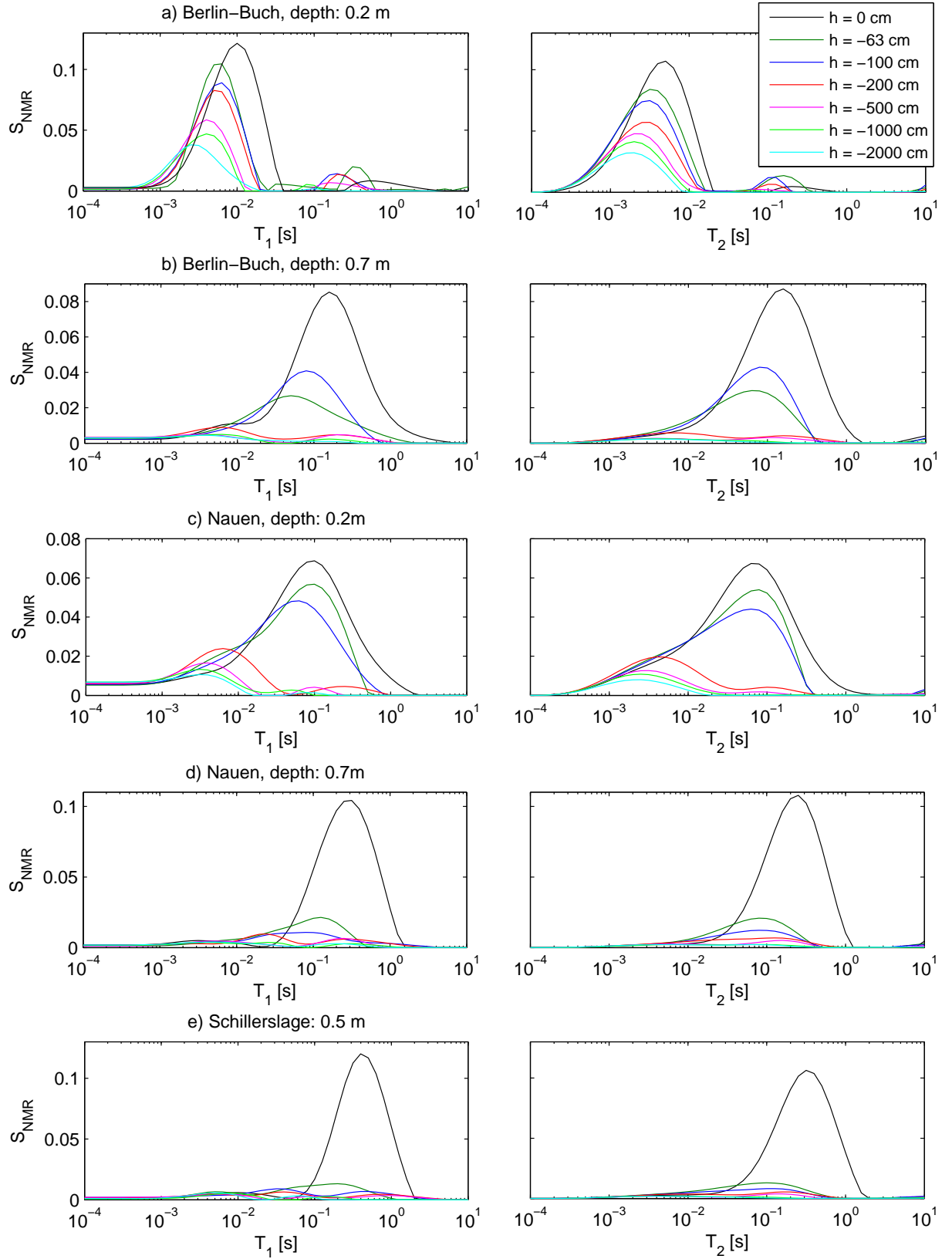


Figure 5.9: NMR relaxation time distributions of soil samples from different test sites at varying capillary pressure heads h , T_1 on the left and T_2 on the right hand side.

responding explanations). In this case, the regularization during the multi-exponential fitting enforces a smooth shape, and the broadness of the resulting distribution is solely influenced by the noise level of the data. NMR data with 'real' multi-exponential behavior, i.e., caused by a significant pore size distribution, must be expected to exhibit relaxation time distributions with similar broadness for different noise levels, as long as the data quality allows for a reliable multi-exponential fit.

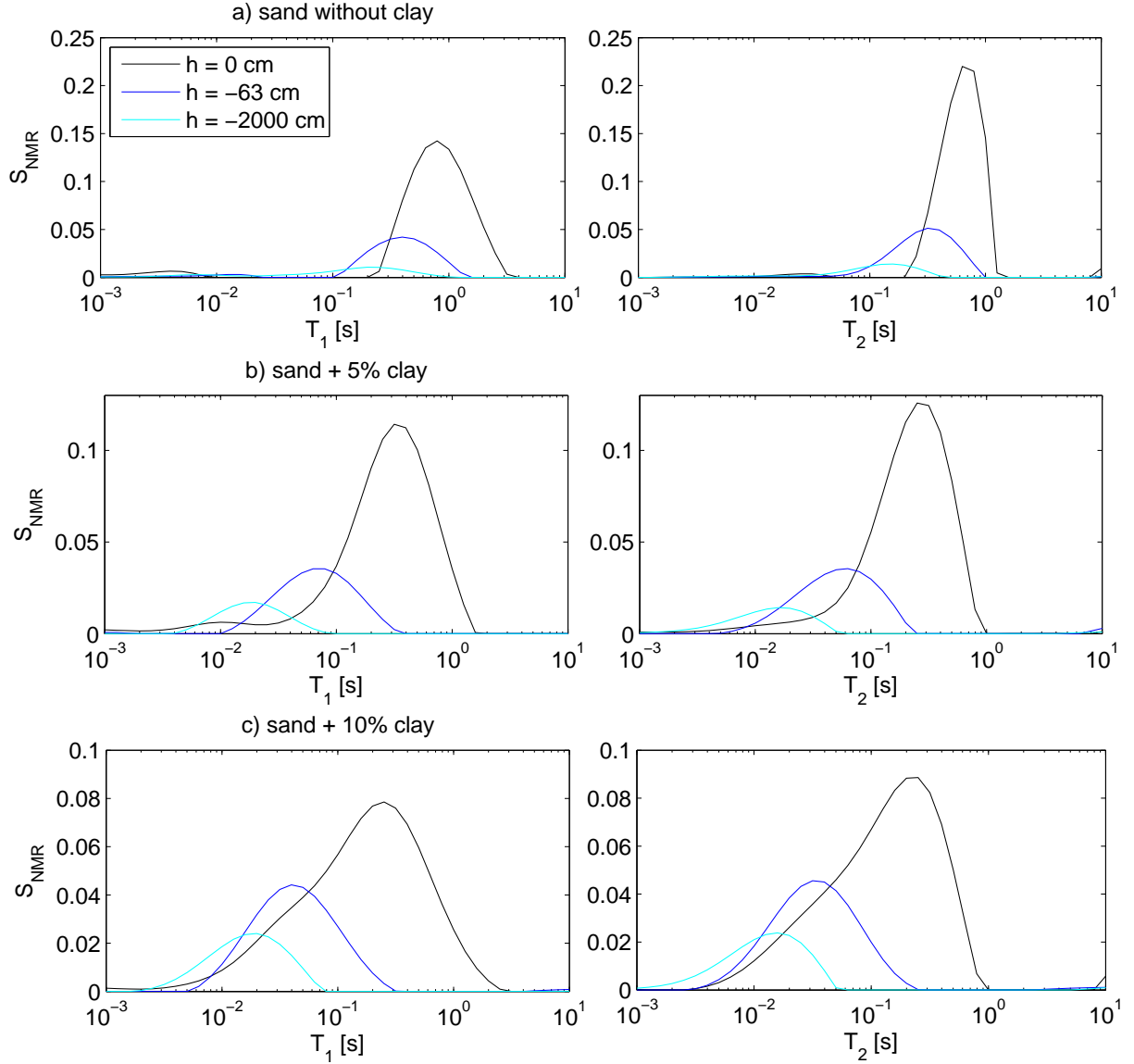


Figure 5.10: NMR relaxation time distributions of artificial sand-clay mixtures at varying capillary pressure heads h , T_1 on the left and T_2 on the right hand side.

For the examples in Figure 5.10, we observe an obvious shift of the distributions at partial saturation compared to the distribution at $S = 1$. According to the theory derived in Chapter 4.1, this behavior indicates that new relaxation regimes appear due to the presence of film or meniscoid water. It was proved in Chapter 4.2 that a mono-exponential representation of the NMR data for pure sand can reliably be explained by a pore model with angular shape (see also Figure 4.7). With increasing clay content, the shift is more and more caused by film water related to the increasing pore surface-to-volume ratio.

For the following considerations the question arises, whether the NMR saturation degree S_{NMR} or the water content Θ_{NMR} should be used for the WRC estimations. The corresponding calibration measurement to determine the absolute water content with NMR might be an additional error source, which contributes to the entire uncertainty of the calculations and propagates during the approximations. This possible error of Θ_{NMR} compared to the error of S_{NMR} is investigated and assessed in the following.

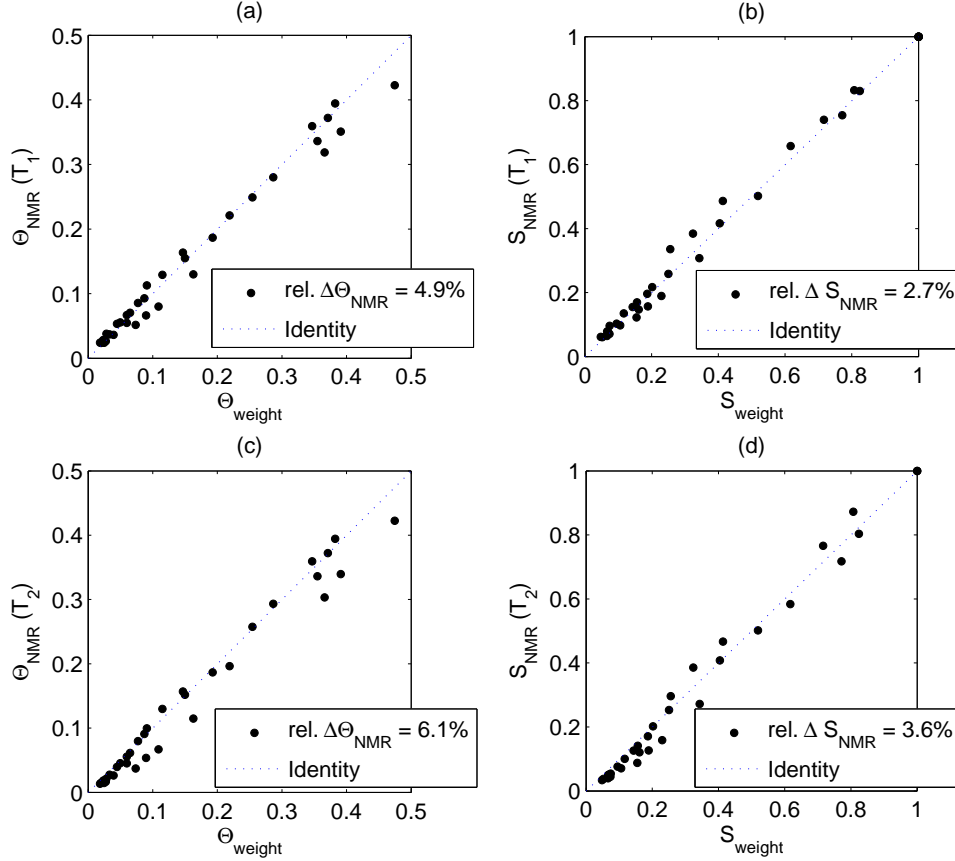


Figure 5.11: NMR-based results for the water content (Θ_{NMR} , a and c) and for the saturation degree (S_{NMR} , b and d) of the natural samples compared to the corresponding values as found by weighing, results of the T_1 relaxation measurements on the top (a and b) and results of the T_2 relaxation measurements at the bottom (c and d).

In Figure 5.11, both Θ_{NMR} and S_{NMR} as derived from the T_1 and the T_2 distributions of all measurements with the natural samples shown above are correlated with the real values as found by weighing (Θ_{weight} and S_{weight}). Obviously, both NMR-based quantities are correlated with the real values and are orientated along the identity line, i.e., no systematic shifts or erroneous trends are observed. However, the relative scattering of the Θ_{NMR} data points around the identity line is almost two times larger than for the S_{NMR} values. To quantify the corresponding uncertainties $\Delta\Theta_{NMR}$ and ΔS_{NMR} , their normalized deviations from the identity line are calculated assuming that Θ_{weight} and S_{weight} are the real values determined with negligible uncertainties. The dataset consists of $n=35$ measurements for both the T_1 and the T_2 relaxation:

$$\begin{aligned}\Delta\Theta_{NMR} &= \frac{1}{\Phi_{mean}} \sqrt{\frac{\sum(\Theta_{real} - \Theta_{T_i})^2}{n}} \\ \Delta S_{NMR} &= \sqrt{\frac{\sum(S_{real} - S_{T_i})^2}{n}}\end{aligned}\tag{5.4}$$

For the following investigations, I conclude that it is a better to choose the NMR saturation degree S_{NMR} for the WRC estimations, as well as for the comparison with the reference measurements and with the predictions by the ROSETTA software, respectively. For a possible practical use of NMR-based WRC estimations in the future, a calibration to derive absolute estimates for the water content remains, of course, a necessary and important issue. However, in this work the main issue is the plausibility of NMR-based WRC estimations and thus, interpretation schemes are preferred here that avoid any unnecessary error sources. Consequently, I use solely the S_{NMR} values from now on, and I abstain from absolute estimates of Θ_{NMR} for the direct comparison with the references.

5.3.3 Comparison of WRC predictions from NMR and ROSETTA

The results of the WRC estimations for the sand-clay mixtures and the ROSETTA predictions as references are shown in Figure 5.12. The NMR estimations are in good agreement with the reference curves. In Figure 5.13, the NMR-based WRC estimations (i.e., represented by their VG approximations) of the natural samples are compared to their WRC measurements and to the ROSETTA predictions, respectively. The model ROS-TH33 (see table 2.1) was used for these ROSETTA predictions. The results of other ROSETTA prediction models, as well as the cumulative NMR distributions as the basis for the VG estimation can be found in the Appendix (Figure A.7). For the samples with less silt and clay contents (i.e., samples nau02, nau07, buch07, and sch05, see Table 5.4), the NMR-based estimations for both the T_1 and the T_2 relaxation measurements are in good agreement with the WRC measurements. Compared to these samples, the sample buch02 has a relatively high content of finer grains, which is the reason for the shift of the corresponding WRC measurement toward higher $|h|$ on the one hand, and the smaller

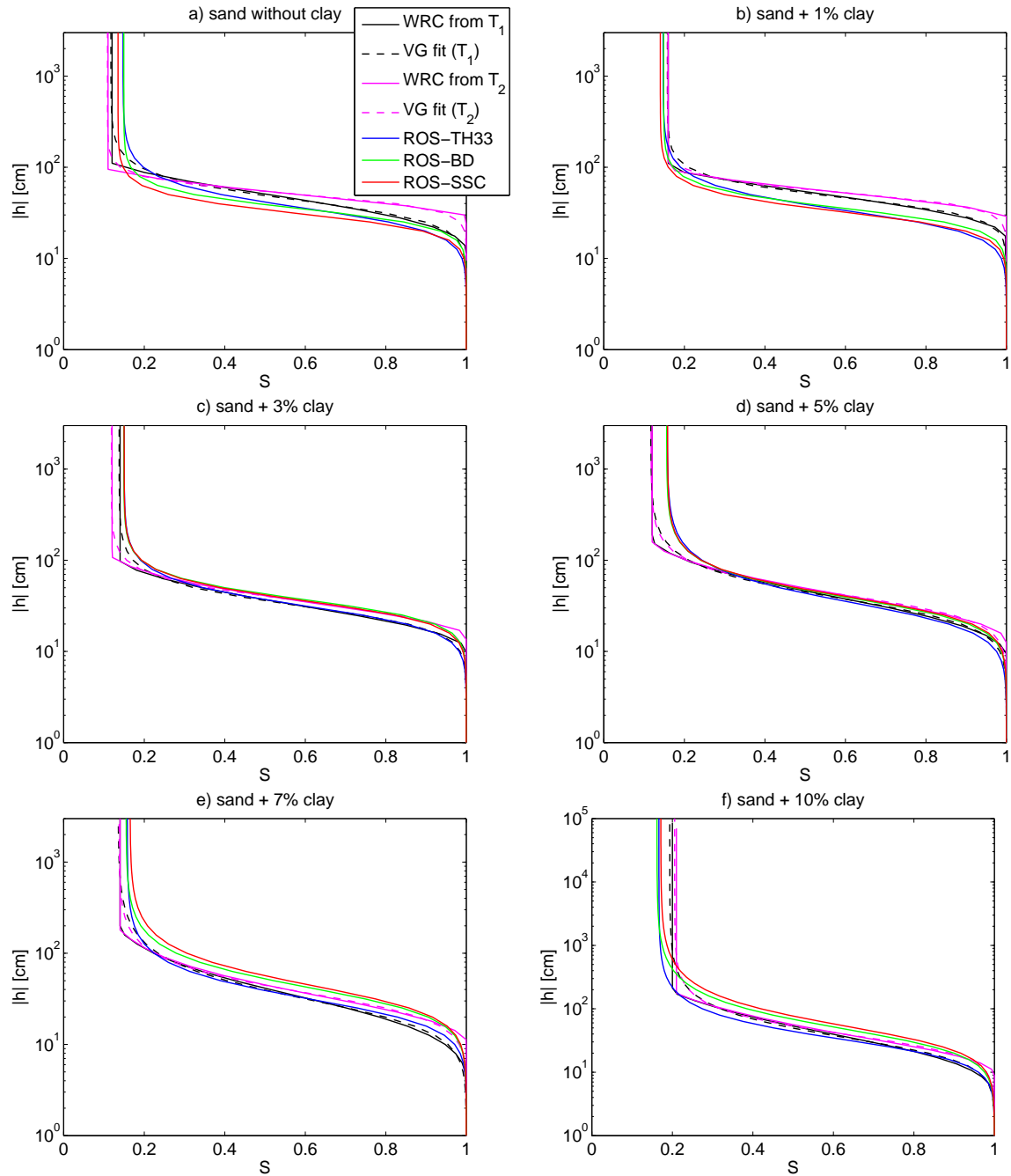


Figure 5.12: WRC estimations from T_1 and T_2 distributions (black and magenta solid lines) and the corresponding fit after van Genuchten (1980) compared to WRC predictions from ROSETTA (Schaap et al., 2001) with the prediction models ROS-SSC (red solid line), ROS-BD (green solid line), and ROS-TH33 (blue solid line), abbreviations are detailed in Tab2.1.

slope of S_{NMR} with decreasing $|h|$ on the other hand. The NMR prediction fails in this case, the predicted slope of the WRC is much larger than the measurements.

It was expected beforehand in this chapter (Section 5.1) that WRCs can be estimated from NMR relaxation time distributions only for soils with small contents of finer grains, i.e., with silt and clay contents below 10%. To prove this assumption, I want to show finally the WRC estimations from the NMR relaxation time distributions at saturation for the natural samples from the location Gasthof, as well as for some examples from the data set of Alali (2008, pers. comm.), which was already depicted as surface plot in Figure 5.1a. For the WRC estimations from these distributions, the procedure described in Figure 5.8 was modified slightly accounting for the fact that S_R could not be determined for these samples. Instead the S_R value predicted by ROSETTA was used. On the other hand, the calibration value for shifting the cumulative NMR distributions was determined from the samples listed in Table 5.2, i.e., different samples prepared with the same material. Strictly speaking, an unknown systematic error must be expected here due to the fact that different samples even with the same material will likely exhibit different bulk densities. However, this systematic error will mainly affect the determination of the VG parameter α , and is expected to have a minor effect on the parameter n controlling the slope of the WRC (Haverkamp et al., 2005). Thus, the comparison of the resulting NMR based WRC estimations with the ROSETTA predictions is nevertheless legitimate.

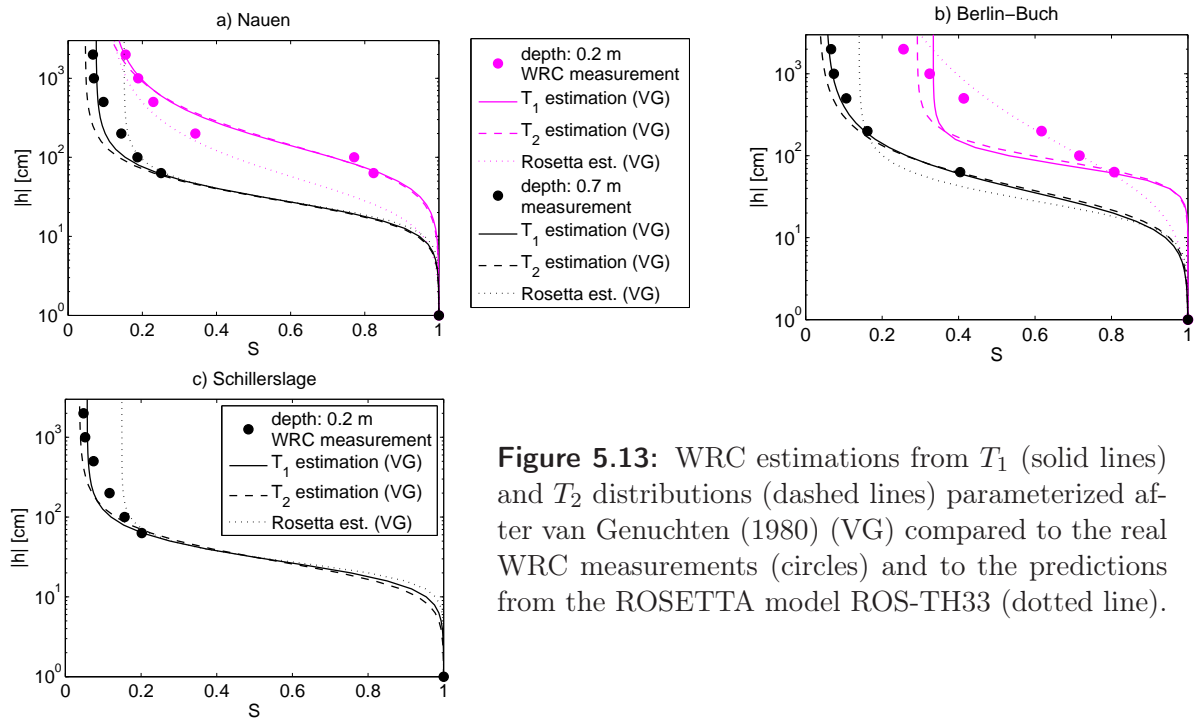


Figure 5.13: WRC estimations from T_1 (solid lines) and T_2 distributions (dashed lines) parameterized after van Genuchten (1980) (VG) compared to the real WRC measurements (circles) and to the predictions from the ROSETTA model ROS-TH33 (dotted line).

5.3. WRC estimation from NMR relaxation time distribution at saturation

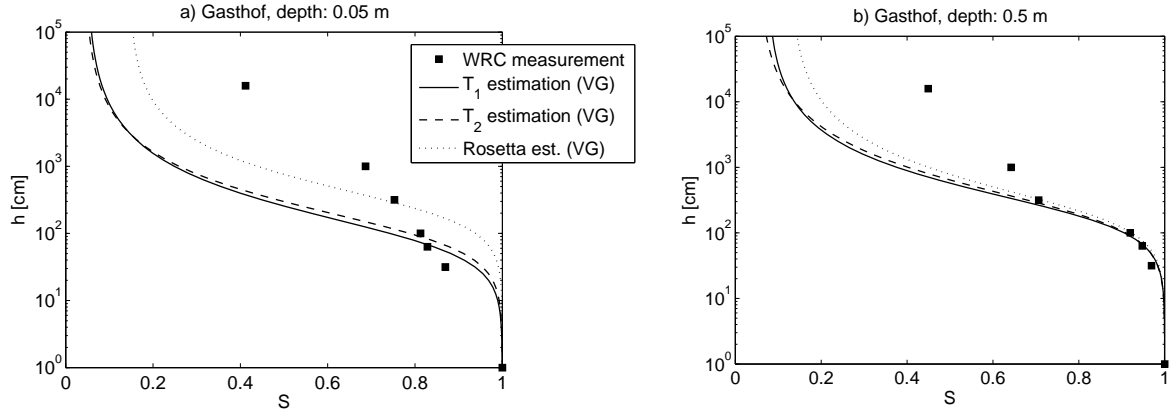


Figure 5.14: WRC predictions for the soil samples from the test site Gasthof, VG parameterization from T_1 distributions (solid lines) and T_2 distributions (dashed lines) compared to the real measurements with pressure plate experiments (black squares) and to the predictions with ROSETTA (model ROS-BD, dotted lines).

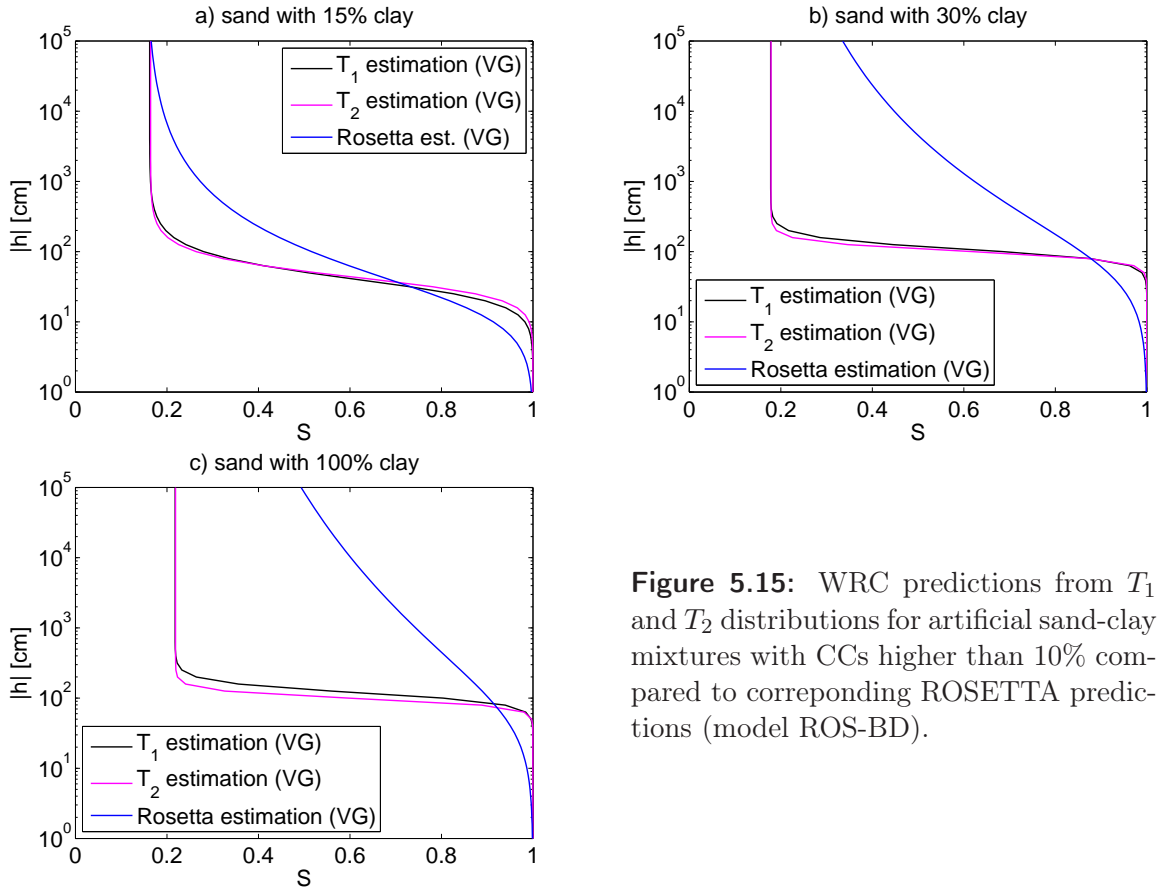


Figure 5.15: WRC predictions from T_1 and T_2 distributions for artificial sand-clay mixtures with CCs higher than 10% compared to corresponding ROSETTA predictions (model ROS-BD).

In Figure 5.14, the WRC estimations for the samples from the test site Gasthof and in Figure 5.15 examples of sand-clay mixtures with CCs higher than 10% are shown and compared to the corresponding ROSETTA predictions (with model ROS-BD). Similar figures can be found in the Appendix with further examples (Figure A.8 and A.9). Obviously, the WRC estimations by NMR for all these samples also fail as for the sample buch02 described above. The NMR based WRCs show a systematically overestimated slope of S as a function of $|h|$ in comparison to the slope predicted by ROSETTA. For increasing CCs, these systematic deviations increases more and more meaning that the NMR estimations of the WRC become more and more unplausible.

In Figure 5.16, the correlation of the VG parameter n estimated from NMR is compared with the predictions of n from ROSETTA (model ROS-BD) for all sand-clay mixtures. For the estimations from the T_1 and the T_2 distributions, the range for plausible n estimates starts at $n=2$. For smaller values, whereby the ROSETTA predictions are considered to be 'more' plausible, the NMR method overestimates n . The NMR-based n estimates increase with increasing CC up to absolutely unrealistic high values. For samples with such high clay contents, all references in the literature report n values smaller than 2. The reason for this overestimation was already presumed at the beginning of this chapter (see Chapter 5.1): The increasing PSD index n as estimated from NMR indicates a strong relation of this method to the pore bodies of the material, whereas the WRC is mainly sensitive to the pore throats.

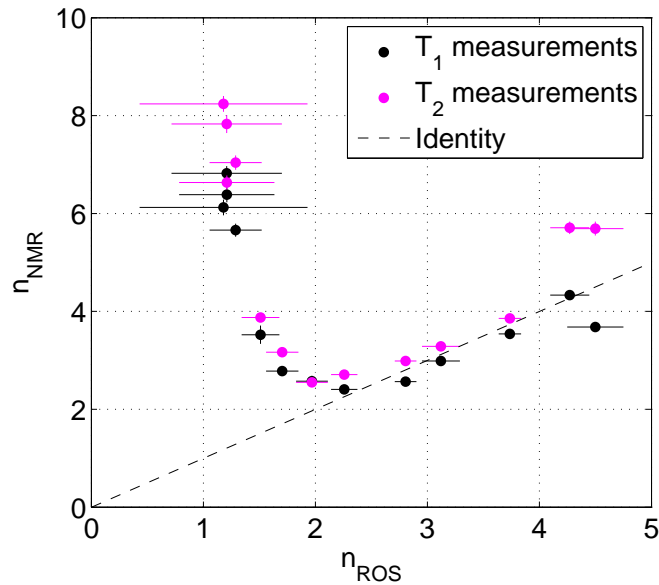


Figure 5.16: Comparison of the estimates of the PSD index n (VG model) from NMR (T_1 and T_2) and from ROSETTA (prediction model ROS-BD) for the sand-clay mixtures with clay contents (CC) from 0 to 100%.

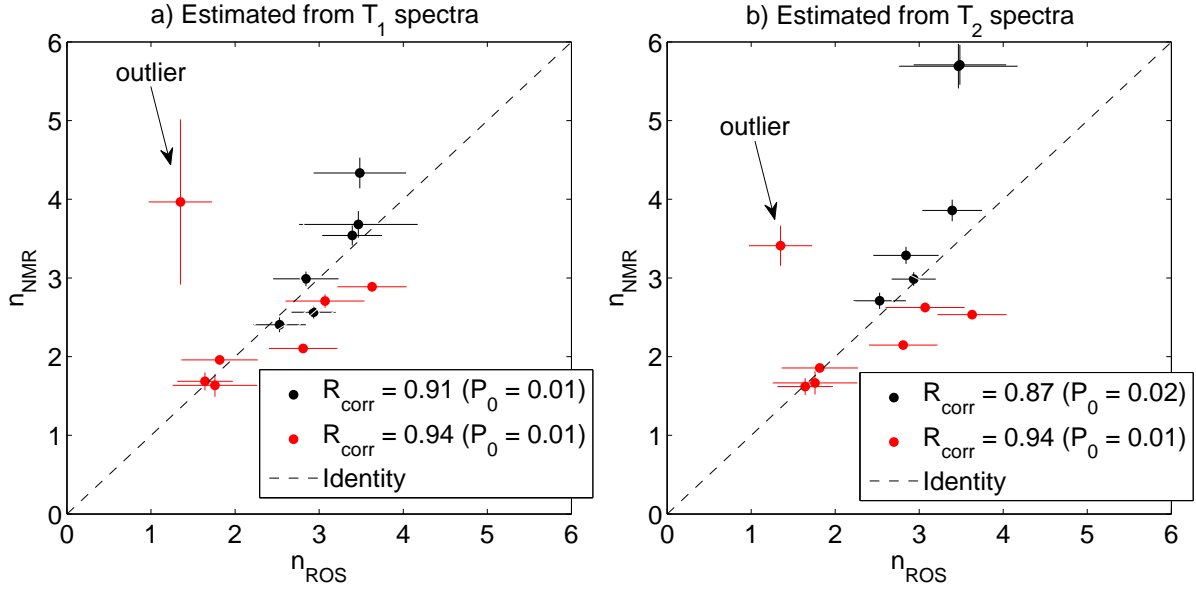


Figure 5.17: The estimates of the PSD index n (VG model) from T_1 (a) and from T_2 (b) distributions compared to the ROSETTA prediction (model ROS-TH33) for the natural (red symbols) and for the artificial samples (black symbols, sand-clay mixtures for CCs from 0 to 10%).

In Figure 5.17, the NMR-based estimates of n of both the natural and the artificial samples in the plausible range up to 10% CC are shown. On the left hand side, the results of the T_1 and on the right hand side the results of T_2 relaxation measurements are plotted against the ROSETTA prediction with model ROS-TH33. The correlation coefficients R_{corr} (as well as P_0 , the probability for the no-correlation hypothesis) for the data is given in the legend, whereby the outlier (sample buch02, see explanations above) was ignored for the calculation of R_{corr} . The correlation between both estimation methods is proved for the natural and for the artificial samples, respectively. The estimates from the T_2 distributions show a broader scattering compared to the T_1 results. Possibly, the influence of internal gradients leads to perturbations of the T_2 relaxation at the pore scale (see Equation 3.31 and corresponding explanations); that is, the T_2 relaxation distribution as estimation of the PSD is less accurate in comparison to the T_1 relaxation distribution.

5.4 Discussions and conclusions

In this chapter, the potential of NMR relaxometry (T_1 and T_2 relaxation) to estimate WCRs is investigated. An interpretation scheme was suggested that estimates the VG parameters from the cumulative NMR relaxation time distribution. This scheme is adapted from the usual method providing the PSD of sedimentary rocks such as sandstones and

limestones (see Chapter 3.2.2). Thereby, the cumulative NMR relaxation time distribution of a sample at saturation is calibrated by means of the residual water saturation S_R , which must be determined beforehand, and by shifting the distribution on the logarithmic scale such that it fits a certain fixed point. The resulting shifting factor can be considered to be the proportionality factor of $T_{1,2}$ and the reciprocal $|h|$. This factor includes specific material parameters such as the NMR surface relaxivity, as well as the surface tension, the contact angle, and the density of the pore water. These parameters are normally not at hand without great additional effort and thus, at least one water retention measurement for a sample to be investigated is suggested in addition to the NMR measurement at saturation. When both the fixed point and S_R are determined, the cumulative NMR relaxation time distribution can be calibrated, and the NMR-based WRC can be approximated, e.g., with the VG model. In this work, all fixed points were determined with the saturation degree of the material at a capillary pressure of $h=-63$ cm. The S_R values for the samples were determined here at a capillary pressure of $h=-2000$ cm. This kind of calibration, which is similar to the procedure using the mercury injection method for consolidated sediments, makes the approximation of the VG parameter α (see Figure 2.3 and corresponding explanations) pointless.

However, it could be shown with natural samples and with artificial sand-clay mixtures that the VG parameter n , which is the effective parameter for the prediction of K_{rel} (Equation 2.7), can reliably be estimated for material with a content of finer material (clay and silt) up to 10%. As expected beforehand, for loose sediments with higher contents of clay and silt the NMR-based WRC estimation fails. NMR is generally a method with high sensitivity to the pore bodies, whereas the hydraulic properties represented by the WRC are controlled by the distribution of the pore throats. In loose sediments a high content of clay or silt leads to a broad distribution of constrictions in the pore space that cannot be recovered by NMR relaxation measurements. In contrast, pore throats and pore bodies in sedimentary rocks have a specific ratio due to the consolidation processes, and the NMR measurement at saturation can be reliably provide a proxy also for the pore throat distribution. The findings of this study suggest that in loose sediments and soils this is not the general case. Particularly for soils with high contents of clay and silt, the NMR-based PSD measured at saturation is not necessarily a qualified measure for hydraulic processes at partial saturation.

In the next chapter, an approach is introduced that includes the NMR response at partial saturation into the discussion.

Chapter 6

Column experiments - K_{rel} estimation with earth's field NMR

The principle idea for the experiments documented in this chapter was to investigate the NMR properties at a kind of 'meso-scale' between conventional laboratory NMR and the field application of NMR, the magnetic resonance sounding method (MRS, see Chapter 3.3). On the one hand, the experimental setup for this study was performed with the focus on the comparison of conventional lab NMR at high magnetic field strength (HFNMR device: Maran Ultra at 2000 kHz, dead time: 150 μ s) and earth's field NMR (EFNMR device: Terranova at 2.1 kHz, dead time: 35 ms), whereby the EFNMR device is expected to provide measurement conditions similar to MRS. On the other hand, unusual large samples were used, that is, columns long enough to reconstruct 'natural' capillary fringes inside (Figure 6.1a). In this way, vertical water content distributions are realized very similar to those that are to be investigated *in situ* on the field scale. Similar column experiments were already successfully conducted by Ioannidis et al. (2006), who investigated glass beads (300 μ m) inside a glass tube of 1.25 m length with a diameter of 0.8 cm. They have shown that estimates of K_{rel} for these glass beads from the mean NMR relaxation times at different saturation degrees are possible. The experiments in the study at hand are a further step toward geological reality, because the sample material is sand of different grain sizes and the columns exhibit a much larger diameter. Finally, the investigations in this chapter will help to develop new interpretation approaches for MRS with focus on the vadose zone. The main content of this chapter is published by Costabel and Yaramanci (2011a).

6.1 Material and methods

6.1.1 Sample characterization and NMR data acquisition

Polycarbonate columns were filled with industrial sand of different grain sizes from fine to coarse sand. The porosities Θ_S of the samples specified in Table 6.1 vary from 0.38 to 0.42. The following abbreviations are used: fs for fine sand (grain size: 0.06 - 0.2 cm), msfs for medium and fine sand (grain size: 0.15 - 0.4 cm), ms for medium sand (grain size: 0.25 - 0.5 cm), cs1 for coarse sand 1 (grain size: 0.5 - 1.0 cm), and cs2 for coarse sand 2 (grain size: 1.0 - 2.0 cm). The cumulative grain size distributions of the samples are depicted in Appendix B (Figure B.1). Columns of different diameters were used: 3.6 cm diameter for the HFNMR measurements and 6.5 cm diameter for the EFNMR measurements. The heights of the columns vary between 1 and 1.6 m. The columns were saturated with distilled water through water-permeable filters mounted at their bottoms and afterward drained by gravity induced outflow in a water bath with a defined constant water table ($h=0$). The water table for every sample was individually determined to minimize the measurement effort. After reaching the equilibrium between gravity and capillary forces, the columns were sealed and NMR measurements were conducted by moving the columns stepwise through the NMR coils (Figure 6.1b). After the NMR experiments, the residual water content of each sample was determined by weighing. In doing so, the material from the upper part of each column was removed, i.e., from the range of the column where the NMR water content stably showed an asymptotic value representing the residual water. The corresponding saturation degree $S_{R,weight}$ for each sample is listed in Table 6.1.

Table 6.1: Properties of the industrial sand samples used for the column experiments: Grain size, porosity (Θ_S), and residual saturation degrees determined by weighing ($S_{R,weight}$) and by NMR in the HF and EF, respectively ($S_{R,HFNMR}$ and $S_{R,EFNMR}$).

Sample	Grain size [mm]	Θ_S	$S_{R,weight}$	$S_{R,HFNMR}$	$S_{R,EFNMR}$
fs	0.06 - 0.20	0.42±0.02	0.21±0.01	0.23±0.01	0.11±0.01
msfs	0.15 - 0.40	0.39±0.03	0.10±0.01	0.10±0.01	0.12±0.03
ms	0.25 - 0.50	0.39±0.01	0.09±0.00	0.09±0.02	0.05±0.03
cs1	0.50 - 1.00	0.38±0.01	0.11±0.00	0.10±0.01	0.05±0.03
cs2	1.00 - 2.00	0.38±0.05	0.12±0.01	0.11±0.01	0.10±0.02

With HFNMR, the T_2 relaxation was measured using the CPMG sequence, and with EFNMR, FID measurements (T_2^* relaxation) were performed (see Chapter 3.1.2 for details). To obtain reliable signal-to-noise (S/N) ratios with both methods, a stacking rate of 25 to 100 were conducted. The observed S/N ratios range from about 2 for the residual water at the upper parts of the columns and 15 for the saturated area at their bottoms.

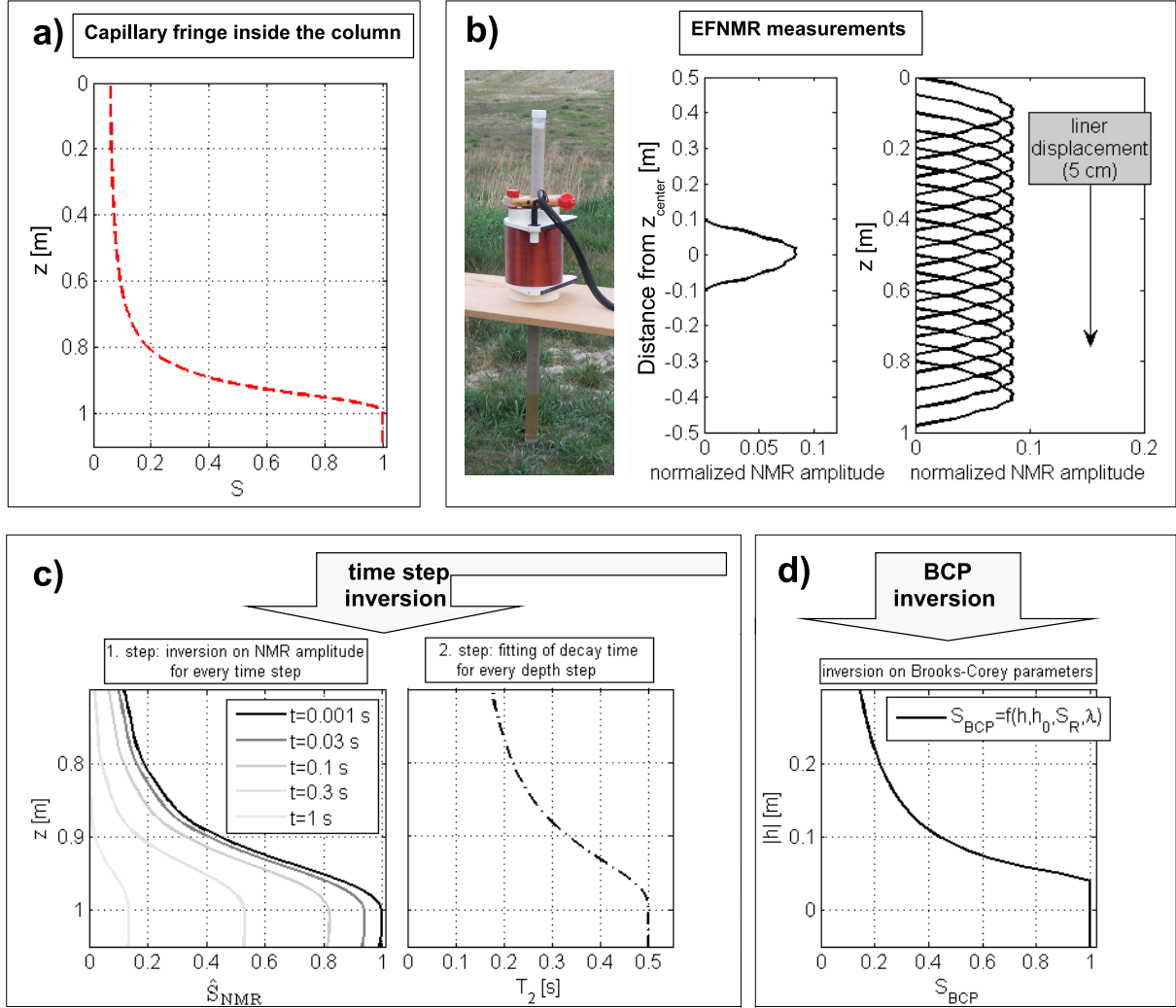


Figure 6.1: NMR measurement setup and interpretation schemes of the column experiments: (a) capillary fringe inside the column, (b, left hand side) EFNMR device, (b, middle) sensitivity distribution of the EFNMR coil, (b, right hand side) displacement of the sensitivity distribution by successive measurements along the column, (c) time step inversion - reconstruction of the spatial distributions of S_{NMR} and T_2 inside the column, (d) BCP inversion - approximation of the capillary fringe by the parameterization after Brooks and Corey (1964).

Usually, S/N ratios measured with MRS also lie within these limits. Thus, the EFNMR measurements can be considered to be representative for MRS measurement conditions. For the saturated range at the bottom of each sand column, as well as for the range with the residual water at the top several measurements at different heights are available. The standard deviations of the resulting NMR parameters at both extremal states represent the natural variability and are given as uncertainties in the Tables 6.1 and 6.3.

In contrast to the NMR investigations of Ioannidis et al. (2006), the sensitivity distribution of the NMR coils are taken into account in this study. The sensitivity distributions of the devices used in this work are quite large with approximately 20 cm for the EFNMR device (Figure 6.1b) and 6 cm for the HFNMR device. Regarding the material that was used, capillary fringes with a height smaller than 20 cm, e.g. for coarse sand, must be expected. To obtain a reliable resolution of the vertical water content distribution inside the columns, one needs therefore NMR measurements with a vertical increment much smaller than the sensitivity distribution of the coil. Afterward, an adequate inversion scheme has to be applied to correct the inaccuracy that is caused by the broadness of the coil sensitivity distribution.

To recover the sensitivity distribution inside the devices, a cylindrical sample with a height of 1 cm and filled with pure water was used. The amplitude of its NMR signal as function of the position inside the coil was measured by moving it through the device with a step size increment of 1 cm. Figure 6.1b shows the sensitivity distribution of the EFNMR device. The curve in Figure 6.1b (middle) is normalized such that the area under the curve equals 1. As expected, the sensitivity has its maximum at the center of the coil, however, the range that is energized during the NMR experiment consists of about 20 cm. Because the column is moved stepwise through the device with a small increment, the sensitivity distribution of the NMR coil is displaced at the column such that the sensitivities of successive measurements overlap each other. This is depicted in Figure 6.1b (right hand side). For clarity, the sensitivity distributions in this plot are depicted with an increment of 5 cm. The resolution that can finally be realized using an adequate inversion approximately matches the increment of the column displacement. Thus, for the real experiments in this study smaller increments were chosen: 1 cm for the samples cs1, cs2 and ms, 2 cm for msfs and fs.

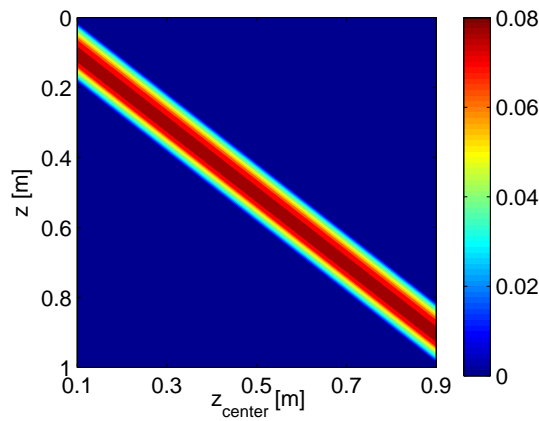


Figure 6.2: Surface plot of the forward operator $\Gamma(z, z_{center})$ for an ensemble of EFNMR measurements with a spatial increment of 1 cm.

The coil center position z_{center} is given as the reference point for a single measurement. Organizing the sensitivity distributions for an ensemble of measurements with respect to z_{center} , one may understand the resulting matrix (Figure 6.2) as the forward operator $\Gamma(z, z_{center})$ for the apparent NMR saturation S_{app} as a function of z_{center} :

$$S_{app}(z_{center}) = \frac{E_0(z_{center})}{E_S} = \int_{z_{lb}}^{z_{ub}} \Gamma(z, z_{center}) S_{NMR}(z) dz. \quad (6.1)$$

The apparent (i.e., measured) saturation degree S_{app} is determined by dividing the NMR signal amplitude E_0 with the mean amplitude from the saturated area E_S below the water table. Both S_{app} and E_0 are allocated at the center position z_{center} of the NMR coil. However, for each single measurement the energized area ranges from z_{lb} to z_{ub} that are the lower and the upper bounds of the coil sensitivity distribution. $S_{NMR}(z)$ is the real vertical NMR saturation distribution inside the column.

6.1.2 Time step inversion

To include also the NMR relaxation times into the discussion, one has to enhance the forward problem in Equation 6.1 with respect to the time dependence:

$$E_{rel}(t, z_{center}) = \frac{E_0(t, z_{center})}{E_S(t=0)} = \int_{z_{lb}}^{z_{ub}} \int_{T_2^{(*)}} \Gamma(z, z_{center}) S_{NMR}(z, T_2^{(*)}) \exp \left[-\frac{t}{T_2^{(*)}(z)} \right] dT_2^{(*)} dz \quad (6.2)$$

Equation 6.2 is inverted by subdividing it into two individual problems to get the vertical distribution of both $S_{NMR}(z)$ and $T_2^{(*)}(z)$ (i.e., T_2 for the HFNMR measurements and T_2^* for the EFNMR measurements):

$$S_{app}(t_n, z_{center}) = \int_{z_{lb}}^{z_{ub}} \Gamma(z, z_{center}) \hat{S}_{NMR}(t_n, z) dz \quad (6.3)$$

$$\hat{S}_{NMR}(t, z_m) = \int_{T_2^{(*)}} S_{NMR}(z_m, T_2^{(*)}) \exp \left[-\frac{t}{T_2^{(*)}(z_m)} \right] dT_2^{(*)} \quad (6.4)$$

As first step Equation 6.3 is inverted for every t_n with n denoting the index of the time sample of the NMR measurement (i.e., the time step). In Figure 6.1c (left hand side), the resulting distributions of the quantity \hat{S}_{NMR} for some example time steps are depicted. The vertical distribution of $S_{NMR}(z)$ is given with $\hat{S}_{NMR}(z, t=0)$. As second

step the $\hat{S}_{NMR}(t_n)$ curves are fitted on the time scale for every z_m with m denoting the index of the z vector. As result, one gets the vertical distribution of $T_2^{(*)}(z)$, which is shown exemplarily in Figure 6.1c (right hand side). This procedure is similar to the so called time step inversion as introduced by Mohnke and Yaramanci (2005) for the MRS method. The \hat{S}_{NMR} curves are fitted multi-exponentially with a smoothed inverse Laplace transform (Chapter 3.2.3). I calculate and discuss here solely the logarithmic mean values of the resulting relaxation time spectra. These spectra in the literature are often called relaxation time distributions. However, I use the term 'distribution' here for the vertical spatial distribution of the log mean values of the relaxation time spectra to avoid misunderstandings.

6.1.3 Brooks-Corey parameterization of the capillary fringe

In addition to the time step inversion as described above, a further inversion scheme is applied to the NMR data that directly provide the hydraulic parameters characterizing the capillary fringe by means of the BC model (Equation 2.5). As for the time step inversion, the amplitudes of the measurement at each vertical location along the column are normalized with respect to the mean amplitude value from the saturated area at the bottom of the column to get the apparent saturation degree S_{app} . Afterward, the BC parameters are fitted to S_{app} . In doing so, the forward calculation in Equation 6.1 is reformulated accounting for the BC parameterization (BCP) of the saturation degree as a function of h :

$$S_{app}(z_{center}) = \int_{z_{lb}}^{z_{ub}} \Gamma(z, z_{center}) S_{BCP}(z) dz \quad (6.5)$$

$$S_{BCP}(z) = \begin{cases} S_R + (1 - S_R) \left(\frac{h_0}{h} \right)^\lambda, & z < z_{table} \text{ with } h = z - z_{table} \\ 1 & , z \geq z_{table} \end{cases}$$

During the inversion of Equation 6.5, only three fitting parameters (S_R , λ , and h_0) are varied until the approximation of $S_{app}(z)$ is achieved within an optional accuracy. The nonlinear least square solver of the MATLAB[®] optimization toolbox (MathWorks, 2007) is used to invert Equation 6.5, as well as Equations 6.3 and 6.4.

6.1.4 Hydraulic parameters from drainage experiments

In addition to the NMR experiments and with the focus to assess the NMR results, the cumulative outflow during drainage of each sample was measured. For these drainage experiments the columns with 3.6 cm diameter (height of the saturated sand column:

1m) were used. The cumulative outflow was measured for several hours until the water content in the columns reaches a state of equilibrium. Figure 6.3 shows this data with symbols. Afterward, the cumulative outflow from the columns was modeled with HYDRUS-1D, a free software that provides one-dimensional unsaturated flow simulations (Šimůnek and van Genuchten, 1999; Šimůnek et al., 2009). The modeling is realized by solving the one-dimensional Richard's equation (Equation 2.1) using the finite element method (Šimůnek et al., 2009). Additionally to the finite element modeling, HYDRUS-1D also allows for estimating hydraulic parameters including $K_U(\Theta)$ and K_S by approximating cumulative outflow data. The outflow simulations initially start at Θ_S . During the modelings, the residual water content was fixed and set to be equal to the real values $S_{R,weight}$ as found by weighing the material after the drainage experiment. At the top of the soil column, atmospheric boundary conditions were simulated. At the bottom, the boundary condition was set to simulate free drainage (Šimůnek et al., 2009).

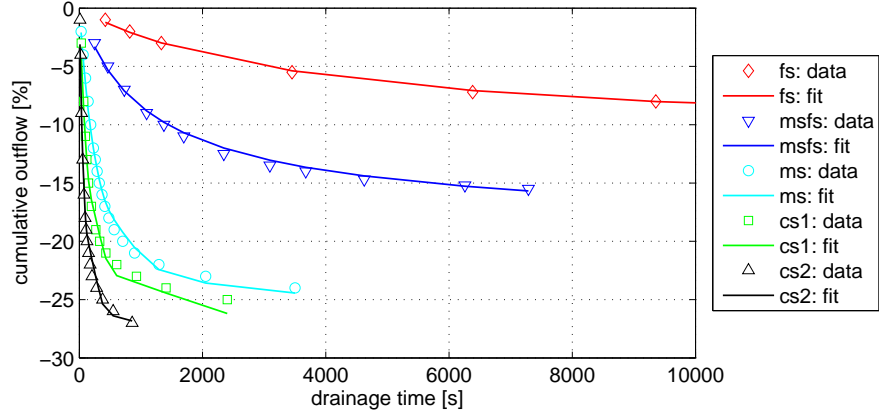


Figure 6.3: Measured cumulate outflow with time during the drainage of the columns (symbols), approximation of the outflow data according to the van Genuchten-Mualem model (solid lines) with HYDRUS-1D.

Table 6.2: Hydraulic parameters (after van Genuchten (1980) and Mualem (1976)) of the sand samples estimated with HYDRUS-1D from the cumulative outflow of the sand columns.

Sample	K_S [m/d]	n	α [cm ⁻¹]	$m(=1 - 1/n)$
fs	3.1±0.5	2.82±1.39	0.02±0.01	0.65±0.32
msfs	15.0±1.0	3.60±0.60	0.02±0.00	0.72±0.12
ms	69.4±5.5	6.11±1.02	0.04±0.00	0.84±0.14
cs1	131.2±25.8	6.44±1.04	0.17±0.01	0.84±0.14
cs2	251.3±53.2	6.60±1.61	0.18±0.01	0.85±0.21

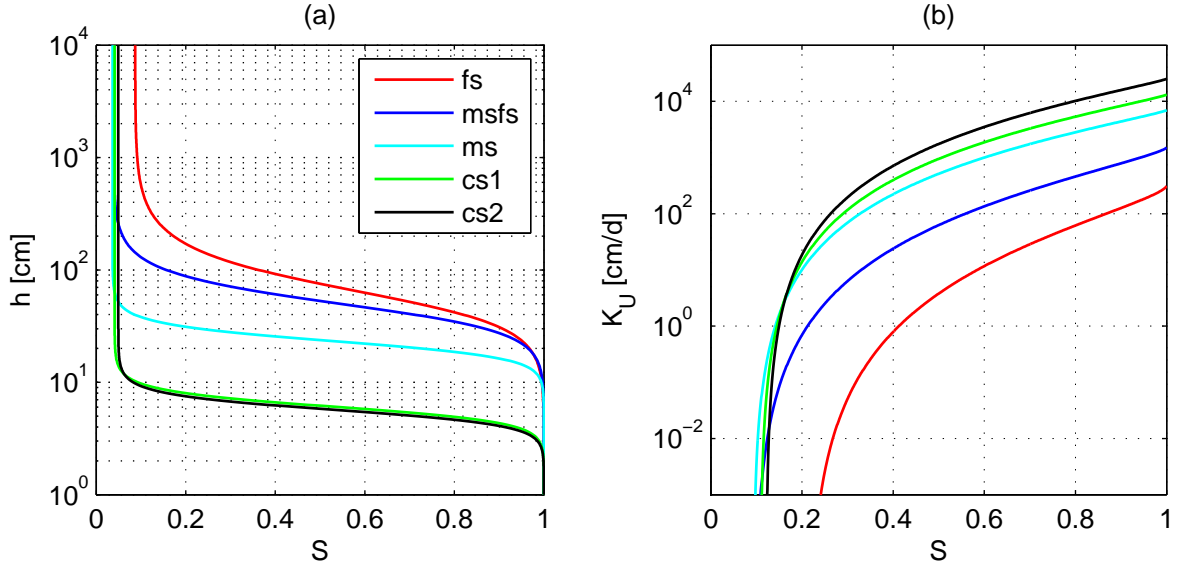


Figure 6.4: Water retention curves (a) and K_U as a function of S for the sand samples found by HYDRUS-1D approximation of the cumulative outflow data in Figure 6.3.

The approximation of the outflow data with HYDRUS-1D (solid lines in Figure 6.3) provides estimates of the VG and VGM parameters according to Equations 2.4 and 2.7. In Figure 6.4, the resulting WRCs and the $K_U(S)$ functions estimated from HYDRUS-1D are depicted. The fitted parameters can be found in Table 6.2. In principle, HYDRUS-1D also allows the application of the BC model. However, with the data base at hand the BC parameterization with HYDRUS-1D could not be applied due to strong instability and loss of robustness during the hydraulic modeling and parameter approximation. Because the NMR and the HYDRUS-1D estimates are based on different models, I abstain from a direct comparison of the fitted hydraulic parameters for both estimation methods. Instead, the K_{rel} predictions in dependency on S_E are finally compared. Thus, the $K_U(S)$ estimation from HYDRUS-1D (by means of the VGM model) is normalized with respect to K_S for the comparison later on.

6.2 Results and interpretation

6.2.1 Estimation of the residual water content with NMR

Figure 6.5 compares both the HFNMR and the EFNMR results for S_R with those that are found by weighing the material removed from the upper part of the columns (see also

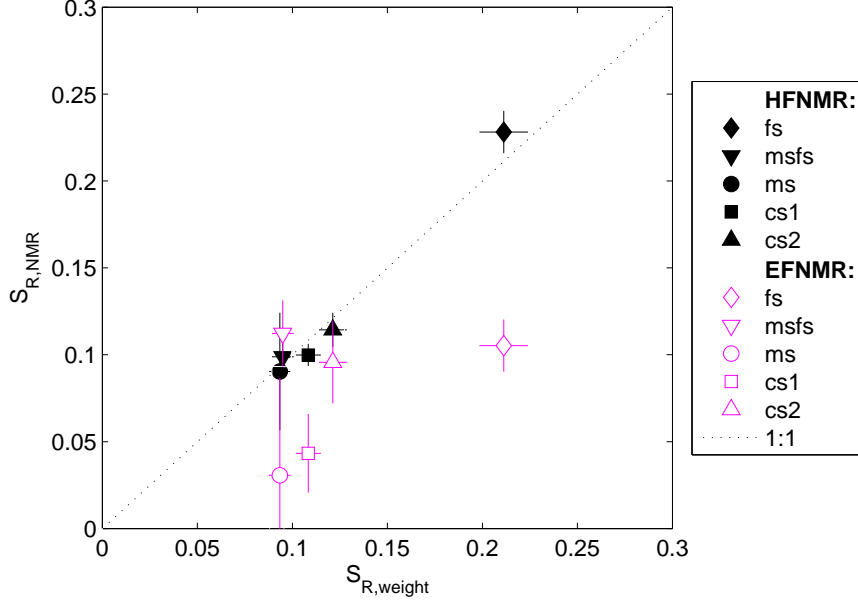


Figure 6.5: Residual saturation degree S_R measured by NMR compared to the real values as determined by weighing.

Table 6.1). Obviously, $S_{R,HFNMR}$ is well correlated with $S_{R,weight}$ and also the $S_{R,EFNMR}$ values of the samples msfs and cs2 almost match the real values within the 95% uncertainty intervals. The discrepancy between the HFNMR results and the real values for S_R is not only due to the uncertainties of the measurements. It is more likely that the NMR method exhibits minor systematic errors due to unavoidable inaccuracies during internal device calibrations, which might cause imperfect flip angles and/or off-resonance excitation. However, compared to the laboratory study demonstrated and discussed in Chapter 5.3 (Figure 5.11), the accuracy of the $S_{R,HFNMR}$ estimates is in a similar order of magnitude. In contrast, the $S_{R,EFNMR}$ values of the samples fs, ms and cs1 are clearly underestimated. This effect occurs when the decrease of T_2^* caused by decreasing saturation (see Equation 4.39) reaches the dead time of the measurement. It is expected that the relaxation regimes inside the pore space with relaxation times significantly smaller than the measurement dead time are non-visible in the NMR signal (Boucher et al., 2011). In this study, this is the case for all samples with $T_{2,S}^*$ times smaller than 0.2 s. Generally, an increasing misfit of $S_{R,EFNMR}$ and $S_{R,weight}$ with increasing ratio t_{dead}/T_2^* and, of course, with lower S/N ratios is expected.

6.2.2 Test of the inversion schemes with synthetic data

The inversion schemes introduced above are tested with a synthetic data example. The S_{NMR} model was calculated following the VG model (Equation 2.4) using typical sand

parameters (suggested parameters by HYDRUS-1D: $n=2.7$, $\alpha=0.15 \text{ cm}^{-1}$, $S_R=0.05$). The T_2 distribution was calculated from S_{NMR} using Equation 4.39 with $T_{2,S} = 0.5 \text{ s}$ and $\lambda=2$, which is a typical BC pore-size-distribution index for homogeneous sand. Several time steps resulting from the time step inversion are depicted in Figure 6.6a. In Figure 6.6b and 6.6c, the S_{NMR} and T_2 distributions of the model are shown. The forward calculation was realized by using the forward operator shown in Figure 6.2, i.e., a measurement of the EFNMR device was simulated. The cyan dashed-dotted line in Figure 6.6b represents the simulated NMR amplitudes normalized to values between 0 and 1, understood as the apparent saturation degree S_{app} . In Figure 6.6c, the apparent relaxation time $T_{2,app}$, i.e., the logarithmic mean values of the fitted T_2 time spectra are shown. Obviously, there is a significant difference between the real model and the simulated measurement curves. Thus, a general application of an inversion calculation for the measurement setup in this study is expedient, otherwise propagating errors in the following estimations must be expected. The discrepancy of the real and apparent distributions of both S_{NMR} and T_2 is expected to decrease with increasing height of the capillary fringe. The black solid lines in Figure 6.6b and 6.6c represent the inverted S_{NMR} and T_2 curves, i.e., S_{inv} and $T_{2,inv}$. They are in agreement with the model, whereas a slight discrepancy appears for S_{NMR} close to 1. Also, slight discrepancies in the T_2 data for S_{NMR} values smaller than 0.2 are observed, which is due to the instability of the inverse Laplace transform for NMR signals with decreasing amplitudes.

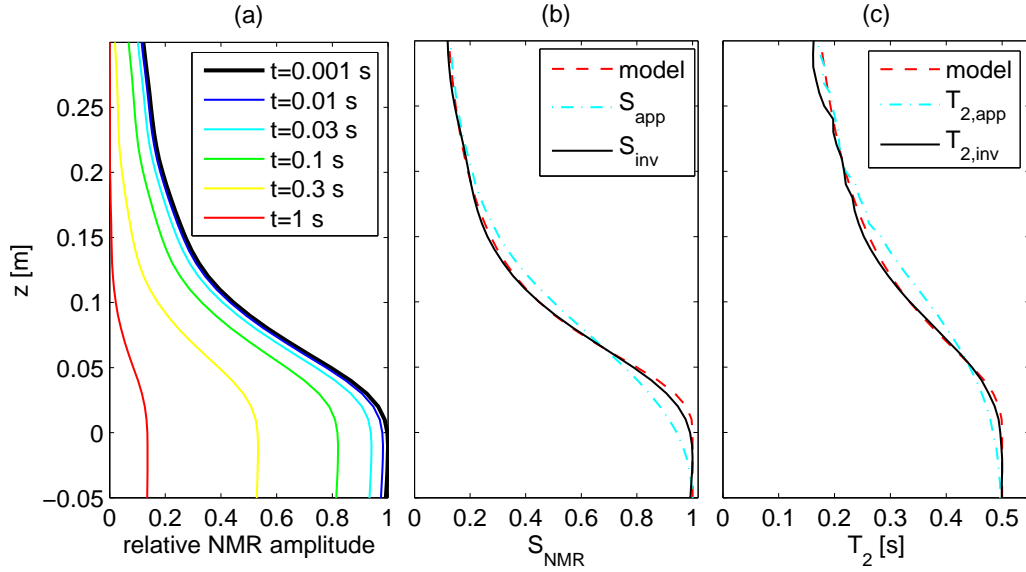


Figure 6.6: Test of the time step inversion scheme with a numerical example: (a) Inversion results for different measurement time steps. (b) Vertical S_{NMR} distribution of the initial model, simulated measurement S_{app} and inversion result S_{inv} . (c) Vertical T_2 distribution of the initial model, simulated measurement $T_{2,app}$ and inversion result $T_{2,inv}$, which is fitted as a second inversion step (see explanation in the text).

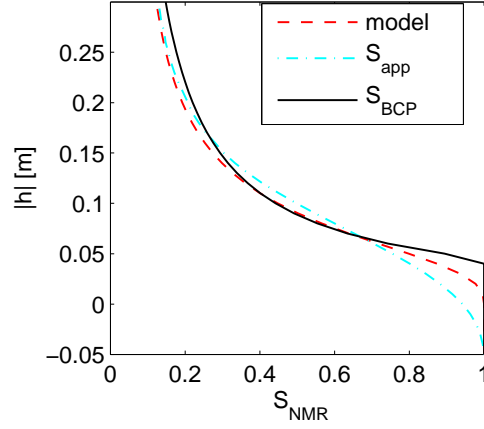


Figure 6.7: Test of the BCP inversion scheme with a numerical example: Initial model defined by hydraulic parameterization after van Genuchten (1980), simulated measurement S_{app} and inversion result S_{BCP} , i.e., the data approximation by means of the hydraulic parameterization after Brooks and Corey (1964).

In Figure 6.7, again both the S_{NMR} distribution and the simulated S_{app} of the synthetic example are plotted and compared to the result of the BCP inversion. The depicted inversion result is calculated from the approximated values for $S_{R,NMR}$, λ and h_0 . The general curvatures of both the model and the inversion result are in agreement, whereas the BCP inversion shows slight overestimations of S_R and h_0 . The overestimation of h_0 leads to overestimations of larger S_{NMR} near 1. Please note that the initial model was generated by the VG model, which allows, in the most cases, a more realistic representation of water retention data, especially close to $S=1$. However, the approximation with the BC model is the better choice for the measurements of this study, as explained below.

6.2.3 Dependency of T_2 and T_2^* from the saturation degree

Figure 6.8 shows the NMR measurements (S_{app} , $T_{2,app}$ and $T_{2,app}^*$) and the inversion results (S_{inv} , $T_{2,inv}$ and $T_{2,inv}^*$) exemplarily for the coarse sand sample cs1. The water table is located at $z=-0.4$ m. Similar figures are shown in Appendix B for the other samples (Figures B.2 to B.5). The spatial distributions of S_{NMR} are depicted in Figure 6.8a (HFNMR) and Figure 6.8c (EFNMR). Both plots show a well developed capillary fringe with S_{NMR} close to 1 near the water table and the expected convergence to a non-zero S_R at the upper part of the column. For the EFNMR measurements, the difference between S_{app} and S_{inv} is in the range of about 5% and is maximal at the region of the highest curvature of $S_{app}(z)$. The HFNMR measurements show a difference of about 2% between S_{app} and S_{inv} . The smaller discrepancies of the HFNMR measurements are due to the smaller sensitivity distribution of the HFNMR coil with only 6 cm broadness in contrast

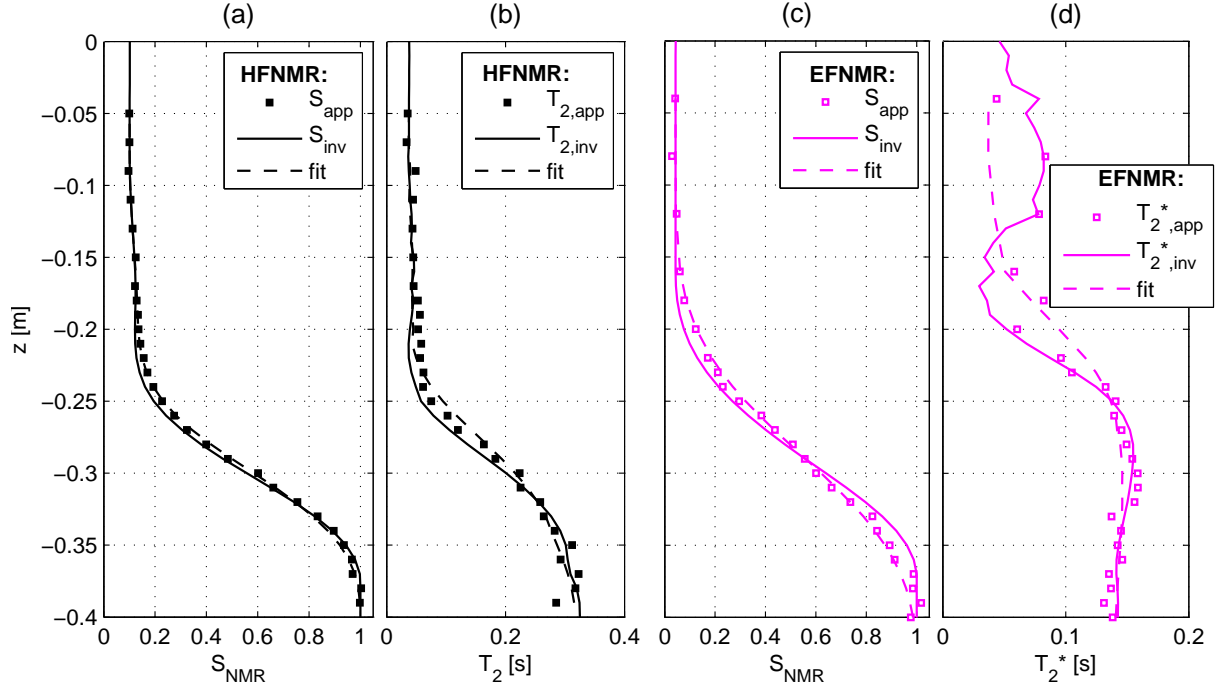


Figure 6.8: Measured (S_{app} , $T_{2,app}$, and $T_{2,app}^*$) and inverted NMR results (S_{inv} , $T_{2,inv}$, and $T_{2,inv}^*$) for the coarse sand sample cs1, spatial distributions inside the column: HFNMR saturation degree (a) and T_2 times (b), EFNMR saturation degree (c) and T_2^* times (d).

to 20 cm of the EFNMR coil. The vertical relaxation time distributions are depicted in Figure 6.8b (HFNMR: T_2) and in Figure 6.8d (EFNMR: T_2^*). Please note the different ranges of the x-axes in these plots. The EF $T_{2,S}^*$ time at saturation (0.14 s) is clearly shorter than the HF $T_{2,S}$ time of 0.30 s due to a non-negligible dephasing of the EFNMR signal caused by internal field gradients (see Chapter 3.1.2 for a detailed discussion of this effect). Also the shapes of the relaxation time curves are different. The HF T_2 curve shows a trend very similar to the S_{NMR} curve, while the EF T_2^* values are quite constant up to a column depth of about -0.25 m corresponding to S_{NMR} values of about 0.3. The expected decrease of T_2^* with decreasing saturation (Equation 4.39) can be observed only for $S_{NMR} < 0.3$, whereas the T_2^* times at small saturation degrees become quite inaccurate due to smaller S/N ratios with decreasing S_{NMR} . Similar observations are made for the other samples in this study (Figures B.2 to B.5). Obviously, the dependence of T_2^* on the saturation degree is much more complex (as expected with Equation 4.41), and will be discussed later in detail.

Figure 6.9 shows the S_{app} measurements of all samples and their corresponding inversion results S_{inv} , respectively. Originally, every column was prepared with the water table at an individual depth for optimizing the measurement effort. For a better comparison of the results, the column depth z on the y-axis in Figure 6.9 is corrected such that the water

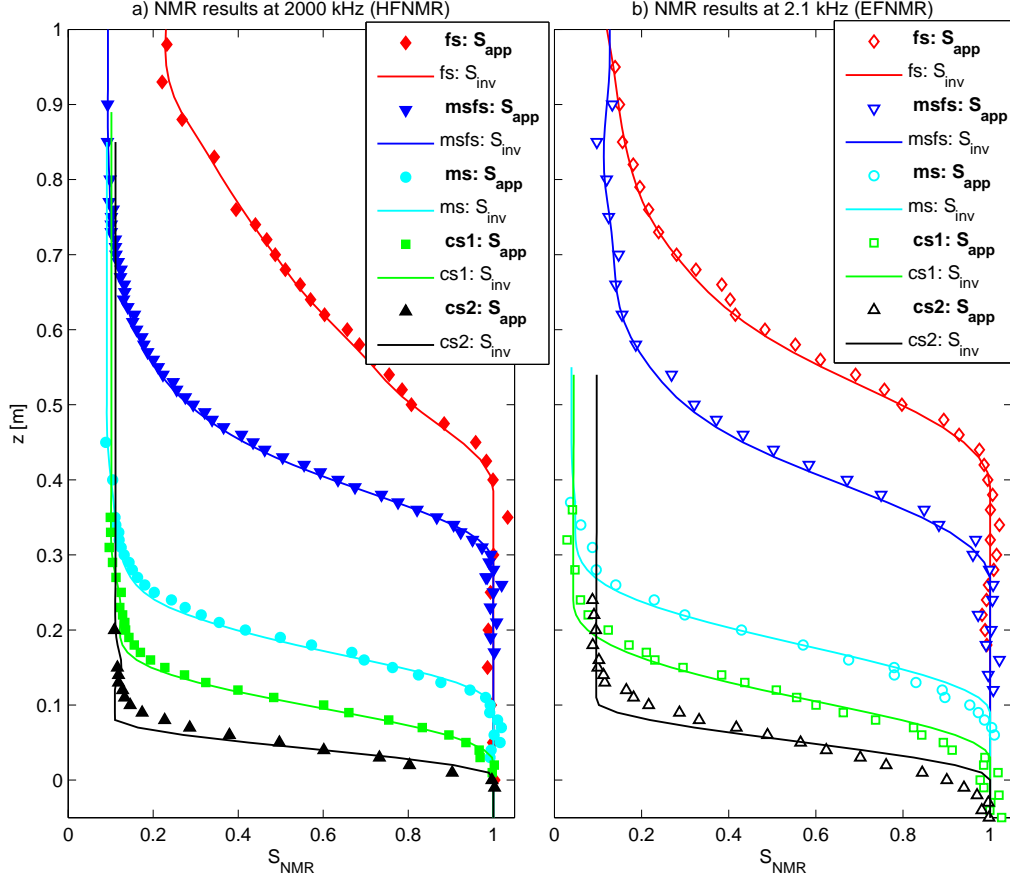


Figure 6.9: Measurements of the apparent NMR water saturation degree (S_{app}) inside the columns by HFNMR (a) and EFNMR (b) compared to the approximations with the time step inversion.

table is located at $z=0$ for all samples. Consequently, the y-axis might be interpreted as the absolute value of the capillary pressure height $|h|$ (see Chapter 2.2). The HF and the EFNMR curves show quite similar shapes representing the capillary fringe inside the columns. The height of the capillary fringe is related to the individual grain size of each sand sample (see also Figure B.1). For the sand samples with smaller grain sizes (fs and msfs), the S_{inv} curve do not significantly differ from S_{app} . Obviously, a data inversion is not necessarily needed for samples with large capillary fringes. As discussed above, the S_R values of the EFNMR measurements for the samples fs, ms, and cs1 are clearly smaller compared to S_R measured by HFNMR.

Now, the saturation dependency of the NMR relaxation times will be investigated. In Figure 6.10, the observed relaxation times for both the HF and EF measurements are plotted against S_{NMR} . Both the measured and the inverted quantities are shown. All HF T_2 times can reliably be fitted with Equation 4.39 and the values for λ lie within a reliable

range for the BC pore-size-distribution index (see Chapter 2.2). The corresponding values of the fitting parameter λ can be found in Table 6.3. The estimates of λ are significantly larger than 1 for all samples, which corresponds to the expectation for homogeneous sand (see also Chapter 5.2.2 and Figure 5.3). However, T_2^* as a function of S_{NMR} clearly differs from the expected relationship. A plausible approximation using the BC model (Equation 4.39) is not possible for all samples. One observes a slight increase of T_2^* with decreasing S_{NMR} down to values between 0.3 and 0.6. The expected decrease of T_2^* can be found for smaller S_{NMR} values. I assume the dephasing effect to be responsible for this feature. As described in Chapter 3.1.2 and in 3.2.2, the dephasing of the NMR signal in an FID experiment leads to a difference between T_2 and T_2^* (see Equation 3.30) due to magnetic field gradients in the primary magnetic field. Obviously, this is the case for all samples in this study. I assume that the dephasing effect decreases with decreasing water content in the pore space, which leads to converging T_2 and T_2^* values for decreasing saturation degrees. To find an algebraic formulation for the T_2^* as a function of S , a saturation-dependend weighting factor of the dephasing relaxation rate in Equation 3.30 is introduced here. This weighting factor is defined as a power law of the saturation degree with the exponent ν that might be referred to as the dephasing index. For T_2^* at partial saturation ($T_{2,U}^*$), the expectation formulated in Equation 4.41 is then modified to:

$$\frac{1}{T_{2,U}^*} = \frac{1}{S_{NMR}^{1/\lambda} T_{2,S}} + \frac{S_{NMR}^\nu}{T_{2,deph}} \quad (6.6)$$

In this equation the new parameter ν appears to be an additional empirical parameter. The T_2^* data shown in Figure 6.10 is approximated using Equation 6.6 with fixed $T_{2,S}$, $T_{2,S}^*$, and λ as estimated from the HFNMR data. The results for ν vary within the range of about 0.9 to 1.8 (see Table 6.3). Obviously, Equation 6.6 explains the observed EFNMR data adequately.

Table 6.3: Parameters estimated from the NMR measurements: Transverse NMR relaxation times at saturation (HFNMR and EFNMR), the pore-size-distribution index λ estimated with Equation 4.39 (HFNMR), and the dephasing index ν estimated with Equation 6.6 (EFNMR).

Sample	HF $T_{2,S}$ [s]	EF $T_{2,S}$ [s]	EF $T_{2,S}^*$ [s]	λ (HF T_2)	ν (EF T_2^*)
fs	0.74±0.06	0.31±0.02	0.15±0.00	1.59±0.16	1.43±0.33
msfs	0.61±0.03	0.55±0.05	0.21±0.01	1.42±0.15	0.90±0.24
ms	0.20±0.01	0.31±0.04	0.09±0.00	1.33±0.08	0.89±0.22
cs1	0.30±0.05	0.46±0.05	0.14±0.01	1.12±0.07	1.07±0.36
cs2	1.10±0.07	1.17±0.1	0.28±0.02	1.17±0.08	1.78±0.20

6.2. Results and interpretation

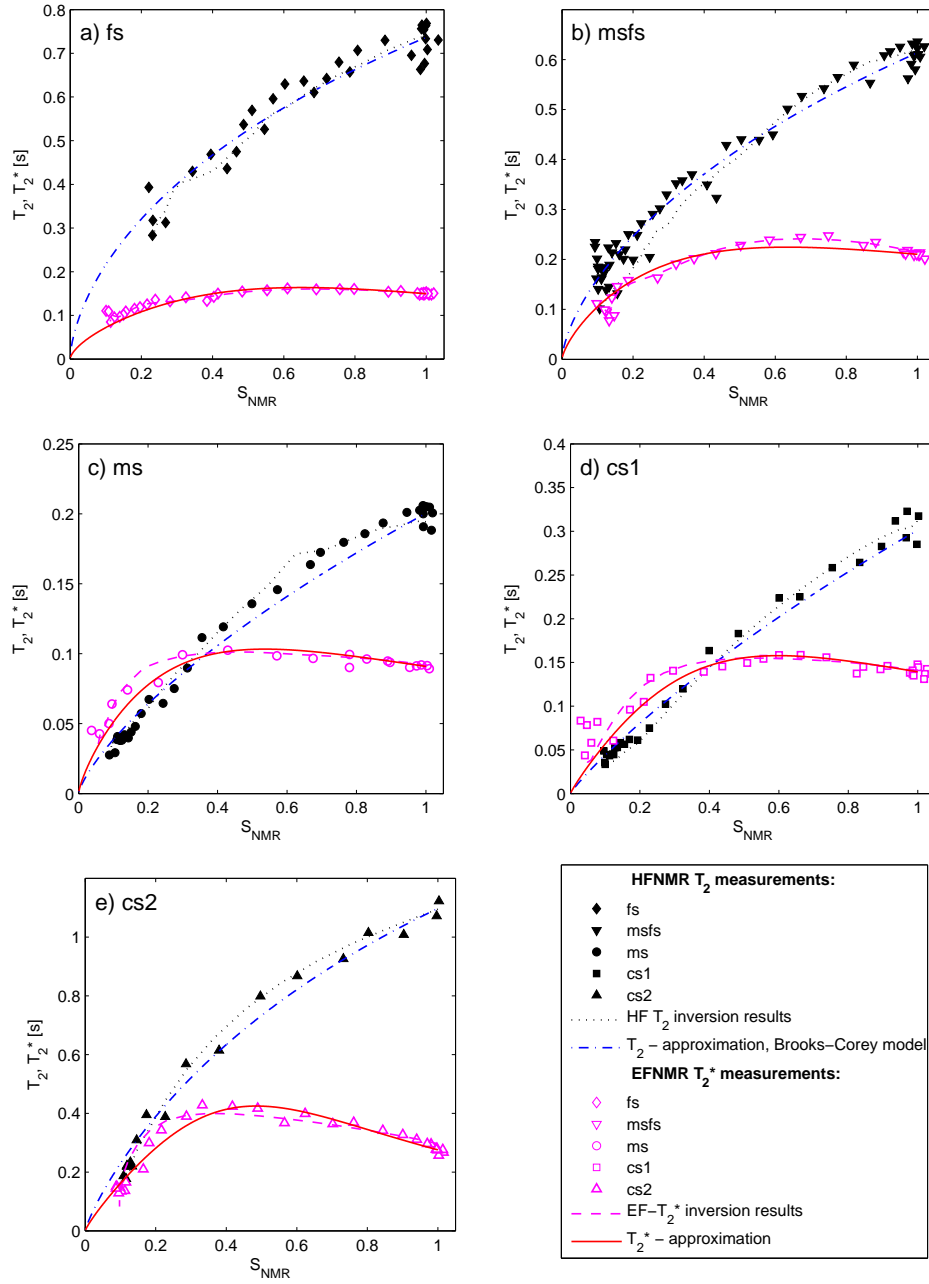


Figure 6.10: Dependency of the transverse relaxation times (HFNMR: T_2 , EFNMR: T_2^*) from the saturation degree S_{NMR} , the measurement results (i.e. apparent values) are plotted with symbols (closed black symbols - HFNMR, open magenta symbols - EFNMR), the inverted results are plotted with lines (dotted blue lines - HFNMR, dashed magenta lines - EFNMR), the approximation of the relaxation times as functions of S_{NMR} are plotted with lines (dashed-dotted blue lines - HFNMR, solid red lines - EFNMR). The T_2 times are approximated according to the Brooks-Corey model (Equation 4.39), the T_2^* times are approximated assuming a saturation dependency of the dephasing relaxation rate (Equation 6.6).

6.2.4 Prediction of K_U from T_2 and T_2^* at partial saturation

Using Equation 6.6 and assuming S_{NMR} to be similar to S_E , the term $S_E^{1/\lambda}$ in Equation 2.8 can be substituted to find a modification of Equation 4.40, i.e., a formulation that allows the estimation of K_{rel} from $T_{2,U}^*$ data:

$$K_{rel} = \frac{K_U}{K_S} = S_{NMR}^a \left(\frac{T_{2,S}}{T_{2,U}^*} - \frac{T_{2,S} S_{NMR}^\nu}{T_{2,deph}} \right)^{-2} \quad (6.7)$$

Compared to the K_{rel} estimation by T_2 , the estimation of K_{rel} from T_2^* measurements necessitates additional *a priori* information: $T_{2,S}^*$ ($= T_{2,S} + T_{2,deph}$), $T_{2,S}$, and ν . In practice, these parameters must be found by calibration or must be taken from a database, once available. In Figure 6.11, the predictions of K_{rel} from the NMR measurements are compared to the estimations found by HYDRUS-1D by modeling the drainage experiments. K_{rel} is plotted as a function of the effective saturation S_E , which is calculated by Equation 4.1 for the NMR measurements. The gray areas denote the confidence intervals of K_{rel} calculated from the uncertainty intervals of the VGM parameter m (see Table 6.2). The NMR predictions are calculated with Equation 4.40 for the HF T_2 data and with Equation 6.7 for the EF T_2^* data. The BC parameter a was set to 3 for the samples fs and msfs, and to 2 for the samples ms, cs1, and cs2. Both the HF and the EFNMR based K_{rel} predictions match the real K_{rel} curves within the confidence intervals. The difference of both estimations for all samples lies within half a decade and the underestimated $S_{R,EFNMR}$ values for the samples fs, ms, and cs1 that are discussed above do not cause significant systematic discrepancies when estimating K_{rel} . However, in this study only sand samples with quite small S_R values are investigated. Systematic errors must be expected when estimating K_{rel} using EFNMR for material with significant contents of silt and clay, which causes an increase of S_R .

6.2.5 Prediction of K_U from capillary fringe parameterization

As already depicted in Figure 6.9, Figure 6.12 shows again the NMR signal amplitudes normalized to values between 0 and 1 corresponding to the apparent saturation degree S_{app} for both the HF (a) and EF (b) measurements with symbols. The solid lines represent the approximations of the S_{app} curves discovered by the Brooks-Corey parameterization (BCP) inversion scheme, i.e., inversion of Equations 6.5. The y-axis depicts the height above the water table and is therefore interpreted as the capillary pressure height $|h|$.

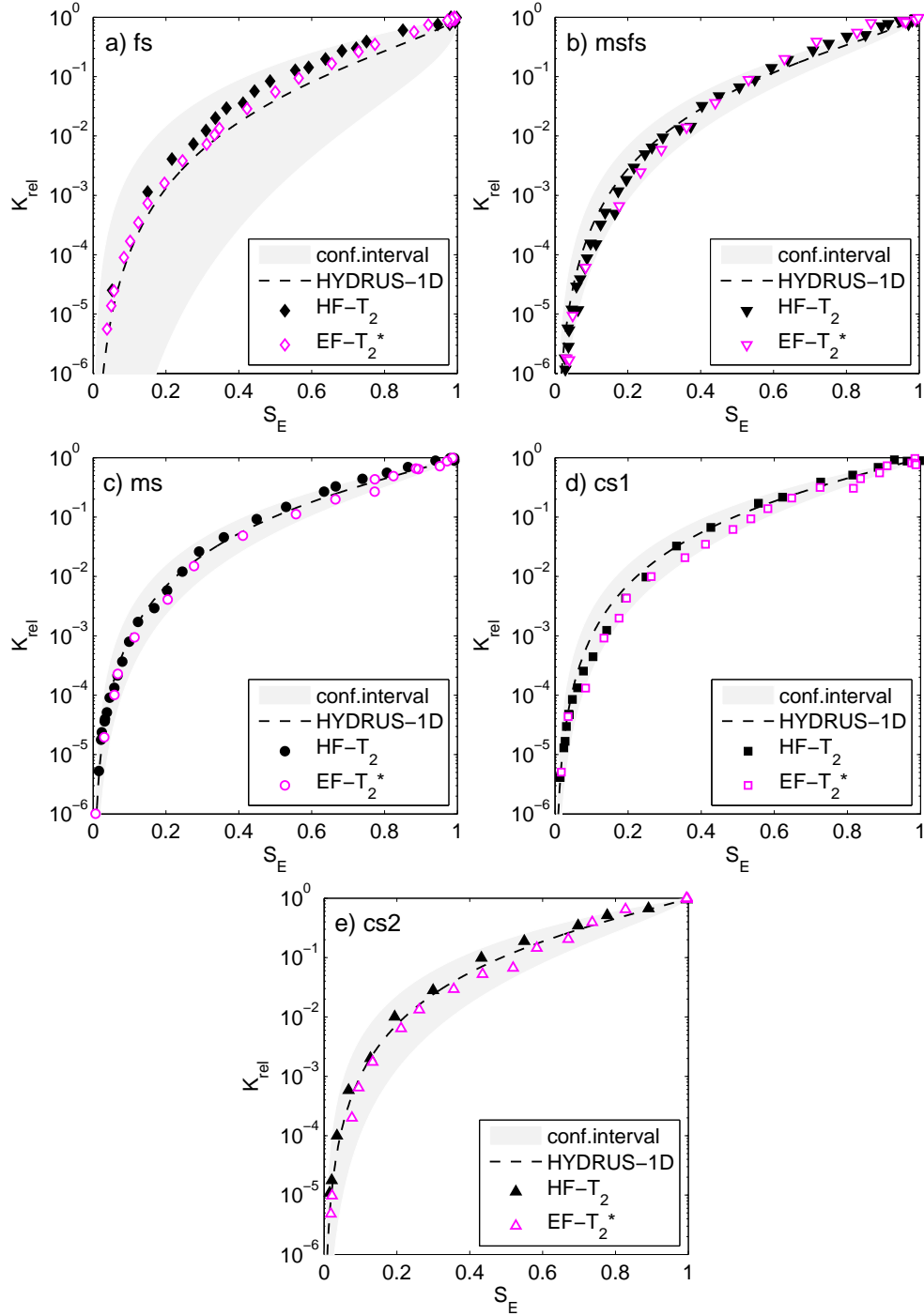


Figure 6.11: Estimations of relative hydraulic conductivity K_{rel} as a function of the effective saturation degree S_E . The predictions from HYDRUS-1D are based on the cumulative outflow data of the drainage experiments (dashed lines with confidence intervals plotted with gray areas). The predictions from T_2 (HFNMR measurements - closed black symbols) are derived from the Brooks-Corey model (Equation 2.8). The predictions from T_2^* (EFNMR measurements - open magenta symbols) are determined according to Equation 6.7.

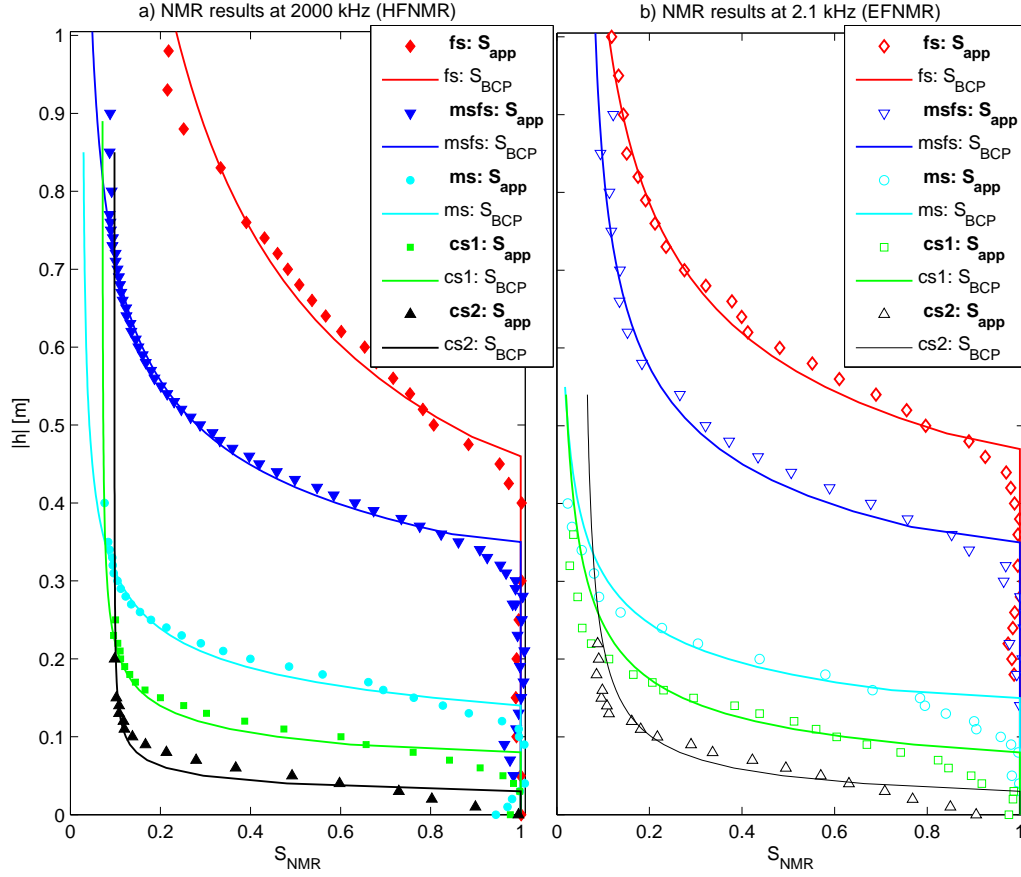


Figure 6.12: Measurements of the apparent NMR water saturation degree (S_{app}) inside the columns by HFNMR (a) and EFNMR (b) compared to the approximations using the Brooks-Corey parameterization (S_{app}).

The BCP obviously leads to a reliable representation of the capillary fringe. As expected from the analysis of the synthetic data example (Figure 6.7), the BCP leads to overestimated S_{NMR} close to 1 for all samples. A parameterization by the unconstrained VG-model (Equation 2.4) might lead to a better representation of the data without these differences near saturation. However, the commonly used relationship $m=1-1/n$ in Equation 2.4 is not valid when approximating WRCs from high resolution column experiments exhibiting sharp air entry points such as the S_{NMR} data in this study (Peters and Durner, 2006). Consequently, both m and n must be considered to be free parameters in the fitting routine. From this two problems follow: First, the parameter space of the inversion scheme increases and leads to a higher degree of nonuniqueness due to the higher dependencies among the VG parameters (Haverkamp et al., 2005). Second, the software HYDRUS-1D does not allow for an independent input of both parameters n and m . Finally, the BC approximation has been chosen for the approximation of the data, which

provides an acceptable data representation in spite of the known uncertainty. Instead of a direct comparison of the fitting parameters, the final prediction of K_{rel} calculated from the results of the BCP inversion is assessed here by comparison with the HYDRUS-1D estimation of K_{rel} using the VGM model (see Table 6.2 and Figure 6.4). The fitting

Table 6.4: Hydraulic parameters estimated from the BCP inversion of both the HFNMR and the EFNMR measurements, BCP means the parameterization of the capillary fringe inside the sand columns after Brooks and Corey (1964).

Sample	λ (HFNMR)	λ (EFNMR)	h_0 (HFNMR)	h_0 (EFNMR)
fs	1.83 ± 0.65	3.46 ± 0.48	45.46 ± 1.60	46.51 ± 0.86
msfs	3.57 ± 0.28	3.75 ± 0.67	34.36 ± 0.38	34.25 ± 0.96
ms	3.24 ± 0.62	3.00 ± 1.67	14.01 ± 0.46	14.37 ± 1.54
cs1	3.32 ± 0.68	2.04 ± 0.81	7.67 ± 0.42	7.92 ± 0.86
cs2	2.97 ± 1.24	1.86 ± 1.01	3.00 ± 0.58	3.27 ± 0.74

parameters from the BCP inversion are given in Table 6.4: h_0 is very well correlated with the grain size of the sand, while λ shows no significant dependency from the grain size. All λ values fitted by the BCP inversion are plausible estimates for homogeneous sand samples with values ranging from 1.8 to 3.8. Compared to the λ results from the approximations of the T_2 times as functions of S_{NMR} (discussed in the previous section, see Table 6.3), the λ estimates from the BCP here are significantly larger. Regarding the corresponding K_{rel} prediction (see Equation 2.8), larger λ values must yield larger K_{rel} estimates. In Figure 6.13, the K_{rel} predictions from the BCP inversion results for the samples are shown and compared with the HYDRUS-1D estimation. As for the estimation from the relaxation times, the parameter a in Equation 2.8 was again set to 3 (samples fs and msfs) and to 2 (samples ms, cs1, and cs2), respectively. As expected, the K_{rel} predictions calculated from the BCP inversion results are slightly larger than the results shown in Figure 6.11, however, they also lie within the confidence intervals of the HYDRUS-1D estimation.

6.3 Discussions and conclusions

NMR experiments at 2000 kHz (HF) and in the earth's field (EF - 2.1 kHz) with partially saturated sand-filled columns (gravity-capillary equilibrium state) show that both methods provide the saturation degrees from S_R (residual water saturation) to $S_{NMR} = 1$. The uncertainties of the saturation degree in EFNMR with up to 3% are larger than in HFNMR with up to 1%. However, it is shown that the shape of the capillary fringe in sands with different grain sizes (from fine to coarse sand) can successfully be reconstructed

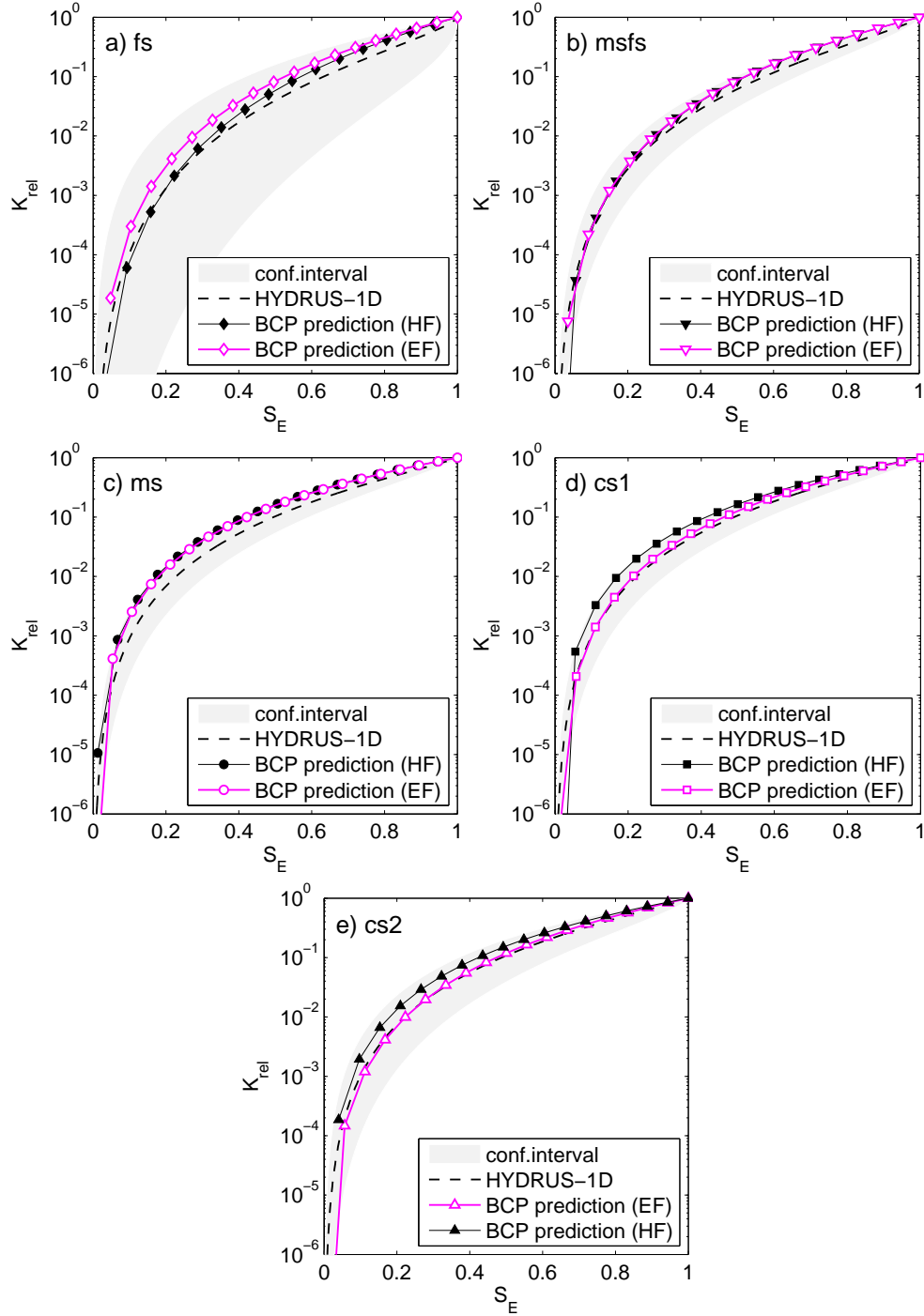


Figure 6.13: Estimations of relative hydraulic conductivity K_{rel} as a function of the effective saturation degree S_E . The predictions from HYDRUS-1D are based on the cumulative outflow data of the drainage experiments (dashed lines with confidence intervals plotted with gray areas). The predictions from the Brooks-Corey parameterization (BCP) of the capillary fringe are calculated according to Equation 2.8.

with HFNMR, as well as with EFNMR. The S/N ratios of the EFNMR signals are observed within the range 2 (residual water) to 15 (saturated conditions) with stacking rates from 25 to 100. Because a similar data quality is usually provided by the MRS method, the EFNMR results shown here are representative for the measurement conditions in the field.

Due to long dead times of the EFNMR signal detection, the residual water saturation degree S_R of materials with short T_2^* times may be underestimated. This is the case when the decrease of T_2^* with decreasing saturation reaches the measurement dead time. Three of the five sand samples show underestimated S_R values when measured with EFNMR. This underestimation is in the range of one third to one half of the real value. Regarding a possible application of EFNMR for soils with silty and clayey content this systematic error is expected to increase, because fine-grained material generally leads to smaller relaxation times. A comprehensive study on EFNMR with partially saturated silty and clayey soils remains an objective for future research. Corresponding experiments must have a layout different from the measurements with sandy material in this study. Capillary fringes in silty and clayey material with a height of at least a few meters will exceed the dimensions that can be handled with columns used as sample holders in the laboratory.

It has been shown that the estimation of the relative hydraulic conductivity K_{rel} of the sands using the T_2 times measured with conventional HFNMR is possible. The key is the behavior of T_2 as a function of the saturation degree according to the Brooks-Corey model (BC) which is valid for material with negligible diffusion relaxation rate. Therefore, a limited applicability of these findings for soils with high contents of magnetic components must be expected. The T_2^* measurements with EFNMR differ from the BC assumption. For the description of the complex dependency of T_2^* from S , the dephasing of the EFNMR signal must be taken into account. The suggested approach is based on the assumption that the dephasing effect decreases with decreasing S_{NMR} , i.e., the influence of the internal gradients is assumed to decrease with decreasing saturation. The suggested empirical model (Equation 6.6) is verified by the experimental data. However, a detailed physical description of the observed phenomenon is an important issue for future research. Additional EFNMR experiments in combination with numerical simulations of the relaxation behaviour on the pore dimension under partially saturated conditions are very promising for a full understanding of the observations in this study. Moreover, such modeling strategies can help to quantify the influence of internal field gradients on the dephasing and on the diffusion relaxation, respectively (Mohnke and Klitzsch, 2010).

It has further been shown that the empirical model to formulate T_2^* as a function of S_{NMR} allows for a K_{rel} prediction from T_2^* measured in the EF (see Equation 6.7). For this prediction, the EF T_2 and T_2^* times for the saturated material must be available, as well as an additional empirical parameter ν controlling the saturation dependency of the dephasing relaxation rate. The parameter ν , that is referred to as the dephasing index, can be found by fitting Equation 6.6, i.e., FID measurements covering a complete spectrum of saturation degrees for S_R to $S=1$ for the material to be investigated are

necessary, preferably in the laboratory. Thus, it must be noted that calibrating the parameter ν could be a limiting criterion when adapting this approach for MRS in practise. On the other hand, because recent MRS research activities deal with the possibility to measure T_2 with MRS equipment in the field (Legchenko et al., 2010), the parameter T_2 can possibly be provided in future MRS measurements without additional effort and lab investigations.

It has also been shown that the direct BC parameterization (BCP) of the NMR saturation distribution inside the sand columns, i.e., BCP of the capillary fringe, leads to reliable K_{rel} predictions when compared to the HYDRUS-1D estimations. Thereby, the estimates of the parameter λ from the BCP inversion are significantly larger than the estimates from the approximations of the T_2 times as functions of S_{NMR} . However, the discrepancy of the final K_{rel} predictions resulting from these differences of λ is quite small. The K_{rel} predictions of both NMR methods lie within the confidence intervals of the HYDRUS-1D estimation.

Based on the findings showed here, the next chapter will focus on the general feasibility of *in situ* predictions of K_{rel} from MRS measurements.

Chapter 7

MRS with focus on the vadose zone - on *in situ* K_{rel} prediction

The magnetic resonance sounding method (MRS) is used for *in situ* investigations of the subsurface aquifer structure (see Chapter 3.3 for details). It directly provides the vertical water content distribution and allows for estimating the saturated hydraulic conductivity from the NMR relaxation times. In this chapter, the potential of this method to provide the relative hydraulic conductivity K_{rel} in the vadose zone is investigated. Based on the findings of the EFNMR measurement at the sand columns in the previous chapter, two different approaches are introduced. The first one is based on the analysis of the relaxation time T_2^* of MRS measurements in the unsaturated zone, and uses the relationship between T_2^* and K_{rel} as derived with Equation 6.7. The second approach parameterizes the natural capillary fringe by means of the model of Brooks and Corey (1964) (BCP), and is a direct adaptation of the BCP inversion introduced with Equations 6.5 in the previous chapter for the column experiments. In doing so, only the NMR signal amplitudes of the MRS measurements are used. The principle feasibilities of both approaches are shown and discussed with real-data examples. The study concerning the BCP inversion is published in (Costabel and Yaramanci, 2011b).

7.1 Adaptation of laboratory interpretation schemes for field strategies

To assess the potential of the MRS method to investigate the vadose zone with its characteristic structure (Figure 7.1a, see also Figure 2.1 and detailed description in Chapter 2.1), one has to analyze the general properties of the so-called MRS kernel, which is the ensemble of sensitivity functions beneath the MRS loop on the surface. Figure 7.1b shows sketchily such an MRS kernel. Detailed explanations on the basics of MRS are given in

Chapter 3.3. By increasing the strenght of the excitation pulse q during the sounding the sensitivity of the method is shifted toward deeper regions, whereas the entire excited range gets broader at the same time. Thus, the resolution of the inverted vertical water content distribution naturally decreases with increasing depth. On the other hand, the very shallow subsurface (e.g., the root zone) is barely tapped by the MRS kernel even for the lowest q . In general, the MRS resolution properties depend on the chosen loop size: The smaller the loop, the better the resolution. However, the excited volume beneath the loop depends on its size, and the amplitude of the resulting MR response signal becomes smaller with decreasing loop size, e.g. only a few tens of nV in a loop with 10 m diameter. Thus, the MRS loop size cannot be chosen arbitrarily small.

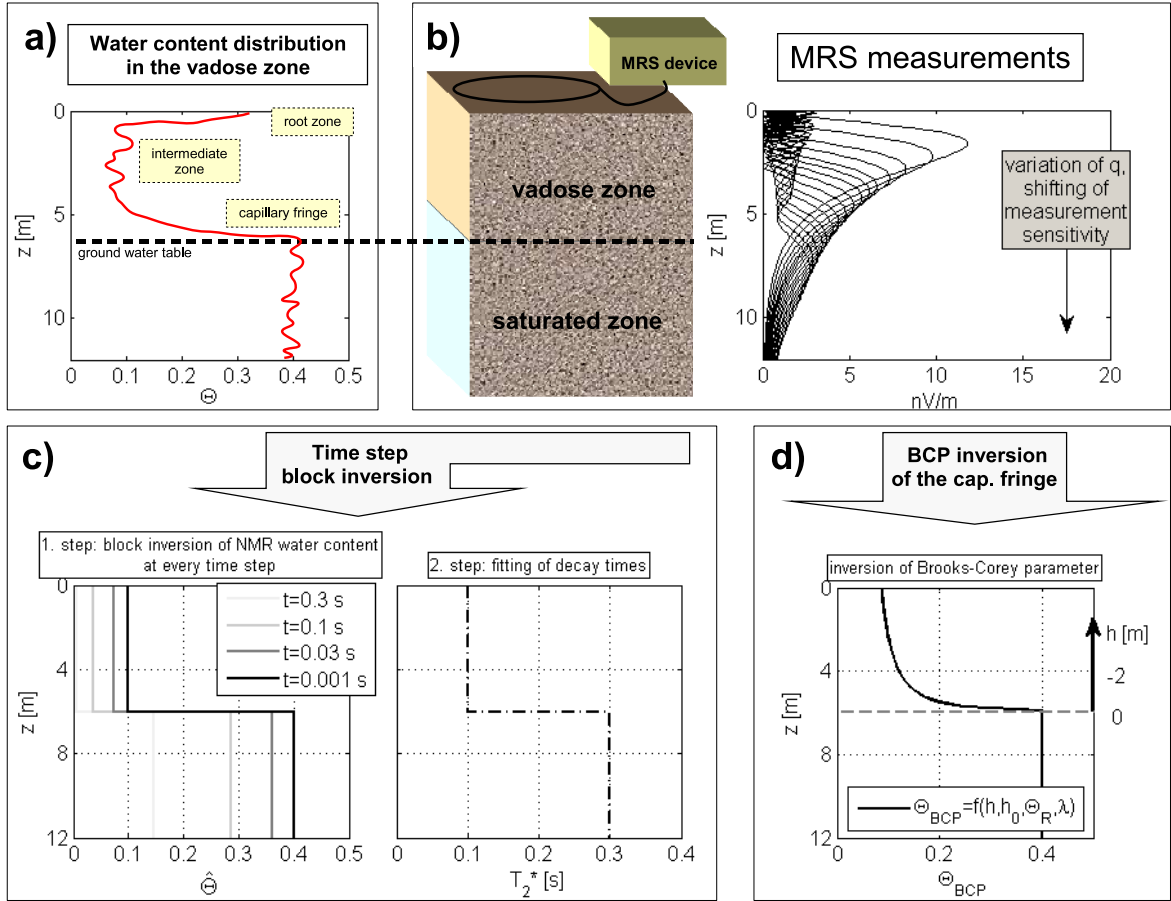


Figure 7.1: Measurement and interpretation schemes of MRS with focus on the vadose zone: (a) Schematic water content distribution inside the vadose zone, (b) Sensitivity functions of the MRS survey, (c) Blocky time step inversion: reconstruction of the water content and T_2^* of both the unsaturated and the saturated zone, (d) BCP inversion - approximation of the capillary fringe by the Brooks-Corey parameterization.

So far, MRS measurements in the root zone are impossible for mainly two reason: First, focussing the MRS sensitivity range on the nearest subsurface, e.g., with small MRS loops, will result in NMR signal amplitudes below the detectability. Second, for technical reasons q cannot optionally be decreased. Thus, the approaches suggested here will neglect the root zone completely, while the investigation of both the intermediate zone and the capillary fringe of the vadose zone seems reliable.

In the previous chapter, two interpretation schemes for column experiments with laboratory NMR were applied (see Figure 6.1): the time step inversion to reconstruct both the water content and the relaxation time distributions inside the columns and the BCP inversion, which is based on the reconstruction of the capillary fringe by means of its parameterization after Brooks and Corey (1964). In principle, both inversion schemes can be adapted for the interpretation of MRS data (Figure 7.1c and d), whereas some simplifications must be made to account for the poorer resolution properties of the MRS kernel function in comparison to the sensitivity distribution of the laboratory NMR coils (see Chapter 6.1.1 for details). As shown below, additional *a priori* information must be available and must be included into the inversion calculation, e.g., the water table, to get reliable results. In the following section, an adaptation of the time step inversion for MRS is introduced, which focusses on the characterization of the intermediate zone (Figure 7.1c). Under the conditions that, first, the extent of the capillary fringe is small compared to the dimension of the intermediate zone and, second, the intermediate zone can be considered to be approximately homogeneous, a blocky two-layer model is assumed, which distinguishes between the saturated and the unsaturated zone. As inversion results the mean saturation degree of the unsaturated zone is provided, as well as its relaxation time, which can be used as a proxy for the mean relative hydraulic conductivity K_{rel} inside the unsaturated layer. For the adaptation of the Brooks-Corey parameterization (BCP) for MRS, the assumption of a well developed capillary fringe in a relatively shallow depth is made, so that the MRS kernel is able to resolve the gradual increase of the water content distribution (Figure 7.1d). Using the pore-size-distribution (PSD) index λ as inversion result from the BCP, K_{rel} can be predicted as function of the saturation degree S according to Equation 2.8.

7.2 K_{rel} estimation from T_2^*

7.2.1 Blocky time step inversion with fixed groundwater table

As described above, for the adaptation of the time step inversion here, the vadose zone is simplified to be a partially saturated layer above a homogeneous saturated zone. With the water table z_{table} given as the boundary between both layers (necessary *a priori* information), the MRS dataset is inverted in two steps (Fig.7.1c) according to the principle of the time step inversion (Mohnke and Yaramanci, 2005). The first step is the 1D-inversion

(see also Eq.3.40 and 3.41) for every time step t_n of the measurement, each with fixed z_{table} that distinguishes between the unsaturated (U) and the saturated (S) layer:

$$E(t_n, q) = \int_z K_{1D}(q, z) \hat{\Theta}(t_n, z) dz$$

$$\hat{\Theta}(t_n, z) = \begin{cases} \hat{\Theta}^U(t_n, z), & z < z_{table} \\ \hat{\Theta}^S(t_n, z), & z \geq z_{table} \end{cases} \quad (7.1)$$

This results in a time dependend quantity $\hat{\Theta}$ that is the 'water content' still visible in the NMR signal at the measurement time step t_n . The second step is the mono-exponential fitting of $\hat{\Theta}$ for both layers:

$$\hat{\Theta}^{U,S}(t) = \Theta_{NMR}^{U,S} \exp \left[-\frac{t}{T_2^{*U,S}} \right] \quad (7.2)$$

In principle, the approximation of $\hat{\Theta}(t)$ can also be applied as a multi-exponential fit. However, the use of Equation 6.7 necessitates a mean $T_{2,U}^*$ depending on S_{NMR} for the estimation of K_{rel} and thus, the mono-exponential representation is sufficient here. Using Equation 6.7 with $S_{NMR} = \Theta_{NMR}^U / \Theta_{NMR}^S$ and the T_2^* -times of both layers, K_{rel} can be estimated as a mean value for the intermediate zone. In doing so, the parameters T_2 and ν in Equation 6.7 must be given as *a priori* information.

7.2.2 Real data example from test field Haldensleben

To test the blocky time step inversion described above with focus on the characterization of the vadose zone, a data example from the test site Haldensleben at location B8 was chosen. This site was investigated by Yaramanci et al. (1999). It exhibits a quite homogeneous sand aquifer followed by a till layer in about 47 m depth. The aquifer is unconfined and the water table can be found in about 20 to 22 m depth varying with the season. Figure 7.2 shows a 1D-sketch of the lithology as interpreted from borehole investigation compared to the results of a usual MRS smooth inversion.

In 2008, an MRS experiment with the GMR instrument (Walsh, 2008) was conducted to test its ability for vadose zone investigations. For this purpose measurements were performed with an unusual high number of pulse moments q , a shortened instrumental dead time, and a limited penetration depth, i.e., the maximum pulse moment q_{max} was determined such that the deepest region to be excited by the pulse lies just inside the saturated zone, while for each $q < q_{max}$ the resulting sensitivity range lies within the unsaturated zone. In Table 7.1, the measurement configurations of this survey are listed and compared to the configurations of a measurement at the same site, but with focus on the deeper aquifer structure (i.e., the data base of the result shown in Figure 7.2).

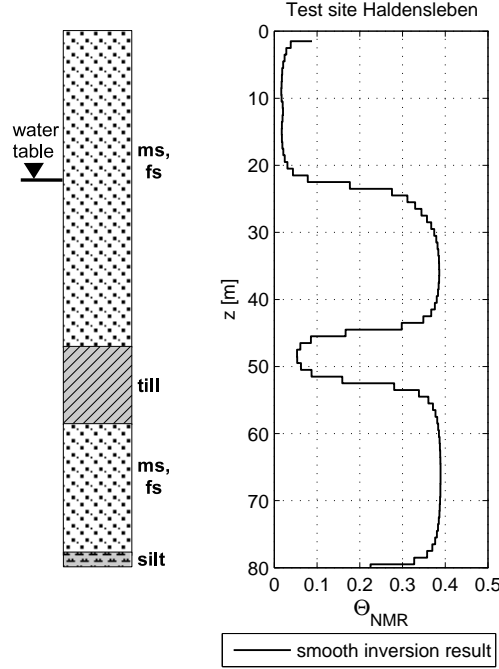


Figure 7.2: The lithology of the test site Haldensleben interpreted from borehole data compared with a typical smooth MRS inversion result discovering the aquifer structure (MRS measurement configuration in Table 7.1).

As derived in Chapter 6.2.4, the relaxation time T_2^* for partially saturated sand measured in the earth's magnetic field can be used as a proxy for the unsaturated hydraulic conductivity K_{rel} , if additional information is at hand: both the T_2^* and T_2 times at saturation and an estimate of the dephasing index ν . Inversion strategies for MRS data must be applied that provide, beside the information of the NMR water content Θ_{NMR} , also the T_2^* distribution in the unsaturated zone. Müller-Petke and Yaramanci (2010) developed a comprehensive inversion of the whole MRS data set at once, the so-called QT inversion, which leads to very promising results regarding the partial water content distribution, i.e., the water content in dependency on different relaxation regimes. It was shown (Müller-Petke, 2009; Müller-Petke and Yaramanci, 2010) that a smooth QT inversion exhibits better properties compared to a smooth time step inversion (Mohnke and Yaramanci, 2005). In Figure 7.3a and 7.3b, two QT inversion results for the Haldensleben survey with focus on the vadose zone are shown as surface plots, i.e., the partial NMR water content distribution as a function of T_2^* and z . Figure 7.3a depicts the inversion result with pure smoothing constraints for both Θ_{NMR} and T_2^* , whereas the

Table 7.1: MRS measurement configurations in Haldensleben.

	focus on the aquifer structure	focus on the vadose zone
MRS device	NUMIS (Legchenko and Valla, 2002)	GMR (Walsh, 2008)
loop layout	circle	circle
loop diameter [m]	100	50
number of turns	1	2
number of pulse moments	20	64
pulse duration [ms]	42	40
min. q [As]	0.12	0.02
max. q [As]	14.27	2.11
dead time [ms]	40	17
stacking number	24	4

result in Figure 7.3b was found with additional constraints on the upper limit of Θ_{NMR} . The data approximation ΔD of both results is almost the same with about $4.5 \cdot 10^{-8}$ V. Both inversion results show water in the vadose zone with decreased T_2^* times as expected (see Chapter 6.2.3). When comparing the spatial distributions of Θ_{NMR} (Figure 7.3c), it is obvious that constraining the upper limit of Θ_{NMR} leads to a more realistic result, and even the water table is found at a reliable depth. However, regarding the spatial distributions of the logarithmic means of T_2^* (Figure 7.3d), the inversion results do not show significant differences. Both inversion schemes show the same smooth increase of T_2^* in the vicinity of the water table. It is very difficult to determine a certain T_2^* value for the saturated zone, which is, however, necessary for the K_{rel} estimation using the interpretation scheme with Equation 6.7. In general, also the exact determination of Θ_{NMR} for the saturated zone is problematic using any kind of smooth inversion, because the shape of the Θ_{NMR} distribution strongly depends on the parameters controlling the smoothness constraints.

In fact, inversion strategies should be preferred that allow for including exact *a priori* information to decrease the degree of ambiguity. Further developements of the QT inversion strategy such as the integration of the block inversion principle and fixed boundaries are planned for the future (Müller-Petke and Günther, pers. comm.). Such developements are very promising regarding the investigation of the vadose zone. However, as long as these options are not available for the QT inversion, in this work the time step inversion scheme with fixed water table as introduced above will be tested. Because the investigation site Haldensleben exhibits a quite large intermediate zone compared to the expected extent of the capillary fringe (in medium sand about some decimeters, see Figures B.3 and B.4), it is plausible to make the assumptions of a blocky subsurface structure. Figure 7.4b shows the inversion result using the two-layer model (saturated and unsaturated

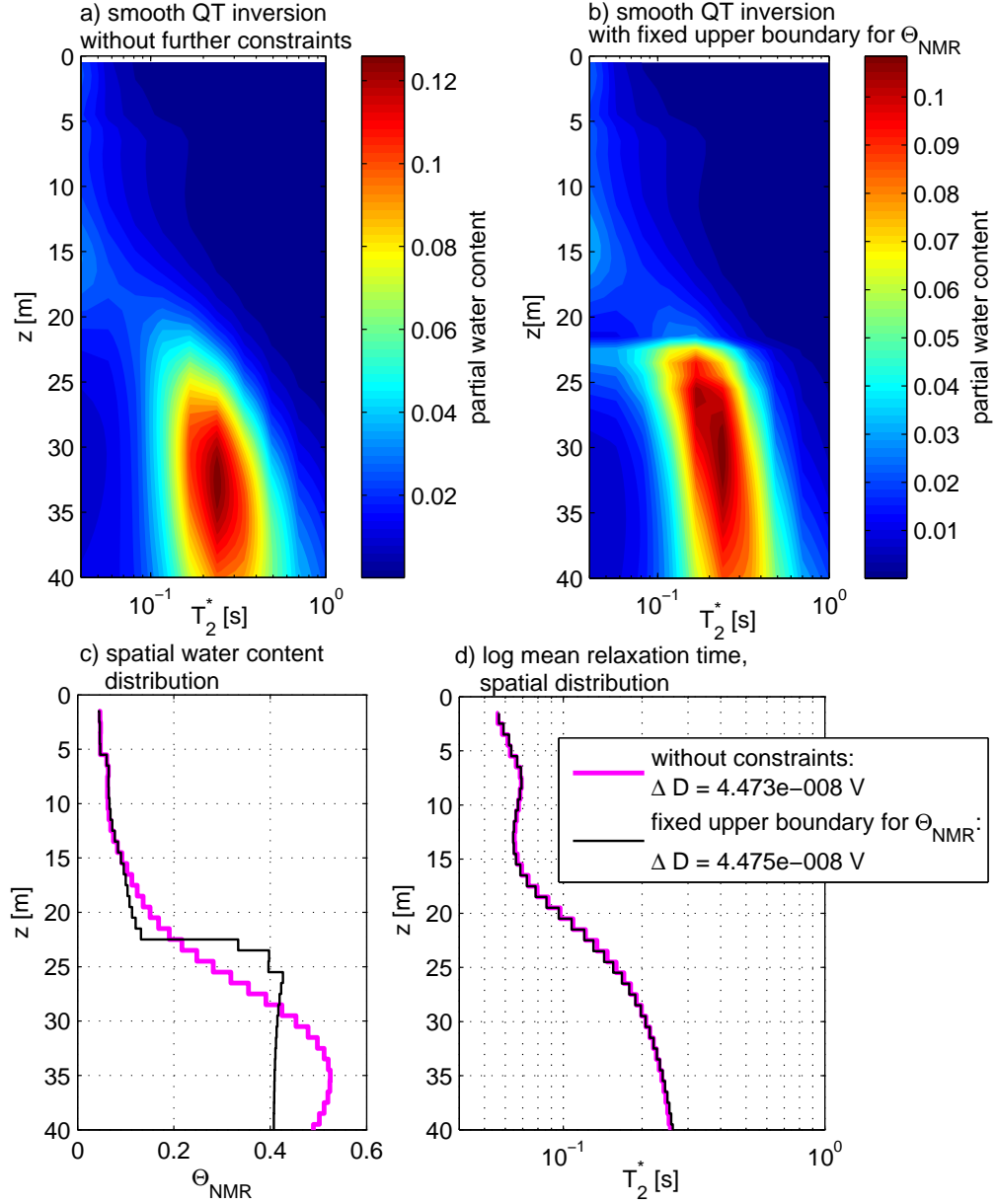


Figure 7.3: Results of the QT inversion (Müller-Petke and Yaramanci, 2010) with smoothing constraints applied at a data example from the Haldensleben test site, partial water content distribution without further constraints (a) and with an upper limit for the total NMR water content (b), comparison of the total NMR water content (c) and the logarithmic mean relaxation time T_2^* (d) of both results.

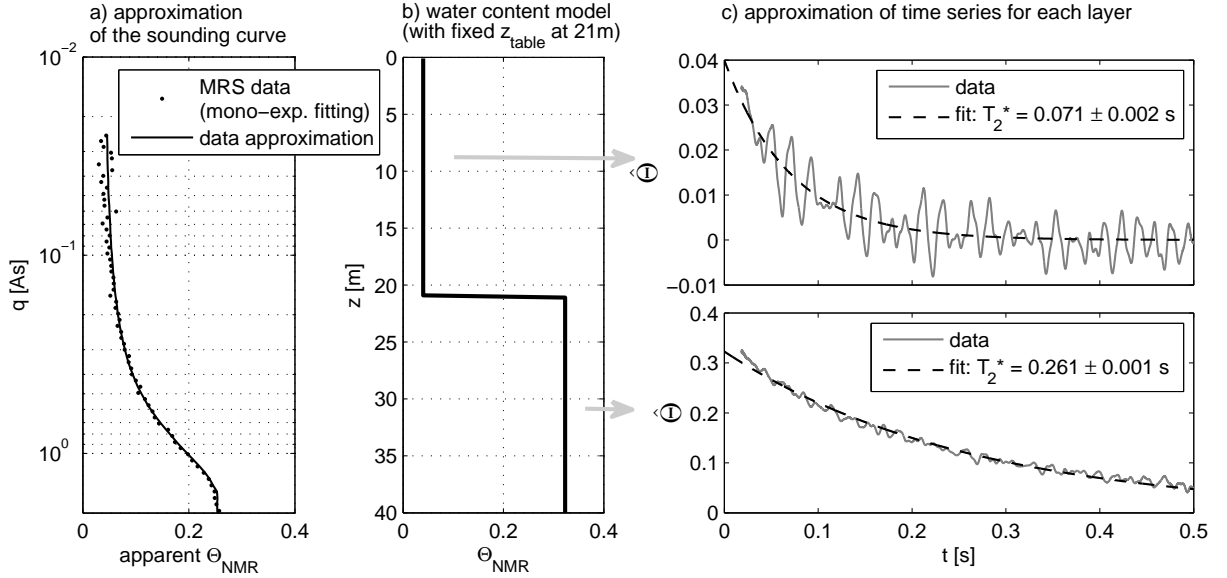


Figure 7.4: Result of the blocky time step inversion applied to the data from the Haldensleben test site with fixed water table at 21 m: (a) approximation of the E_0 -amplitudes normalized to values representing the apparent water content, (b) water content block model, (c) approximation of T_2^* for the unsaturated and the saturated zone.

zone) with a ground water table z_{table} at 21 m. Below z_{table} , the water content Θ_{NMR} is found with 0.32. The unsaturated zone exhibits a Θ_{NMR} of 0.04, which corresponds to a saturation degree S_{NMR} of 0.13. The approximation of the sounding curve in Figure 7.4a is excellent meaning that the block model assumption also satisfies the measured MRS data. In Figure 7.4c, the exponentially decaying $\hat{\Theta}(t)$ curves for both layers are shown. The mono-exponential approximations of these curves provide different T_2^* times with a smaller T_2^* value for the unsaturated layer as expected. In the saturated zone T_2^* is 0.26 s and in the unsaturated zone 0.07 s. These values are similar to those of the sample msfs from the laboratory study in Figure 6.10. I thus use the parameters T_2 and ν as found for the sample msfs (Table 6.3) to estimate K_{rel} roughly for the unsaturated zone in Haldensleben according to Equation 6.7 and to test, whether the resulting K_{rel} estimate is in a reliable range. In addition, the dependency of the K_{rel} estimate on the (*a priori*) input of z_{table} will be tested. Unfortunately, no samples from the aquifer in Haldensleben for laboratory investigations were available and thus, the essential parameters for the K_{rel} estimation could not be determined for the original material.

Figure 7.5 shows a set of inversion results and the corresponding K_{rel} estimations for different z_{table} within the range 21 ± 2 m, which is expected to be the range of natural seasonal variation of z_{table} in this area of investigation. In this way, the influence of a possibly erroneous determination of z_{table} and its impact on the estimation of Θ_{NMR} , $T_2^{*U,S}$, and the resulting K_{rel} can be assessed. The bold black lines in the subplots of

Figure 7.5 depict the optimal inversion result (smallest RMS value) with a z_{table} at 21 m. Obviously, Θ_{NMR} in the unsaturated layer is determined very stable independently from the chosen depth of the water table, the same for T_2^* in the saturated zone. The T_2^* value in the unsaturated layer spreads from 0.05 to 0.09, while the spreading of Θ_{NMR} in the saturated layer ranges from 0.3 to 0.36. However, finally the variance of K_{rel} in the unsaturated zone lies within half a decade, which is acceptable regarding common methods for determining the hydraulic conductivity. It is expected, that systematic errors due to uncertainties of the parameters T_2 and ν will have a greater impact on the final K_{rel} results. Strategies for determining these parameters for the application in the field is an important aim of future work.

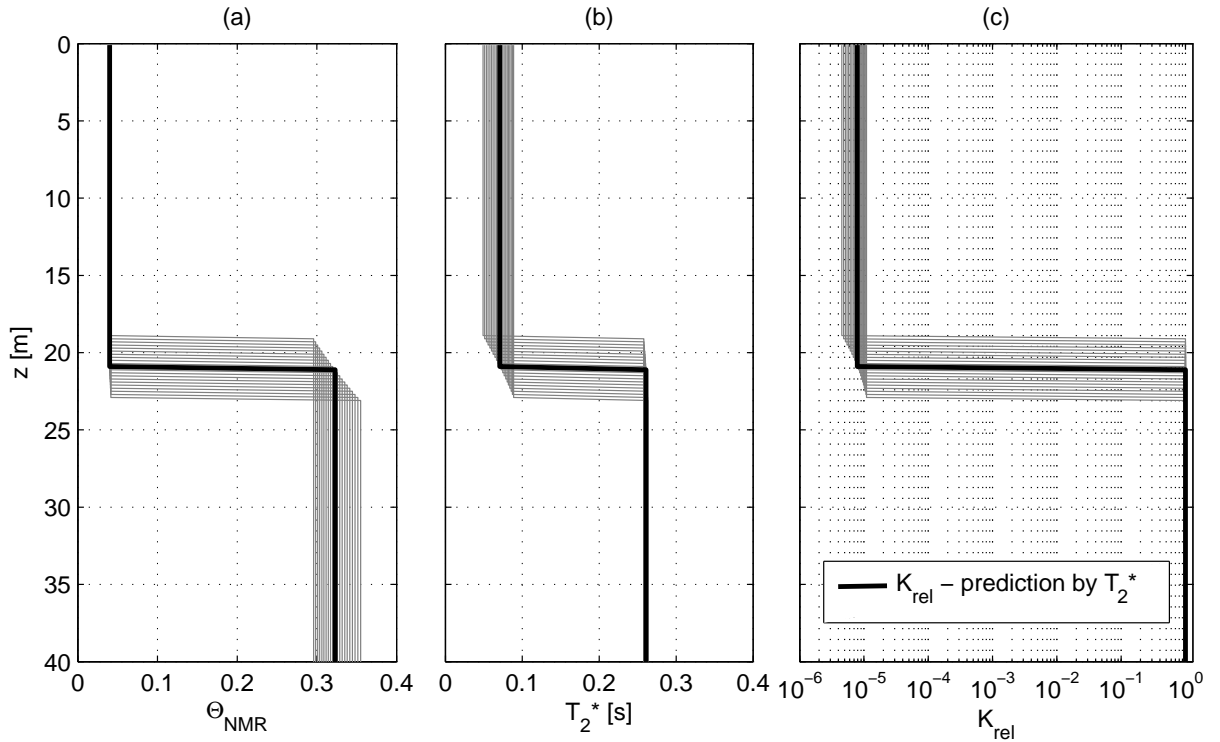


Figure 7.5: Results of the blocky time step inversion applied to the data from the Haldensleben test site with varying water table from 19 to 23 m: (a) spatial water content distribution, (b) spatial T_2^* -distribution, (c) K_{rel} estimates calculated with Equation 6.7.

7.3 K_{rel} estimation based on parameterization of the capillary fringe

7.3.1 MRS inversion based on Brooks-Corey parameterization

It was shown in the previous chapter that the Brooks-Corey parameterization (BCP) of the capillary fringe in sand columns leads to reliable estimations of K_{rel} as a function of the saturation degree (Figure 6.13). This approach is now adapted for the interpretation of MRS data. The MRS forward problem (Equation 3.40) is reformulated by using the BC representation of the subsurface water content above the water table, i.e., by using Equations 2.3 and 2.5:

$$E_{0,BCP}(q) = \int_z \kappa_{1D}(q, z) \Theta_{BCP}(z) dz$$

$$\Theta_{BCP}(z) = \begin{cases} \Theta_R + (\Theta_S - \Theta_R) \left(\frac{h_0}{h} \right)^\lambda, & z < z_{table} \text{ with } h = z - z_{table} \\ \Theta_S, & z \geq z_{table} \end{cases} \quad (7.3)$$

Under the assumption that the capillary fringe is well developed in a homogeneous sediment and with a given water table z_{table} ($h=0$), Equation 7.3 can be inverted directly for discovering the BC parameters. The inversion scheme starts with a user-defined model, i.e., starting values for λ , h_0 , Θ_R and Θ_S . As a first step, the corresponding water content distribution $\Theta_{BCP}(z)$ is reconstructed. Second, using $\Theta_{BCP}(z)$ and the forward operator κ_{1D} the sounding curve $E_{0,BCP}(q)$ is calculated and compared to the MRS measurements $E_0(q)$. Afterward, the BC parameters for the calculation of $\Theta_{BCP}(z)$ are changed in order to minimize the differences between $E_{0,BCP}(q)$ and $E_0(q)$ by means of least squares. Both steps are repeated until $E_{0,BCP}(q)$ and $E_0(q)$ match within a user defined threshold. An optimization algorithm working with conjugated gradients (MathWorks, 2007) to solve this inversion problem automatically was used.

7.3.2 Feasibility study with synthetic data

First, the question of whether the resolution properties of the MRS kernel function are appropriate to provide reliable estimates of the BC parameters by using the inversion scheme described above arises. The results of the BCP inversion are expected to be more accurate when more pulse moments with adequate sensitivity cover the region of the capillary fringe.

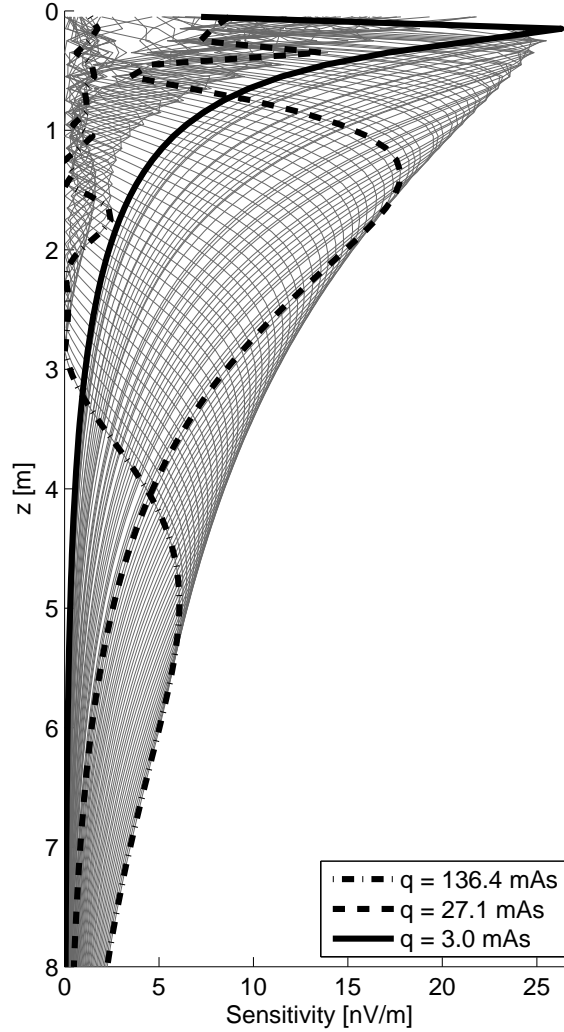


Figure 7.6: Sensitivity functions of the simulated MRS measurements above a water table at 2-m depth, calculated for a figure-eight loop with a 10-m diameter. The number of pulse moments is 75, with values in the range of 3.0 to 136.4 mAs (gray solid lines). Three curves with corresponding pulse moments q are highlighted for orientation.

In the following, the inversion scheme is tested with a set of synthetic models. The forward operator κ_{1D} for this test was calculated according to the real data example that is introduced later. It consists of 75 pulse moments q in the range of 3 to 136.4 mAs. A figure-eight loop with 10 m diameter was assumed above a ground with a resistivity of $3000 \Omega m$ in the unsaturated zone above $z_{table}=2$ m and $280 \Omega m$ in the saturated zone beneath z_{table} . All sensitivity functions of κ_{1D} are shown in Figure 7.6 as gray solid lines to illustrate the vertical coverage beneath the loop. Some curves are highlighted and depicted in the legend with the associated q for a better orientation.

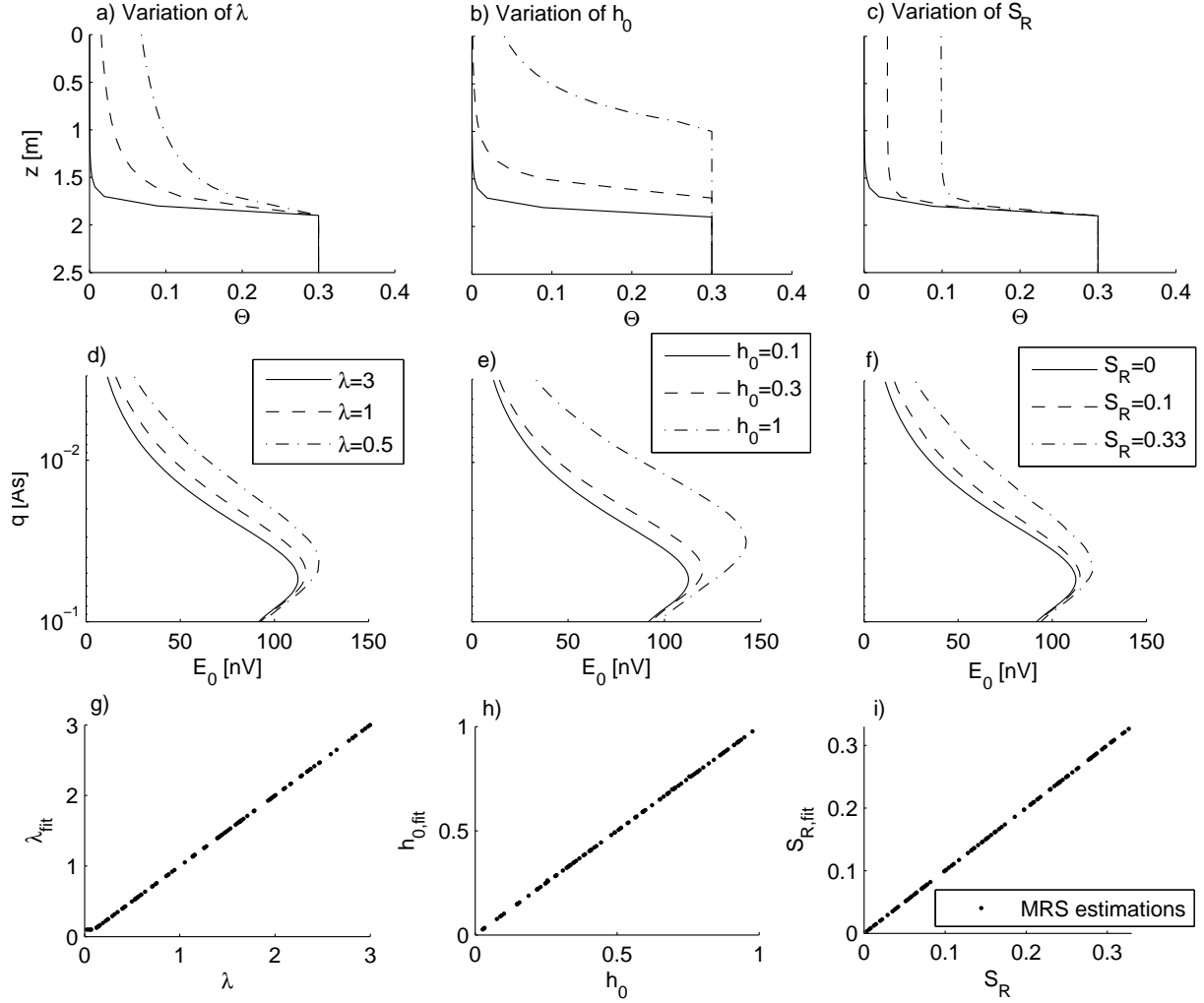


Figure 7.7: (a-c) Example water content models for the synthetic tests of the BCP inversion. The capillary fringe is reconstructed by the BC parameters λ , h_0 and S_R , whereas the water content Θ_S beneath the water table ($z_{table}=2$ m) is constant with 0.3. (d-f) The MRS sounding curves forward calculated from the curves in (a-c) without additional noise. (g-i) The correlation of the inverted BC parameter (y-axes) and the input values (x-axes) for 100 models with uniform distributed random BC values within the ranges $0.01 < \lambda < 3$, $0.01 < h_0 < 1$, and $0 < S_R < 0.33$.

I use a set of different synthetic models for the test of the resolution properties. All models exhibit a water table z_{table} at 2 m and a water content Θ_S of 30% beneath z_{table} . The BC parameters for the reconstruction of the capillary fringe in each model are determined as uniform distributed random values in a realistic range (λ : from 0.01 to 3, h_0 : from 0.01 to 1, S_R : from 0 to 0.33). In Figure 7.7a to c, examples of the resulting water content distributions are depicted to show the influence of each BC parameter. As already

explained in Chapter 2.3 (Figure 2.3), the parameter λ (Figure 7.7a) controls the slope of the capillary fringe, while h_0 (Figure 7.7b) represents the height above the water table with completely water saturated pore space. The saturated zone generally starts at a certain depth above the water table, i.e., at $z = z_{table} + h_0$. The residual water saturation degree $S_R = \Theta_R/\Theta_S$ (Figure 7.7c) controls the asymptotic value of the water content with increasing distance above z_{table} . Figure 7.7d to 7.7f show the sounding curves corresponding to the models in Figures 7.7a to 7.7c. We note that the sounding curves in Figure 7.7d (calculated for different λ with $S_R = 0$) look very similar to those in Figure 7.7f (calculated for different S_R with $\lambda = 3$). Thus, ambiguities between λ and S_R must be expected when applying the BCP inversion scheme introduced above. However, the application of the BCP inversion scheme at the pure synthetic sounding curves (without any noise) leads to a perfect reconstruction of the BC parameters. In Figure 7.7g to 7.7i the inverted BC parameters (after 100 repeated runs with randomly determined parameters) are plotted against the input values. Obviously, the BCP inversion scheme works accurately for any combination of the BC parameters in the given ranges, at least for noise-free measurements.

For the following tests, some noise is added to the synthetic sounding curves and the numerical experiment is repeated. The noise is realized as zero-mean normal distributed random values added as distortion to the E_0 amplitudes, whereby the standard deviation is referred to as the noise level. For all further numerical experiments the number of models with randomly determined BC parameters is 100. Once a model is determined, the corresponding sounding curves are superposed with noise 100 times, i.e., for each model one gets 100 different data sets, each with varied noise of the same magnitude. The inversion is applied to each data set, and afterward, mean value and standard deviation of each fitted BC parameter are calculated.

For the first test, the noise level is unrealistic small at 1 nV. In Figure 7.8a and 7.8c, the ambiguity problem between λ and S_R mentioned above is clearly visible. For both parameters the estimations and the real values are bad correlated (black dots) and the solid line depicting the standard deviation of the parameter estimation is in the same magnitude as the estimated values themselves. Obviously, a reliable reconstruction of both parameters λ and S_R is not possible at the same time, not even under best noise conditions. From this finding one must conclude that the BCP inversion scheme must be applied with reduced parameter space, i.e., the S_R must be given as a priori information. Usually, the water content interpreted from MRS measurements is interpreted as the effective water content (Legchenko et al., 2002), i.e., the water content reduced by the water in the smallest pores. Small pores exhibit small relaxation times that cannot be recorded in MRS due to the long measurement dead times of the available MRS equipment. Because Θ_R is related to small pores, one may reliably assume $S_R=0$ as a priori value for the BCP inversion.

In Figure 7.9 the results for the estimation of λ and h_0 are shown for the case of keeping $S_R = 0$ as a constant during the inversion process. At a noise level of 1 nV (Figure 7.9a

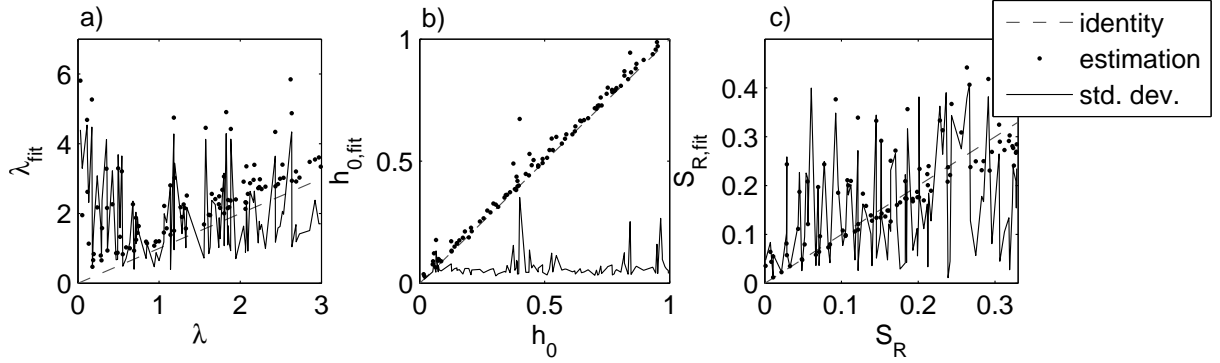


Figure 7.8: Comparison of the mean values of the inverted BC parameters (y-axes) and the input values (x-axes) for 100 models with uniform distributed random BC values within the ranges (a) $0.01 < \lambda < 3$, (b) $0.01 < h_0 < 1$, and (c) $0 < S_R < 0.33$ (dots). The noise level of the sounding curves was set to 1 nV. The solid lines represent the standard deviation for each parameter after 100 runs (only the noise was varied 100 times for each model). The dashed lines denote the identity for orientation.

and 7.9b), both parameters can be determined with small uncertainties. The standard deviation of λ , depicted by the black solid lines, is smaller than 10% for $\lambda < 2.2$; for h_0 it is about 0.02 to 0.05 m and remains constant over the whole range of h_0 . For λ -values larger than 2.2, large errors occur. This is obviously the limit given by the resolution properties of the forward operator κ_{1D} used for the simulations. Above a certain threshold it is not possible to distinguish between large λ -values, because a large λ corresponds with a sharp gradient zone between the unsaturated and the saturated zone that cannot be resolved by the MRS measurements. In Figures 7.9c and 7.9d, the estimation results for λ and h_0 at a noise level of 10 nV are shown. The standard error for both parameters is unacceptable large and the correlation of the estimated and the real values is very weak. An increased noise level higher than 10 nV obviously requires a further parameter reduction for the BCP inversion scheme, at least for the example loop configuration discussed here.

Because λ is the governing parameter for the K_{rel} estimation (see Equation 2.8), I want to test in the following how accurate λ can be estimated when h_0 is given as a priori information. For the next investigation both λ and h_0 are randomly determined, whereas for the inversion scheme h_0 is held constant. S_R was set again to 0. Two different noise levels were applied: 10 and 20 nV. In Figure 7.10, the estimations of λ are compared to the real values. The standard deviation for λ in the case of 10-nV noise varies from 0.1 for $\lambda < 1$ to about 0.3 for $1 < \lambda < 1.8$. For $\lambda > 1.8$ the uncertainty abruptly increases to values up to 2 and higher, so the limit for a reliable estimation for λ is reached here. For the case of 20-nV noise this limit is also reached at $\lambda = 1.8$, whereas the standard deviation is increased to a range of 0.3 (for $\lambda < 1$) to about 0.5 (for $1 < \lambda < 1.8$). I conclude that under realistic noise conditions (noise level at 10 to 20 nV) the estimation of λ provides reliable results with acceptable uncertainties for $\lambda < 1.8$, whereas the BC

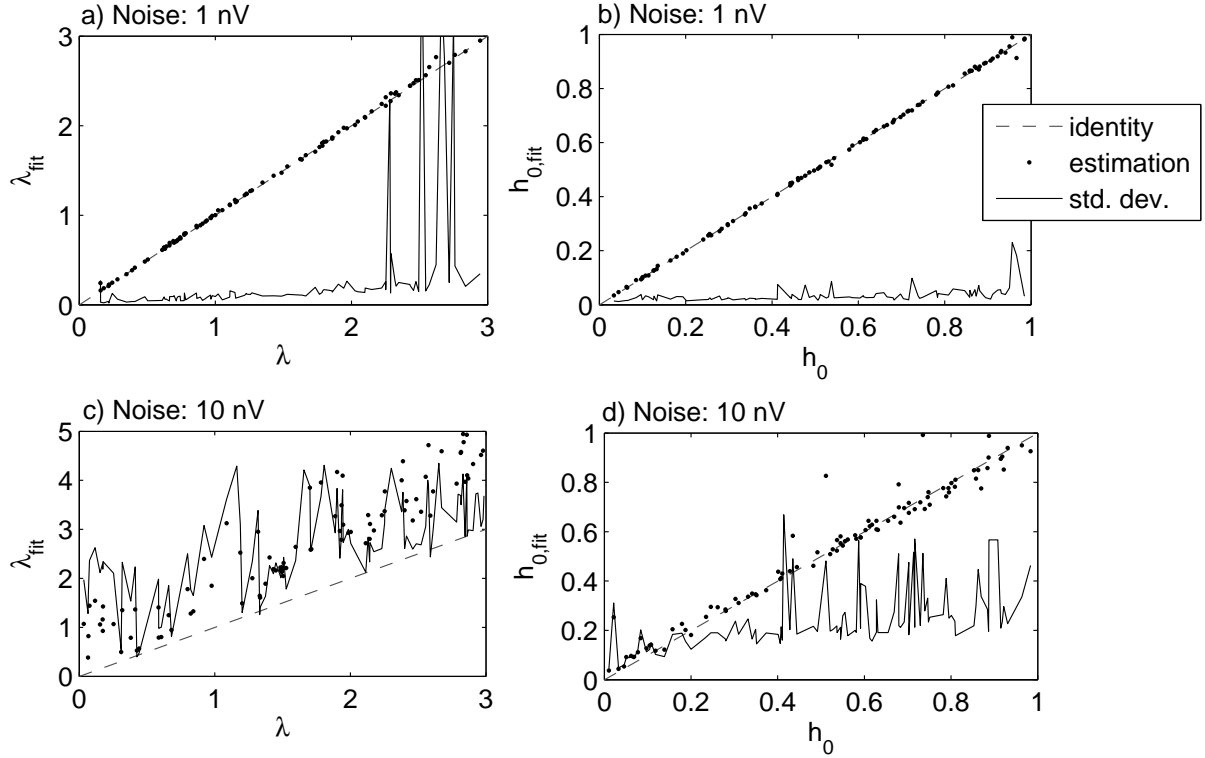


Figure 7.9: Comparison of the mean values of the inverted BC parameters (y-axes) and the input values (x-axes). Only λ and h_0 were varied randomly within the ranges $0.01 < \lambda < 3$ and $0.01 < h_0 < 1$ (dots), whereas S_R was set to 0. The noise level of the sounding curves was set to (a and b) 1 nV, and (c and d) 10 nV. For each noise level, 100 individual models were investigated. The solid lines represent the standard deviations for each parameter after 100 runs (only the noise was varied 100 times for each model). The dashed lines denote the identity for orientation.

parameter h_0 and S_R must be given as *a priori*.

The test was repeated with the same conditions for another model with a water table z_{table} at 5-m depth. The simulated measurement configuration, i.e., the loop geometry and q distribution, was identical to the prior test with one exception: The number of pulse moments was enlarged up to 128 in the range from 3 to 1400 Ams to increase the investigation depth. In the resistivity model, the boundary between the unsaturated ($3000 \Omega m$) and the saturated ($280 \Omega m$) zones was modified with z_{table} for calculating κ_{1D} . The estimations of λ are shown in Figure 7.10c for 10-nV noise and in Figure 7.10d for 20-nV noise. Obviously, the upper limit for a reliable estimation of λ decreases down to 1.5 for the model with deeper z_{table} . On the other hand, the standard deviation of λ is decreased in the range $\lambda < 1.5$ compared to the results of the model with $z_{table}=2$ m. From this finding one must conclude that the resolution in the deeper regions decreases; that

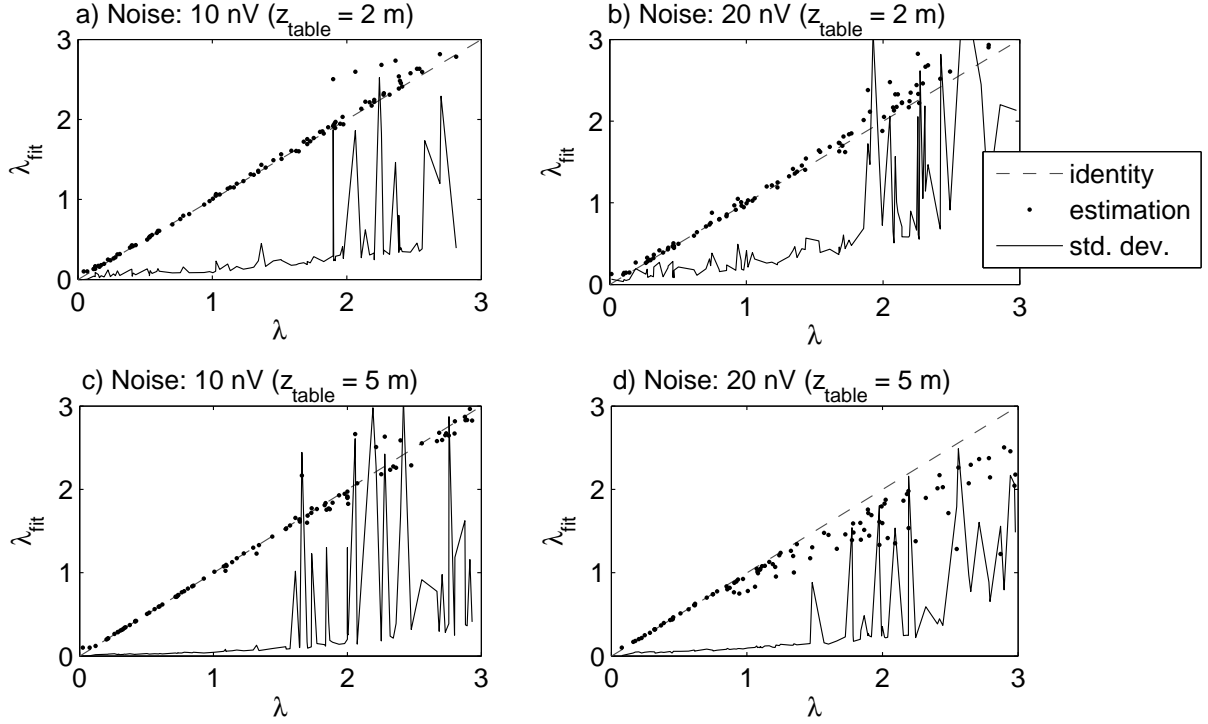


Figure 7.10: Comparison of the mean values of the inverted BC parameter λ (y-axes) and the input value for λ (x-axes), which was varied randomly within the range $0.01 < \lambda < 3$ (dots). The parameter h_0 was also varied randomly within the range $0.01 < h_0 < 1$, but it was held constant during the inversion; S_R was set to 0. The water table z_{table} was determined at (a and b) 2 m and (c and d) 5 m. The noise level of the sounding curves for (a) and (c) was set to 10 nV and for (b) and (d) it was set to 20 nV. For each noise level and for each water table, 100 individual models were investigated. The solid lines represent the standard deviations for each parameter after 100 runs (only the noise was varied 100 times for each model). The dashed lines denote the identity for orientation.

is, the upper limit for a reliable estimation of λ decreases for a deeper z_{table} . However, the uncertainty of λ in the reliable range is smaller due to the increased information content given by the increased number of pulse moments. Additional numerical experiments in the future will systematically investigate the limits for the estimation of λ in dependency of z_{table} and for other types of MRS loops.

Now, I will test how the number of pulse moments and the gap between adjacent pulse moments (i.e., the coverage of the corresponding sensitivity functions) affect the accuracy of the λ estimation by the BCP inversion. Another MRS measurement was simulated, again with a figure-eight loop of 10-m diameter and pulse moments in the range of 3 to 1400 Ams. The water content model is the same as described above, i.e., $z_{table}=5$ m with the corresponding resistivity distribution.

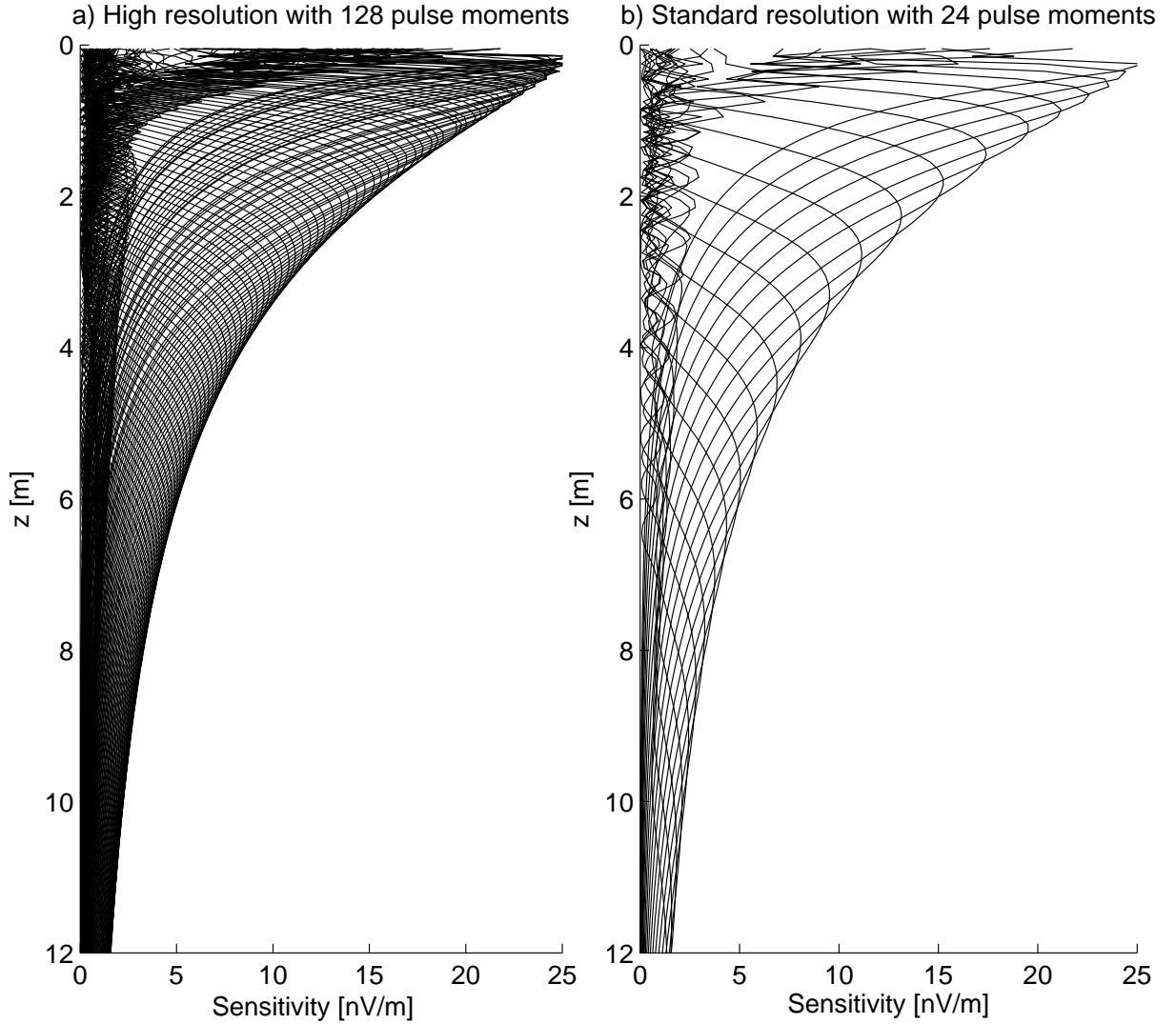


Figure 7.11: Sensitivity functions of the simulated MRS measurements above a water table at 5-m depth, calculated for a figure-eight loop with 10-m diameter, for (a) 128 and (b) 24 number of pulse moments in the range of 3.0 to 1400 Ams.

This time, the measurement was simulated with 24 pulse moments, which is a usual number for common MRS soundings. In Figure 7.11 the resulting vertical spatial coverage of this measurement is compared with the simulation using 128 pulse moments. The BCP inversion was applied with S_R and h_0 as *a priori* information to the resulting synthetic sounding curves. In doing so, the configuration of the numerical experiment was the same as for the data in Figure 7.10. Figure 7.12 shows the results of the λ estimation for the simulations with 24 pulse moments. Compared to the data in Figure 7.10c and 7.10d, the reliable range for the λ estimation is decreased to about 1.1; that is, for $\lambda > 1.1$, large

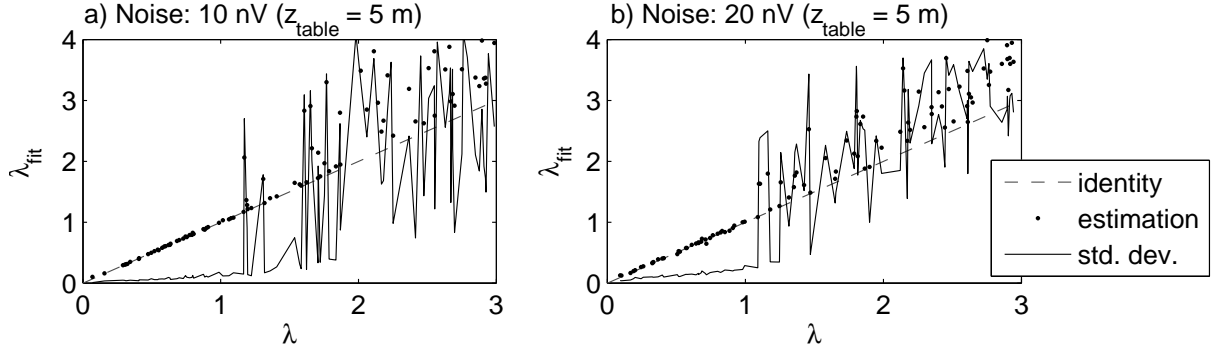


Figure 7.12: Comparison of the mean values of the inverted BC parameter λ (y-axes) and the input value for λ (x-axes), which was varied randomly within the range $0.01 < \lambda < 3$ (dots). The parameter h_0 was also varied randomly within the range $0.01 < h_0 < 1$, but it was held constant during the inversion; S_R was set to 0. The water table z_{table} was determined at 5 m. The noise level of the sounding curves was set to (a) 10 nV and (b) 20 nV, respectively. For each noise level, 100 individual models were investigated. The solid lines represent the standard deviations for each parameter after 100 runs (only the noise was varied 100 times for each model). The dashed lines denote the identity for orientation.

uncertainties of up to 200% occur. I conclude that a reliable application of the BCP inversion requires a number of pulse moments about 3 to 5 times larger than usual in quite a small range. Otherwise, an adequate resolution cannot be realized for discovering the capillary fringe.

7.3.3 Real data example from test field Nauen

The area of investigation is the well-known test field Nauen (Yaramanci et al., 2002; Goldbeck, 2002), which is about 50 km west of Berlin, Germany. The site exhibits a geological situation that is characteristic for the northern part of Germany: a sequence of Quaternary sediments, i.e., sand interbedded with cohesive glacial till and silt. The water table of the test field varies with the season within the range of about 1.6- to 2.0-m depth. Figure 7.13 shows a 1D sketch of the lithology as interpreted from well logging and borehole documentation compared to a standard MRS smooth inversion results.

The MRS investigation was performed with a circular loop (one turn) of 100-m diameter. The pulse sequence (Table 7.2) was designed with the focus on having the investigation depth be as large as possible to discover and characterize the aquifer properties. Aquicludes and aquitards appear in MRS results with reduced or vanishing water content. This is due to the dead time of the instrument (about 40 ms for the device used), which makes relaxation regimes with small T_2^* (i.e., small pore sizes) invisible. Regarding the vadose zone, we note that the resolution in the region of interest is much too low; the

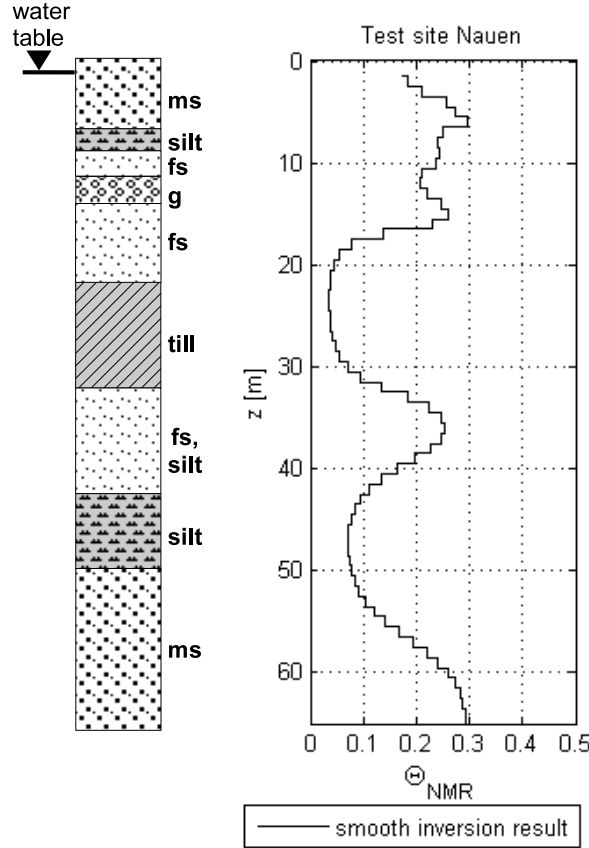


Figure 7.13: The lithology of the test site Nauen from borehole data compared to a typical smooth MRS inversion result showing the aquifer structure (MRS measurement configuration in Table 7.2).

water table cannot be identified at the correct depth, and the capillary fringe cannot be resolved. To focus the MRS investigation on the vadose zone and to get a better resolution near the water table, the MRS measurements were repeated with a changed measurement layout (Table 7.2). First, the loop size was reduced: A figure-eight loop (Trushkin et al., 1994) for signal detection (10-m diameter for each circle) and an additional reference loop (Walsh, 2008) for noise cancellation (square loop with 8-m side length) were used to optimize the signal-to-noise ratio (S/N). Second, the measurements were performed with a shortened dead time and, most important for our purpose here, with a large number pulse moments in a very small range (75 pulse moments in the range of 3 to 136.4 mAs). The measurements were not repeated for stacking. The S/N is quite low, with up to 3.5 in the saturated zone, which nevertheless allows a plausible interpretation thanks to the unusual high number of pulse moments. Legchenko and Shushakov (1998) have shown that a significant improvement of the resolution properties can be achieved even with low

Table 7.2: Comparison of typical MRS measurement parameters for aquifer characterization and vadose zone investigation (Nauen test site).

	Focus on aquifer structure	Focus on vadose zone
MRS device	NUMIS (Legchenko and Valla, 2002)	GMR (Walsh, 2008)
loop layout	circle	figure-eight
loop diameter [m]	100	10
number of turns	1	4
number of pulse moments	24	75
pulse duration [ms]	42	10
min. q [mAs]	31	3.0
max. q [mAs]	18070	136.4
dead time [ms]	40	17

S/N down to 2, if the number of pulse moments is high enough.

The actual water table z_{table} at the site of investigation was measured at a depth of 1.7 m in a borehole at a distance of 50 m. The kernel function was calculated with a resistivity of 3000 Ωm for the unsaturated and 280 Ωm for the saturated zone (Yaramanci et al., 2002). The resulting sensitivity functions are almost identical to the functions used for the synthetic study (see Figure 7.6). In Figure 7.14, inversion results with usual smoothness constraints are plotted. The regularization parameter w controlling the smoothness of the resulting water content distribution $\Theta_{NMR}(z)$ during the inversion routine is normally determined by an optimal compromise between a reliable data approximation and an adequate smoothness of the inversion result (Müller-Petke and Yaramanci, 2008). Figure 7.14 shows how the choice of different w affects the gradual increase of Θ_{NMR} near z_{table} . The slope of Θ_{NMR} decreases with increasing w . However, the root mean square (RMS) value as measure for the fit quality is almost identical (15.34 to 15.53 nV). Because an optimal choice of w always depends on the noise conditions of the data, a reliable reconstruction of the capillary fringe cannot be expected by using the usual smooth inversion.

The application of the time step inversion and the estimation of K_{rel} from T_2^* as described above must fail when no water is detected in the intermediate zone. The example at the Nauen test site exhibits this feature. The result of the two-layer time step inversion is shown in Fig.7.15. In contrast to the data example from Haldenslaben, the water in the intermediate zone here, also consisting of medium sand, cannot be detected with MRS. Consequently the T_2^* -time of the unsaturated zone cannot be determined. Instead, the BCP inversion is applied to the data example from the Nauen test site to reconstruct the capillary fringe using the BCP inversion. The benefit of this approach is the ability to predict K_{rel} from the pore-size-distribution index λ according to Equation 2.8.

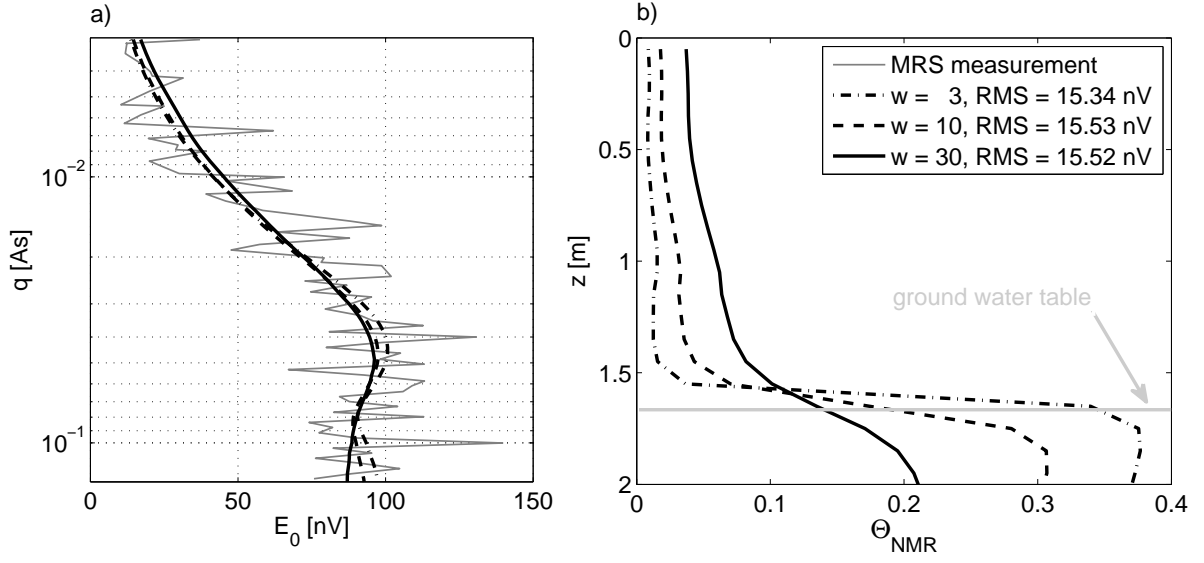


Figure 7.14: (a) MRS sounding curve (gray line) from the Nauen test site (MRS measurement configuration in Table 7.2) and approximations (black lines) from smooth inversions with different weighing parameters for model smoothness (w) and (b) the corresponding NMR water content distributions close to the water table.

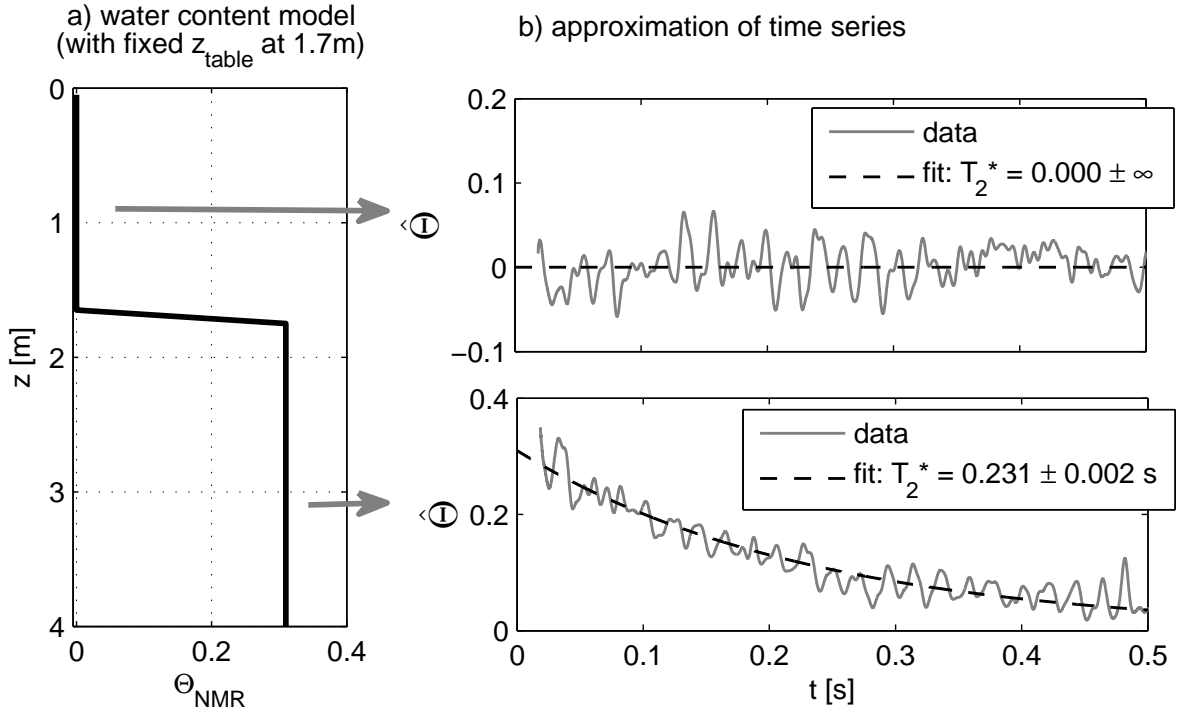


Figure 7.15: Result of the time step block inversion applied at the data from the Nauen test site with fixed water table at 1.7 m: (a) the water content block model, (b) the approximation of T_2^* for the unsaturated and the saturated zone.

Following the definition of the noise level in the synthetic study above, i.e., the statistical spread of the E_0 amplitudes, I use the RMS values from the smooth inversion results (about 15.5 nV, see Figure 7.14) as an estimation of the noise level for the real data. Regarding this noise level and recalling the numerical study above, the application of the BCP inversion with $S_R = 0$ and h_0 as *a priori* information is suggested. The parameter h_0 is set to 0.1 cm according to the laboratory data for the medium sand sample (ms in Figure 6.9). In Figure 7.16, the BCP inversion result is plotted. The pore-size-distribution index λ was approximated to be 1.49 ± 0.51 ; that is, the uncertainty of λ is in the same range as predicted by the numerical study (Figure 7.10). In Figure 7.16b, the representation of Θ as function of the BC parameters is depicted. The gray shaded zone represents the confidence interval of the water content distribution inside the capillary fringe. The confidence interval is calculated from the standard error of λ . The triangles depict WRC measurements of a core sample from the borehole taken at 0.7-m depth. These measurements were performed using a pressure plate apparatus (Warrik, 2003). Three different capillary pressure heads were applied: $h=63, 100$, and 200 cm, where the latter represents the field capacity range, i.e. the capillary pressure range at which the water is held in the pore space against the gravity force. The water

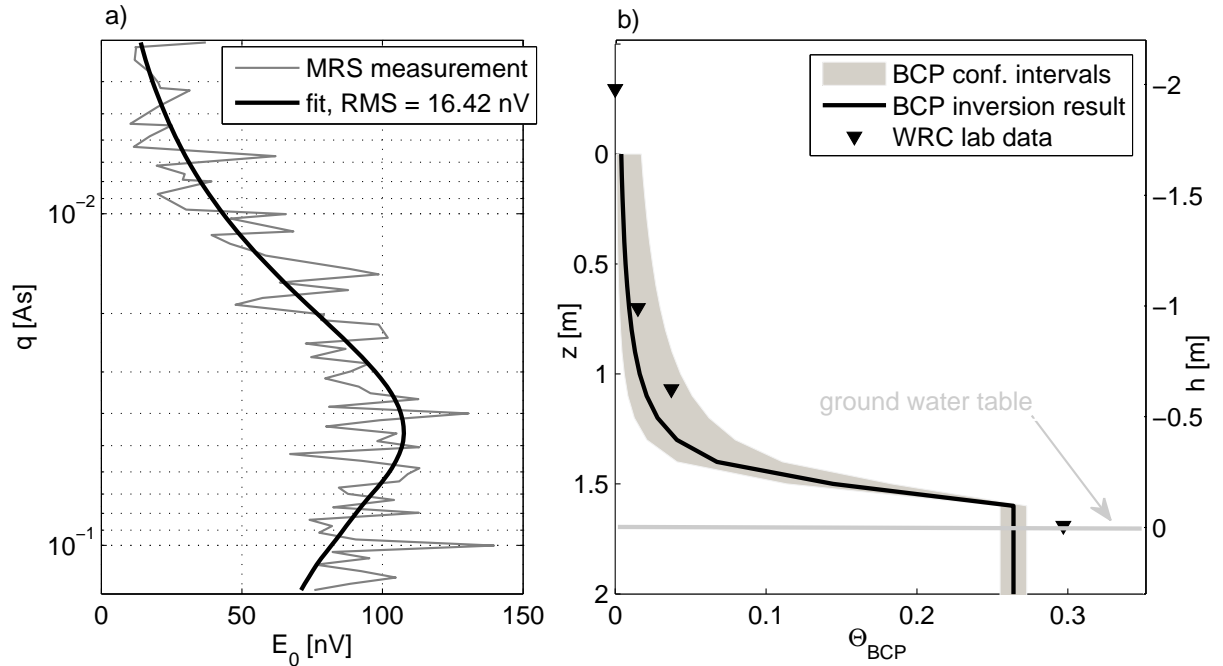


Figure 7.16: Result of the BCP inversion at the data example from the Nauen test site: (a) approximation (black line) of the sounding curve (gray line) and (b) water content model according to the BC representation of the capillary fringe (solid line) compared to laboratory WRC measurements for a core sample from 0.7-m depth (triangles).

content at $h=200$ cm ($\Theta(h = 200\text{cm})=4.9\%$) is interpreted as Θ_R to reduce the absolute Θ value to values representing the effective water content. The point at $h=0$ represents the saturated sample. The MRS prediction of the WRC is in good agreement with the laboratory result within the confidence interval. However, the effective water content at $h=0$ is slightly larger than the MRS water content for the saturated sand. This is caused by the fact that the MRS measurements at this location underestimate the effective water content due to additional dead-time-induced losses of the NMR signal.

The K_{rel} estimation calculated from the BCP inversion result, i.e., according to Equation 2.8, is depicted in Figure 7.17 as a function of S_E . For comparison, the $K_{rel}(S_E)$ curve for the sample at 0.7 m depth was calculated. This calculation was made by using the WRC parameters for this sample as predicted by the software ROSETTA (Schaap et al., 2001), a program able to reconstruct the WRC parameter from the texture information of a sample (see Chapter 2.4). The following sample parameters as found by analysis in the laboratory were used for the ROSETTA-based prediction: sand fraction: 93%, silt fraction: 7%, bulk dry density: 1.73 g/cm³, and $\Theta(h = 200\text{cm})=4.9\%$. The MRS-based estimation of K_{rel} matches the prediction by ROSETTA within the 95% confidence intervals. The discrepancy for $S_E > 0.2$ is smaller than half a decade.

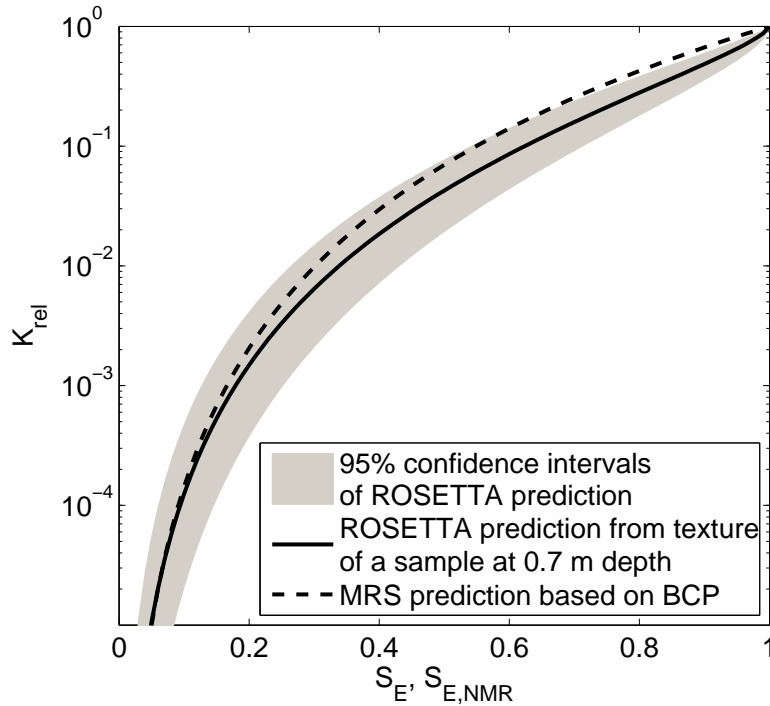


Figure 7.17: BCP-based prediction of $K_{rel}(S_E)$ (dashed line) compared to $K_{rel}(S_E)$ of a sample in 0.7-m depth (solid line).

7.4 Discussions and conclusions

A new inversion scheme for MRS was introduced that approximates the capillary fringe based on the Brooks-Corey model (BC model), which might be referred to as Brooks-Corey parameterization (BCP) inversion. In principle, the parameter space of this approach to be inverted is reduced to only four parameters: the water content of the saturated zone Θ_S , the residual water saturation in the unsaturated zone $S_R = \Theta_R/\Theta_S$ (where Θ_R is the residual water content), the pore-size-distribution index λ , and the air entry point h_0 . With a given water table z_{table} as a priori information, the BCP inversion allows a prediction of the relative hydraulic conductivity K_{rel} as a function of the saturation degree based on the inverted BC parameter λ (Equation 2.8). The application of this interpretation scheme for MRS is an important benefit for the non-invasive assessment of the water transport properties in the vadose zone. The feasibility of the approach was demonstrated with a real MRS data example.

However, numerical studies with synthetic data of a simulated measurement with a figure-eight loop of 10 m diameter show that under realistic noise conditions the parameters S_R and h_0 must be reliably estimated beforehand and then be held constant during the BCP inversion to stabilize the inversion of λ and Θ_S . According to the usual assumption that the NMR water content measured with MRS is an estimate of the effective water content (that is, the water content reduced by Θ_R), S_R can reliably be set to 0. On the other hand, the determination of h_0 in the field is a crucial limiting factor. For the real-data example in this study, an h_0 value found in the laboratory was used.

In the future, one should investigate whether h_0 can reliably be estimated from other non-invasive geophysical methods, such as ground-penetrating radar and/or geoelectrical measurements. Moreover, further numerical studies should be undertaken to investigate under which MRS measurement conditions it is possible to estimate λ and h_0 at the same time. The BCP inversion can be, in principle, be combined with common inversion concepts, such as smooth and block inversion strategies. In this way, the assessment of the aquifer structure can be enhanced by additional information about the vadose zone. However, for a broad application of the BCP inversion, special configurations of MRS measurements are required. First, arbitrary small pulse moments must be realized to shift the MRS sensitivity toward the very shallow subsurface. Second, an arbitrary number of pulse moments within a small range must be realized; that is, the gap between adjacent pulse moments must be decreased compared to standard MRS measurements. Both requirements are necessary to realize an adequate spatial coverage of the subsurface. However, user-defined configurations are still not implemented in commercially available MRS equipment.

As an alternative to the BCP inversion, the T_2^* times provided by MRS for the estimation of K_{rel} could be used. Under the condition that an adequate inversion scheme can provide reliable relaxation information from the vadose zone, an estimation of K_{rel} based on

the relaxation times would not be restricted on the range of the capillary fringe only; instead, the whole unsaturated zone, e.g. seepage water, could be characterized. In this study, with a real-data example was shown that the application of a blocky time step inversion with fixed water table (necessary *a priori* information) leads to a plausible estimation of K_{rel} from T_2^* for the unsaturated zone. In doing so, the subsurface was assumed to be a two-layer model distinguishing the saturated from the unsaturated zone. However, the MRS result for the shown data example could not be verified by laboratory investigations due to the lack of sample material. The main limitation of this approach is the fact that *a priori* information must be available that is usually not at hand in the field, the T_2 time of the saturated material and the dephasing index ν (see also Chapter 6.2.4). Strategies must be developed in the future that provide these parameters, e.g., by calibration or by estimation from a comprehensive data base for various lithological units. The development of such a data base is an important issue for future work.

Chapter 8

Conclusions

This work focusses on estimating the hydraulic conductivity and other effective hydraulic parameters of partially saturated soils from NMR methods applied on the laboratory and on the field scale, respectively. When applying various NMR measurements in the laboratory with different saturation degrees of the same material, the occurrence of new relaxation regimes with decreasing saturation in both the longitudinal (T_1) and the transverse (T_2) relaxation time distributions is observed. During desaturation, the relaxation time distributions are shifted towards smaller times compared to the distribution at saturation. The theoretical analysis of simple pore geometries has shown that this effect is caused by capillary-bound water that remains in the pore space during drainage as meniscoid or film water on the pore walls. The relaxation time of a water film on the pore walls linearly depends on the saturation degree of the pore (in the fast diffusion regime). In contrast, the assumption of an angular pore space with meniscoid water bounded in the corners of the pore leads to a square-root relationship between relaxation time and saturation. These considerations suggest the use of empirical models to avoid ambiguities, because, in practice, detailed information about the pore geometry is usually not at hand.

Laboratory and borehole NMR relaxometry applications in relatively high magnetic fields (at least 1000 times higher than the earth's magnetic field) are used to estimate the pore size distribution (PSD) of the saturated material. For soil physical purposes, the water retention curve (WRC), considered to be the cumulative PSD, is the key for predicting water transport processes when approximated adequately using soil physical models such as suggested by van Genuchten (1980) (VG) and by Brooks and Corey (1964) (BC). With artificial and natural soil samples, it was shown in this work that the approximation of the NMR relaxation data with the widely used VG model can lead to plausible estimates of the PSD index, but only for clay contents smaller than approximately 10%. For higher clay contents, the width of the PSD is underestimated by NMR compared to real WRC data as measured using a conventional pressure plate apparatus. This underestimation

8. Conclusions

increases with increasing clay content because of the higher sensitivity of NMR to the pore bodies compared to the pore-throat sensitivity of conventional WRC measurements. Thus, it is concluded that a plausible estimation of the unsaturated hydraulic conductivity from the cumulative NMR PSD is possible for sandy soils only.

Based on the BC model, an empirical approach has been developed, which relates the logarithmic mean of the T_2 distributions as a function of the saturation degrees to the PSD index. This approach allows for estimating the saturation dependend relative hydraulic conductivity K_{rel} , i.e., the ratio of the unsaturated and the saturated conductivities. It was verified by column experiments in the laboratory with sand of different grain sizes from fine to coarse. Regarding the field application of NMR, i.e., the magnetic resonance sounding (MRS) method working in the earth's magnetic field, the approach for estimating K_{rel} was modified for the use of the relaxation time T_2^* , which is measured in MRS by default. This modification is based on the assumption that the dephasing relaxation rate, which generally causes the difference between T_2 and T_2^* , also depends on the saturation of the material to be investigated. The dependence of the dephasing relaxation rate on the saturation degree is assumed to be a power law, and the corresponding exponent is referred to as the dephasing index.

The potential of T_2^* measured with earth's field NMR as a proxy for K_{rel} is demonstrated on the laboratory scale with column experiments, and its principle applicability for MRS is shown with a field example. However, the application of the approach demands *a priori* information: the T_2 relaxation time of the soil at saturation and the dephasing index, which limits its general applicability so far. Further research is necessary: the development of calibration strategies and/or the compilation of data bases for the missing parameters. Recent MRS research activities deal with the possibility to measure T_2 with MRS equipment in the field (Legchenko et al., 2010). Thus, it is expected that, at least, the parameter T_2 can be provided in the future directly by MRS measurements.

Alternatively to the approach of using the T_2^* times, an additional inversion approach for MRS is introduced, which directly parameterizes the capillary fringe in the subsurface by using the BC model (BCP). The BCP inversion approach uses the NMR signal amplitudes only, and is independent from the quality of the relaxation data, which is often a crucial limiting factor of MRS in practice. With the PSD index resulting from the BCP inversion, K_{rel} as a function of the saturation degree can be predicted under the assumption that the capillary fringe is in a state of equilibrium. The BCP approach was verified with column experiments in the laboratory and with a further field example, respectively.

Future approaches of using MRS to support *in situ* investigations of the vadose zone should include dynamic observations. In fact, the interpretation schemes in this work exhibit an important shortcoming: Based on steady state measurements they estimate parameters that finally describe dynamic processes. Regarding the overall issue, that is, the characterization of dynamic water flow processes in the vadose zone, the approaches

8. Conclusions

introduced here can just be considered to be in a state of 'getting-started'. The development of monitoring strategies and corresponding interpretation schemes, preferably combined with hydraulic modelings, must overcome this shortcoming in the future.

Bibliography

- Abragam, A. (1983). *Principles of Nuclear Magnetism*. Oxford University Press.
- Alali, F. (2006). Dependence of NMR and SIP parameters on clay content. Master's thesis, Berlin University of Technology.
- Alali, F., Müller, M., and Yaramanci, U. (2007). Dependence of NMR and SIP parameters on clay content. In *Tagungsband der 67. Jahrestagung der Deutschen Geophysikalischen Gesellschaft, Aachen, Germany*.
- Assouline, S. and Tartakovsky, D. M. (2001). Unsaturated hydraulic conductivity function based on a soil fragmentation process. *Water Resources Research*, 37 (5):1309 – 1312.
- Bird, N. R. A., Preston, A. R., Randall, E. W., Whalley, W. R., and Whitmore, A. P. (2005). Measurement of the size distribution of water-filled pores at different matric potentials by stray field nuclear magnetic resonance. *European Journal of Soil Science*, 56:135143.
- Bloch, F. (1946). Nuclear induction. *Physical Review*, 70(7):460 – 474.
- Boucher, M., Costabel, S., and Yaramanci, U. (2011). The detectability of water by NMR considering the instrumental dead time - a laboratory analysis of unconsolidated materials. *Near Surface Geophysics*, 9 (2):145 – 153.
- Brooks, R. H. and Corey, A. T. (1964). Hydraulic properties of porous media. *Hydrology Papers 3, Colorado State University*.
- Brownstein, K. R. and Tarr, C. E. (1979). Importance of classical diffusion in NMR studies of water in biological cells. *Physical Review A*, 19:2446–2453.
- Carr, H. and Purcell, E. (1954). Effects of diffusion on free precession experiments. *Physical Review*, 94:630.
- Chen, S., Liaw, H.-K., and Watson, A. T. (1994). Measurements and analysis of fluid saturation-dependent NMR relaxation and linebroadening in porous media. *Magnetic Resonance Imaging*, 12(2):201–202.

- Coates, G., Xiao, L., and Prammer, M. (1999). *NMR Logging Principles and Application*. Halliburton Energy Services.
- Costabel, S. and Yaramanci, U. (2011a). Relative hydraulic conductivity and effective saturation from earth’s field nuclear magnetic resonance - a method for assessing the vadose zone. *Near Surface Geophysics*, 9 (2):155 – 167.
- Costabel, S. and Yaramanci, U. (2011b). Relative hydraulic conductivity in the vadose zone from magnetic resonance sounding – Brooks-Corey parameterization of the capillary fringe. *Geophysics*, 76 (3):B1–B11.
- Cullen, S. J., Kramer, J. H., Everett, L. G., and Eccles, L. A. (1995). *Is Our Ground-Water Monitoring Strategy Illogical?* In F. L. Troise (ed): *Handbook of Vadose Zone Characterization and Monitoring*, pages 1 – 8. CRC Press.
- Davies, S. and Packer, K. J. (1990). Pore-size distributions from nuclear magnetic resonance spin-lattice relaxation measurements of fluid-saturated porous solids. I. Theory and simulation. *Journal of Applied Geophysics*, 67 (6):3163 —3170.
- Dunn, K., Bergman, D. J., and Latorraca, G. A. (2002). *Nuclear Magnetic Resonance – Petrophysical and Logging Applications*. Elsevier.
- Dunn, K., Latoracca, G. A., and Bergman, D. J. (1999). Permeability relation with other petrophysical parameters for periodic porous media. *Geophysics*, 64:470–478.
- Godefroy, S., Korb, J.-P., Fleury, M., and Bryant, R. G. (2001). Surface nuclear magnetic relaxation and dynamics of water and oil in macroporous media. *Physical Review E*, 64:021605.
- Goldbeck, J. (2002). Hydrogeophysical methods at the test-site Nauen - evaluation and optimisation. M.S. thesis, Berlin University of Technology.
- Hahn, E. (1950). Spin echoes. *Physical Review*, 80 (4):580 – 594.
- Hammecker, C., Barbiero, L., Boivin, P., Maeght, J. L., and Diae, E. H. B. (2004). A geometrical pore model for estimating the microscopical pore geometry of soil with infiltration measurements. *Transport in Porous Media*, 54:193–219.
- Haverkamp, R., Leij, F. J., Fuentes, C., Sciortino, A., and Ross, P. J. (2005). Soil water retention: I. introduction of a shape index. *Soil Science Society of America Journal*, 69:1881–1890.
- Hertrich, M. (2005). *Magnetic Resonance Sounding with separated transmitter and receiver loops for the investigation of 2D water content distributions*. PhD thesis, Technical University of Berlin.

- Hertzog, R. C., White, T. A., and Straley, C. (2007). Using NMR decay-time measurements to monitor and characterize DNAPL and moisture in subsurface porous media. *Journal of Environmental and Engineering Geophysics*, 12 (4):293 – 306.
- Hinnell, A. C., Ferre, T. P. A., Vrugt, J. A., Huismann, J. A., Moysey, S., Rings, J., and Kowalsky, M. B. (2010). Improved extraction of hydrologic information from geophysical data through coupled hydrogeophysical inversion. *Water Resources Research*, 46:W00D40.
- Howard, J. J. and Kenyon, W. E. (1992). Determination of pore size distribution in sedimentary rocks by proton magnetic resonance. *Marine and Petroleum Geology*, 9:139–145.
- Ioannidis, M. A., Chatzis, I., Lemaire, C., and Perunarkilli, R. (2006). Unsaturated hydraulic conductivity from nuclear magnetic resonance measurements. *Water Resources Research*, 42:W07201.
- Jaeger, F., Bowe, S., van As, H., and Schaumann, G. E. (2009). Evaluation of ^1H NMR relaxometry for the assessment of pore-size distribution in soil samples. *European Journal of Soil Science*, 60:1052 – 1064.
- Keating, K. and Knight, R. (2007). A laboratory study to determine the effect of iron oxides on proton NMR measurements. *Geophysics*, 72:27–32.
- Keating, K. and Knight, R. (2008). A laboratory study of the effect of magnetite on NMR relaxation rates. *Journal of Applied Geophysics*, 66:188–196.
- Kenyon, W. E. (1997). Petrophysical principles of applications of NMR logging. *The Log Analyst*, pages 21–43.
- Kenyon, W. E., Howard, J. J., Sezginer, A., Straley, C., Matteson, A., Horkowitz, K., and Ehrlich, R. (1989). Pore-size distribution and NMR in microporous cherty sandstones. In *Proceedings of the 40th Annual Logging Symposium*, pages 1–24.
- Kleinberg, R. L. (1996). Utility of NMR T2 distributions, connection with capillary pressure, clay effect, and determination of the surface relaxivity parameter ρ_2 . *Magnetic Resonance Imaging*, 14:761–767.
- Kleinberg, R. L., Kenyon, W. E., and Mitra, P. P. (1994). Mechanism of NMR relaxation of fluids in rock. *Journal of Magnetic Resonance, Series A*, 108:206–214.
- Kowalsky, M. B., Finsterle, S., Peterson, J., Hubbard, S., Rubin, Y., Majer, E., Ward, A., and Gee, G. (2005). Estimation of field-scale soil hydraulic and dielectric parameters through joint inversion of GPR and hydrological data. *Water Resources Research*, 41:W11425.

- Kutilek, M. and Nielson, D. R. (1994). *Soil Hydrology*. Catena Verlag.
- Legchenko, A., Baltassat, J., Beauce, A., and Bernard, J. (2002). Nuclear magnetic resonance as a geophysical tool for hydrogeologists. *Journal of Applied Geophysics*, 50(1-2):21–46.
- Legchenko, A. and Shushakov, O. A. (1998). Inversion of surface NMR data. *Geophysics*, 63(1):75–84.
- Legchenko, A. and Valla, P. (2002). A review of the basic principles for proton magnetic resonance sounding measurements. *Journal of Applied Geophysics*, 50(1-2):3–19.
- Legchenko, A., Vouillamoz, J.-M., and Roy, J. (2010). Application of the magnetic resonance sounding method to the investigation of aquifers in the presence of magnetic materials. *Geophysics*, 75 (6):L91 – L100.
- Leij, F. J., Alves, W. J., van Genuchten, M. T., and Williams, J. R. (1996). Unsaturated Soil Hydraulic Database, UNSODA 1.0 User’s Manual. *Report EPA/600/R-96/095*, US Environmental Protection Agency, page 103.
- Levitt, M. H. (2002). *Spin Dynamics - Basics of Nuclear Magnetic Resonance*. John Wiley & Sons, LTD.
- Lubczynski, M. W. and Roy, J. (2003). Hydrogeological interpretation and potential of the new magnetic resonance sounding (MRS) method. *Journal of Hydrology*, 283(1-4):19–40.
- MathWorks, T. (2007). *Optimization toolbox user’s guide for use with MATLAB*.
- Mattea, C., Kimmich, R., Ardelean, I., Wonorahardjo, S., and Farrher, G. (2004). Molecular exchange dynamics in partially filled microscale and nanoscale pores of silica glasses studied by field-cycling nuclear magnetic resonance relaxometry. *Journal of Chemical Physics*, 121 (21):10648–10656.
- McCall, K. R., Johnson, D. L., and Guyer, R. A. (1991). Magnetization evolution in connected pore systems. *Physical Review B*, 44 (14)(14):7344–7355.
- Meiboom, S. and Gill, D. (1958). Compensation for pulse imperfections in Carr-Purcell NMR experiments. *Review of Scientific Instruments*, 29:688.
- Melton, B. F. and Pollak, V. L. (2002). Condition for adiabatic passage in the earth’s-field nmr technique. *Journal of Magnetic Resonance*, 158:15 – 22.
- Michel, D. (1981). *Grundlagen und Methoden der kernmagnetischen Resonanz*. Akademie-Verlag Berlin.

- Mohnke, O. and Klitzsch, N. (2010). Microscale simulations of NMR relaxation in porous media considering internal field gradients. *Vadose Zone Journal*, 9:846 – 857.
- Mohnke, O. and Yaramanci, U. (2002). Smooth and block inversion of surface NMR amplitudes and decay times using simulated annealing. *Journal of Applied Geophysics*, 50:163–177.
- Mohnke, O. and Yaramanci, U. (2005). Forward modeling and inversion of MRS relaxation signals using multi-exponential decomposition. *Near Surface Geophysics*, 3:165–185.
- Mohnke, O. and Yaramanci, U. (2008). Pore size distributions and hydraulic conductivities of rocks derived from magnetic resonance sounding relaxation data using multi-exponential decay time inversion. *Journal of Applied Geophysics*, 66:73–81.
- Morel-Seytoux, H. J., Meyer, P. D., Nachabe, M., Touma, J., van Genuchten, M. T., and Lenhard, R. J. (1996). Parameter equivalence for the Brooks-Corey and van Genuchten soil characteristics: Preserving the effective capillary drive. *Water Resources Research*, 32 (5):1251 – 1258.
- Mualem, Y. (1976). A new model for predicting the hydraulic conductivity of unsaturated porous media. *Water Resources Research*, 12:513–522.
- Müller, M., Kooman, S., and Yaramanci, U. (2005). Nuclear magnetic resonance (NMR) properties of unconsolidated sediments in field and laboratory. *Near Surface Geophysics*, 3(4):275–286.
- Müller-Petke, M. (2009). *Extended use of Magnetic Resonance Sounding datasets - QT inversion and resolution studies*. PhD thesis, Berlin University of Technology.
- Müller-Petke, M. and Yaramanci, U. (2008). Resolution studies for magnetic resonance sounding (MRS) using the singular value decomposition. *Journal of Applied Geophysics*, 66(3-4):165–175.
- Müller-Petke, M. and Yaramanci, U. (2010). QT inversion - comprehensive use of the complete surface nmr data set. *Geophysics*, 75 (4):WA 199 – WA 209.
- Nemes, A., Wösten, J. H. M., and Lilly, A. (2001). *Development of soil hydraulic pedo-transfer functions on a European scale: their usefulness in the assessment of soil quality*. In: D. E. Stott, R. H. Mohtar and G.C. Steinhardt (eds). *Sustaining the Global Farm - Selected papers from the 10th International Soil Conservation Organization Meeting.*, pages 541 – 549. International Soil Conservation Organization in cooperation with the USDA-ARS National Soil Erosion Research Laboratory and Purdue University.

- Peters, A. and Durner, W. (2006). Improved estimation of soil water retention characteristics from hydrostatic column experiments. *Water Resources Research*, 42:W11401.
- Ransohoff, T. C. and Radke, C. J. (1988). Laminar flow of a wetting liquid along the corners of a predominantly gas-occupied noncircular pore. *Journal of Colloid and Interface Science*, 121 (2):392 – 401.
- Roy, J. and Lubczynski, M. W. (2005). MRS multi-exponential decay analysis: aquifer poresize distribution and vadose zone characterization. *Near Surface Geophysics*, 3(4):287–298.
- Rucker, D. F. and Ferre, T. P. A. (2004). Parameter estimation for soil hydraulic properties using zero-offset borehole radar: Analytical method. *Soil Science Society of America Journal*, 68:1560 – 1567.
- Saxton, K. E. and Rawls, W. J. (2006). Soil water characteristic estimates by texture and organic matter for hydrologic solutions. *Soil Scientific Society of America Journal*, 70:1569–1578.
- Schaap, M. G., Leij, F. J., and van Genuchten, M. T. (2001). Rosetta: a computer program for estimating soil hydraulic parameters with hierarchical pedotransfer functions. *Journal of Hydrology*, 251:163 – 176.
- Schindler, U., Durner, W., von Unold, G., Mueller, L., and Wieland, R. (2010). The evaporation method: Extending the measurement range of soil hydraulic properties using the air-entry pressure of the ceramic cup. *Journal of Plant Nutrition and Soil Science*, 173 (4):563 – 572.
- Schirov, M. D., Legchenko, A., and Creer, G. (1991). A new direct non-invasive groundwater detection technology for Australia. *Exploration Geophysics*, 22:333–338.
- Schlumberger (1997). How to use borehole nuclear magnetic resonance. *Oilfield Review*.
- Schönwiese, C. D. (2000). *Praktische Statistik für Meteorologen und Geowissenschaftler*. Gebrüder Borntraeger, Berlin-Stuttgart, Germany.
- Seevers, D. (1966). A nuclear magnetic method for determining the permeability of sandstones. *Transactions SPWLA*, Paper L.
- Steenhuis, T. S., Parlange, J. Y., and Aburime, S. A. (1995). *Preferential Flow in Structured and Sandy Soils: Consequences for Modeling and Monitoring*. In F. L. Troise (ed): *Handbook of Vadose Zone Characterization and Monitoring*., pages 61 – 77. CRC Press.
- Stephens, D. B. (1996). *Vadose Zone Hydrology*. CRC Press.

- Tannus, A. and Garwood, M. (1997). Adiabatic pulses. *NMR in Biomedicine*, 10:423 – 434.
- Torrey, H. C. (1949). Transient nutations in nuclear magnetic resonance. *Physical Review*, 76 (8)(8):1059–1068.
- Trushkin, D., Shushakov, O. A., and Legchenko, A. (1994). The potential of a noise-reducing antenna for surface NMR groundwater surveys in the earth’s magnetic field. *Geophysical Prospecting*, 42:855–862.
- Tuller, M. and Or, D. (2002). Unsaturated hydraulic conductivity of structured porous media: A review of liquid configuration-based models. *Vadose Zone Journal*, 1:14–37.
- Tuller, M., Or, D., and Dudley, L. M. (1999). Adsorption and capillary condensation in porous media: Liquid retention and interfacial configurations in angular pores. *Water Resources Research*, 35 (7):1949–1964.
- van Genuchten, M. (1980). A closed-form equation for predicting the hydraulic conductivity of unsaturated soils. *Soil Science Society of America Journal*, 44:892–898.
- Vereecken, H. (1995). Estimating the unsaturated hydraulic conductivity from theoretical models using simple soil properties. *Geoderma*, 65:81–92.
- Volokitin, Y., Looyestijn, W. J., Slijkerman, W. F. J., and Hofman, J. P. (2001). A practical approach to obtain primary drainage capillary pressure curves from NMR core and log data. *Petrophysics*, 42 (4):334–343.
- Šimůnek, J. and van Genuchten, M. T. (1999). *Characterization and Measurement of the Hydraulic Properties of Unsaturated Porous Media*, chapter Using the Hydrus-1D and Hydrus-2D codes for estimating unsaturated soil hydraulic and solute transport parameters, pages 1523–1536. University of California, Riverside, CA.
- Šimůnek, J., Šejna, M., Saito, H., Sakai, M., and van Genuchten, M. T. (2009). *The HYDRUS-1D software package for simulating the one-dimensional movement of water, heat and multiple solutes in variably-saturated media, Version 4.0: HYDRUS Software Series 3*. Department of Environmental Sciences, University of California Riverside.
- Walbrecker, J., Hertrich, M., and Green, A. G. (2009). Accounting for relaxation processes during the pulse in surface NMR data. *Geophysics*, 74 (6):G27 – G34.
- Walsh, D. (2008). Multi-channel surface NMR instrumentation and software for 1D/2D groundwater investigations. *Journal of Applied Geophysics*, 66(3-4):140–150.
- Warrik, A. W. (2003). *Soil Water Dynamics*. Oxford University Press.

- Weichman, P. B., Lun, D. R., Ritzwoller, M. H., and Lavelly, E. M. (2002). Study of surface nuclear magnetic resonance inverse problems. *Journal of Applied Geophysics*, 50(1-2):129–147.
- Wierenga, P. J. (1995). *Water and Solute Transport and Storage*. In F. L. Troise (ed): *Handbook of Vadose Zone Characterization and Monitoring*., pages 41 – 60. CRC Press, Inc.
- Wösten, J. H. M., Pachepsky, Y. A., and Rawls, W. J. (2001). Pedotransfer functions: bridging the gap between available basic soil data and missing soil hydraulic characteristics. *Journal of Hydrology*, 251:123 – 150.
- Yaramanci, U. and Hertrich, M. (2006). *Magnetic Resonance Sounding*. In R. Kirsch (ed): *Groundwater Geophysics - A Tool for Hydrogeology*., pages 253–273. Springer-Verlag.
- Yaramanci, U., Lange, G., and Hertrich, M. (2002). Aquifer characterisation using surface NMR jointly with other geophysical techniques at the Nauen/Berlin test site. *Journal of Applied Geophysics*, 50(1-2):47–65.
- Yaramanci, U., Lange, G., and Knödel, K. (1999). Surface NMR within a geophysical study of an aquifer at Haldensleben (Germany). *Geophysical Prospecting*, 47:923–943.
- Yaramanci, U. and Müller-Petke, M. (2009). Surface nuclear magnetic resonance a unique tool for hydrogeophysics. *The leading edge*, 28 (10):1240–1247.
- Zhu, J. and Mohanty, B. P. (2002). Upscaling of soil hydraulic properties for steady state evaporation and infiltration. *Water Resources Research*, 38 (9):1178.

Acknowledgements

I would like to express my gratitude to the following persons:

- Prof. Dr. Ugur Yaramanci, who supervised and supported this PhD thesis. His encouragements and suggestions guided me from the early fundamental ideas five years ago to the final state of this work. As head of the Department of Applied Geophysics of the Berlin University of Technology he always provided ideal working conditions, so I had an excellent start of my professional life there and, on the other hand, the opportunity to start a family at the same time.
- Prof. Dr. Reinhard Kirsch for his support and good will during our great team play at the Berlin University of Technology. His refreshing criticism and cheerfulness always inspired me. What a shame that he doesn't like my coffee.
- My colleague and friend Dr. Mike Mueller-Petke for his interest and joy on endless discussions and on good coffee. In particular, I am very grateful for his private lessons in inversion theory and his support in the development of the inverse Laplace software.
- Prof. Dr. Gerd Wessolek and Michael Facklam from the Department of Standortkunde und Bodenschutz of the Berlin University of Technology for providing me with the equipment to perform the water retention measurements.
- Dr. Ursula Noell and Dr. Uwe Meyer from the Federal Institute for Geosciences and Natural Resources for their support during the last months of writing this thesis.
- Dr. Marian Hertrich and Dr. Jan Walbrecker from the Institute of Geophysics of the ETH - Swiss Federal Institute of Technology, as well as Dr. Thomas Günther, Raphael Dlugosch and Mathias Ronczka from the Leibniz-Institute of Applied Geophysics Hannover for fruitful discussions about NMR in general and, in particular, constructive criticism on this thesis.
- Dr. Traugott Scheytt and Dr. Dirk Radny from the Department of Hydrogeology of the Berlin University of Technology for their interest in my work and for illuminating conversations about capillary forces and unsaturated flow. Special thanks to Dirk

Acknowledgements

for providing me with relevant literature and for his endurance in getting the books back.

- Dr. Andre Peters from the Department of Soil Science of the Berlin University of Technology for helpful discussions about the reliability of water retention models.
- My family for the unlimited mental support all the time. In particular, I want to thank my parents-in-law Barbara and Jörg-Peter Costabel for providing their garden as out-door NMR laboratory. Last but not least, I am deeply indebted to my wife Katja, a great modern woman, caring mother and self-assured scientist (in the making), knowing friend and verbal sparring partner, for giving me a home and bolstering me up.

Appendices

Appendix A

Appendix to Chapter 5

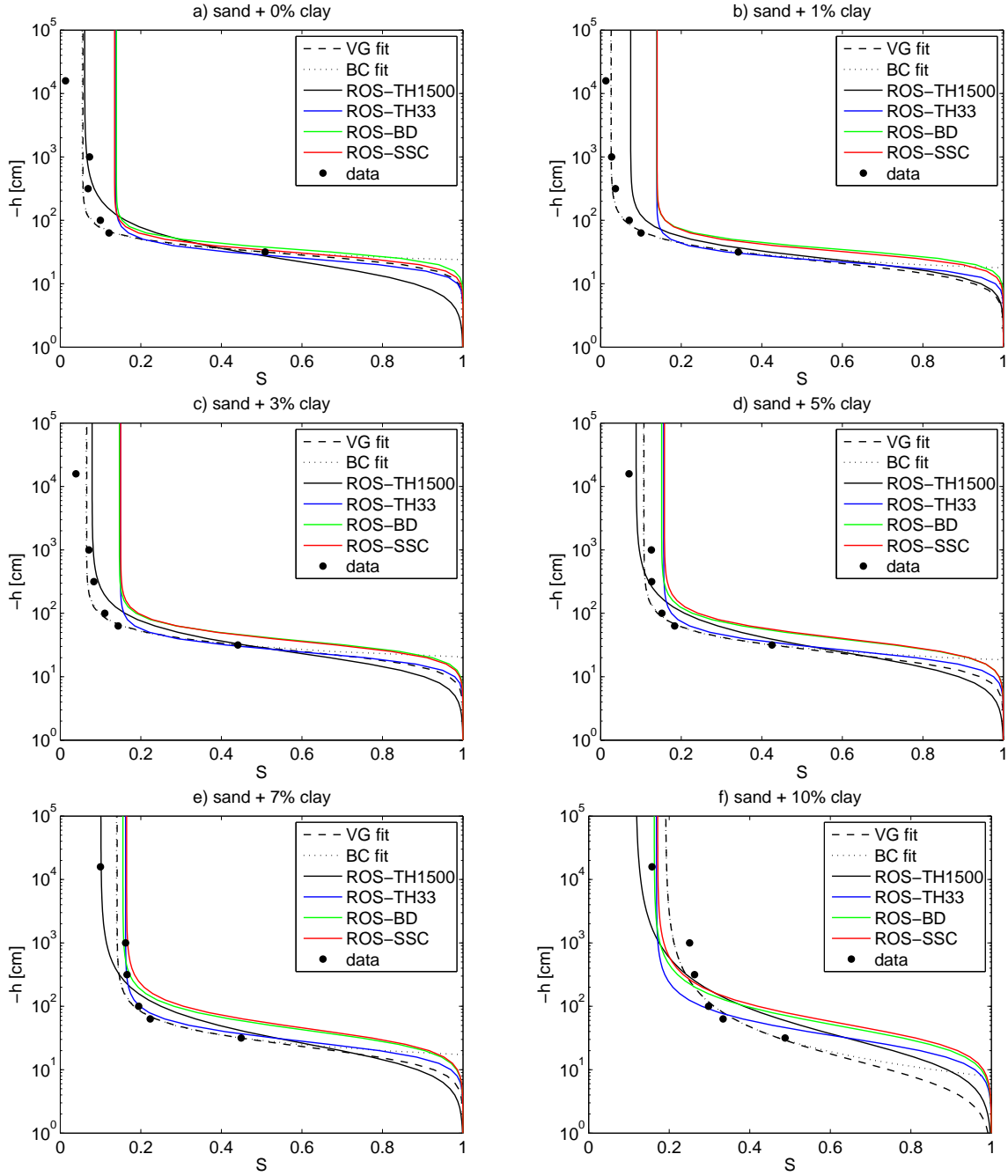


Figure A.1: WRC measurements (black circles) of artificial sand-clay mixtures and the corresponding approximations after van Genuchten (1980) (VG) and after Brooks and Corey (1964) (BC), for comparison: the WRC predictions by ROSETTA (Schaap et al., 2001) using the models ROS-TH1500, ROS-TH33, ROS-BD, and ROS-SSC, abbreviations are detailed in Table 2.1.

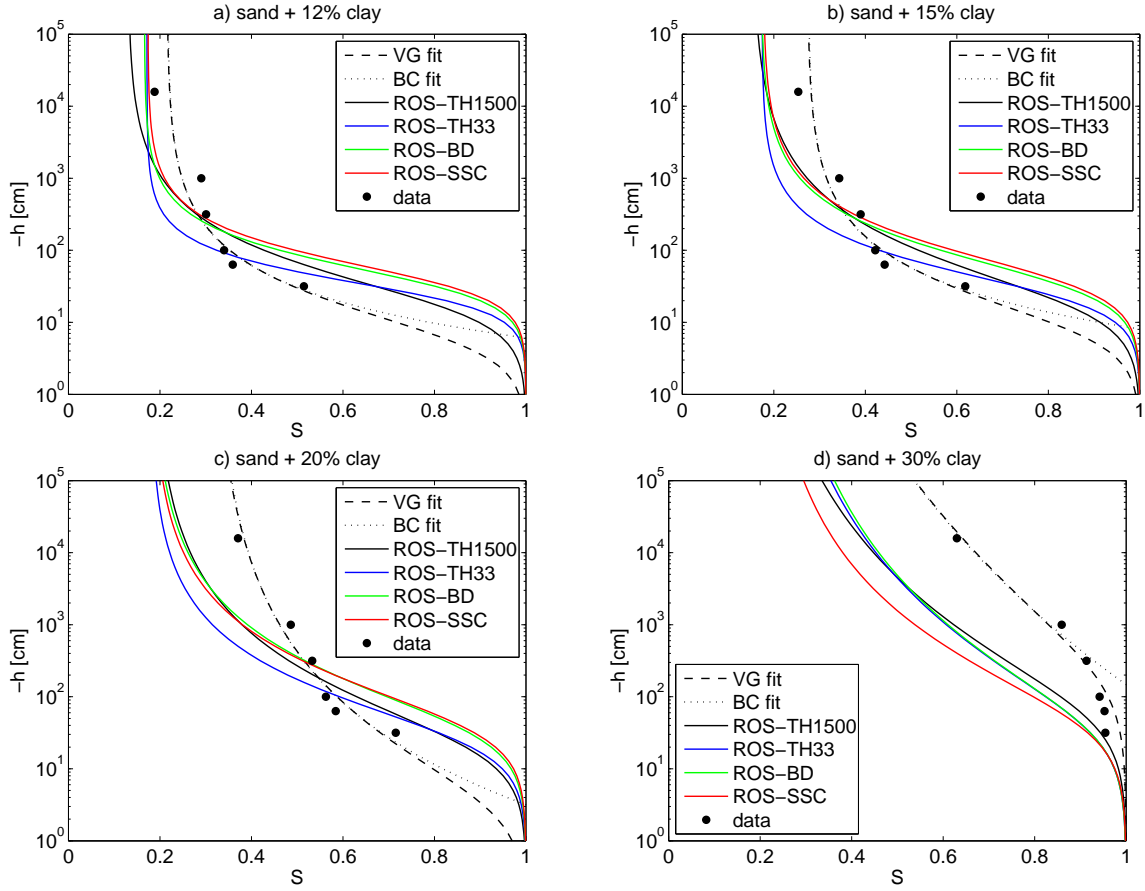


Figure A.2: WRC measurements (black circles) of artificial sand-clay mixtures and the corresponding approximations after van Genuchten (1980) (VG) and after Brooks and Corey (1964) (BC), for comparison: the WRC predictions by ROSETTA (Schaap et al., 2001) using the models ROS-TH1500, ROS-TH33, ROS-BD, and ROS-SSC, abbreviations are detailed in Table 2.1.

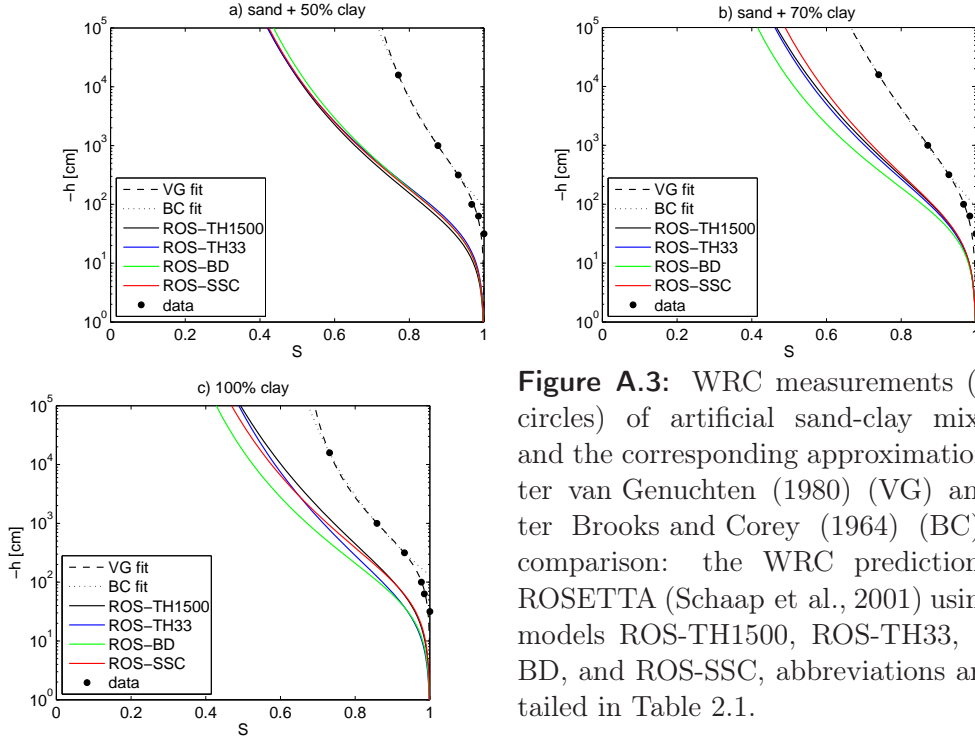


Figure A.3: WRC measurements (black circles) of artificial sand-clay mixtures and the corresponding approximations after van Genuchten (1980) (VG) and after Brooks and Corey (1964) (BC), for comparison: the WRC predictions by ROSETTA (Schaap et al., 2001) using the models ROS-TH1500, ROS-TH33, ROS-BD, and ROS-SSC, abbreviations are detailed in Table 2.1.

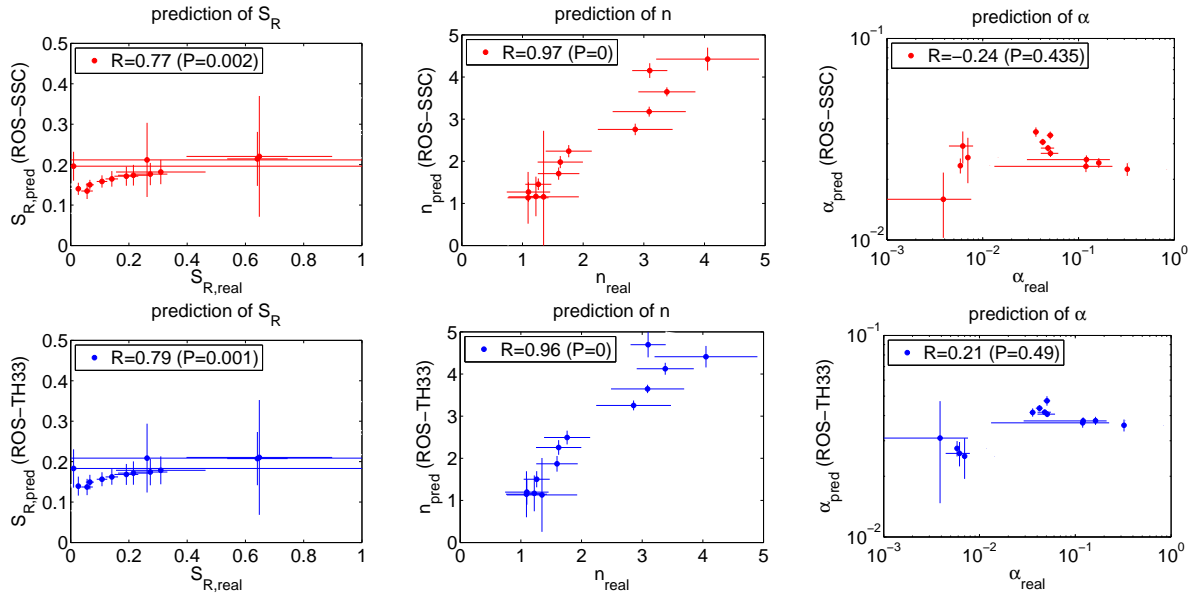


Figure A.4: VG parameters predicted by ROSETTA compared to the 'real' parameters as found by fitting the corresponding WRC measurements of artificial sand-clay mixtures, predictions with ROSETTA models ROS-SSC (top) and ROS-TH33 (bottom), abbreviations are detailed in Table 2.1.

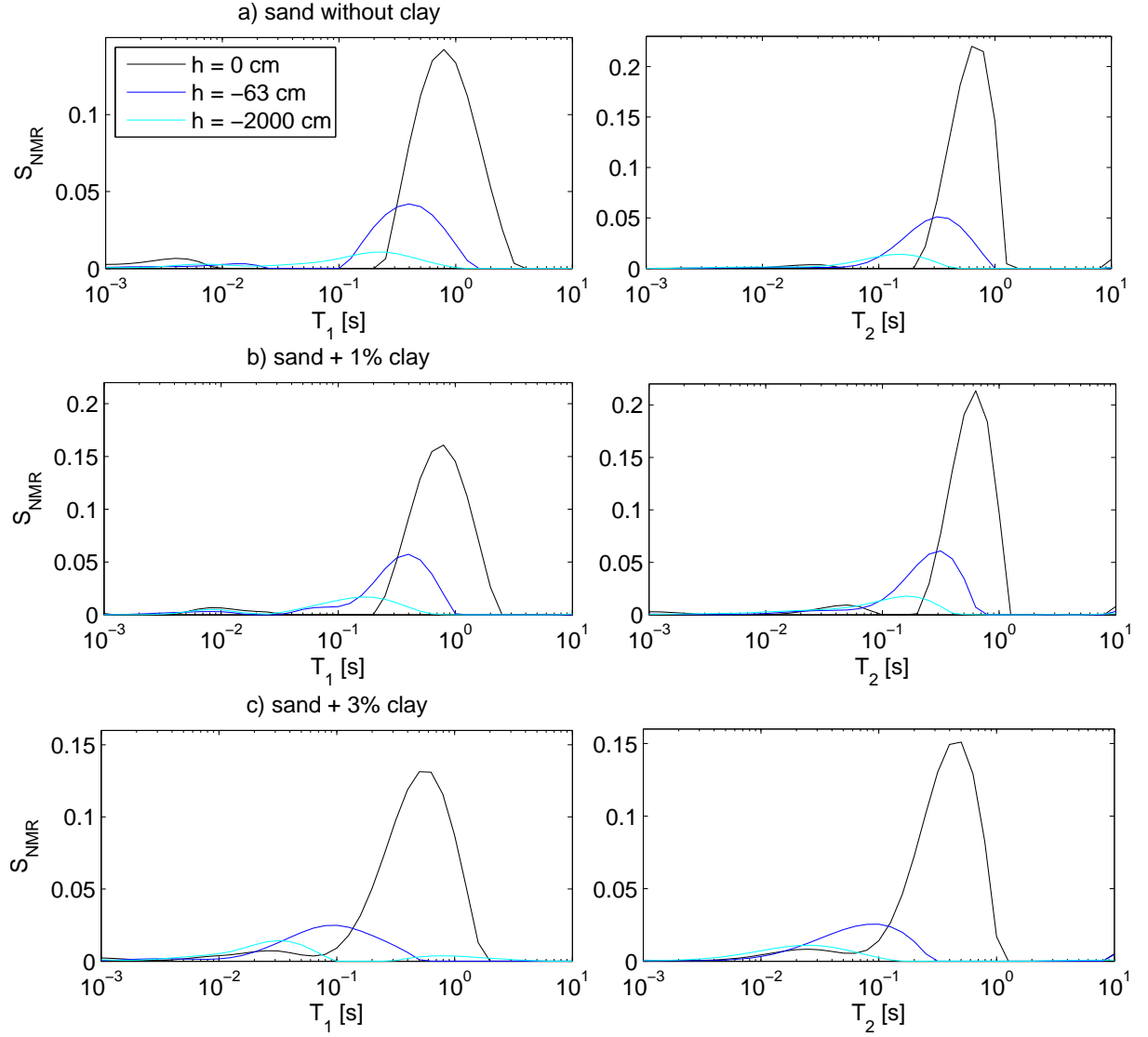


Figure A.5: NMR relaxation time distributions of artificial sand-clay mixtures at varying capillary pressure heads h , T_1 on the left and T_2 on the right hand side.

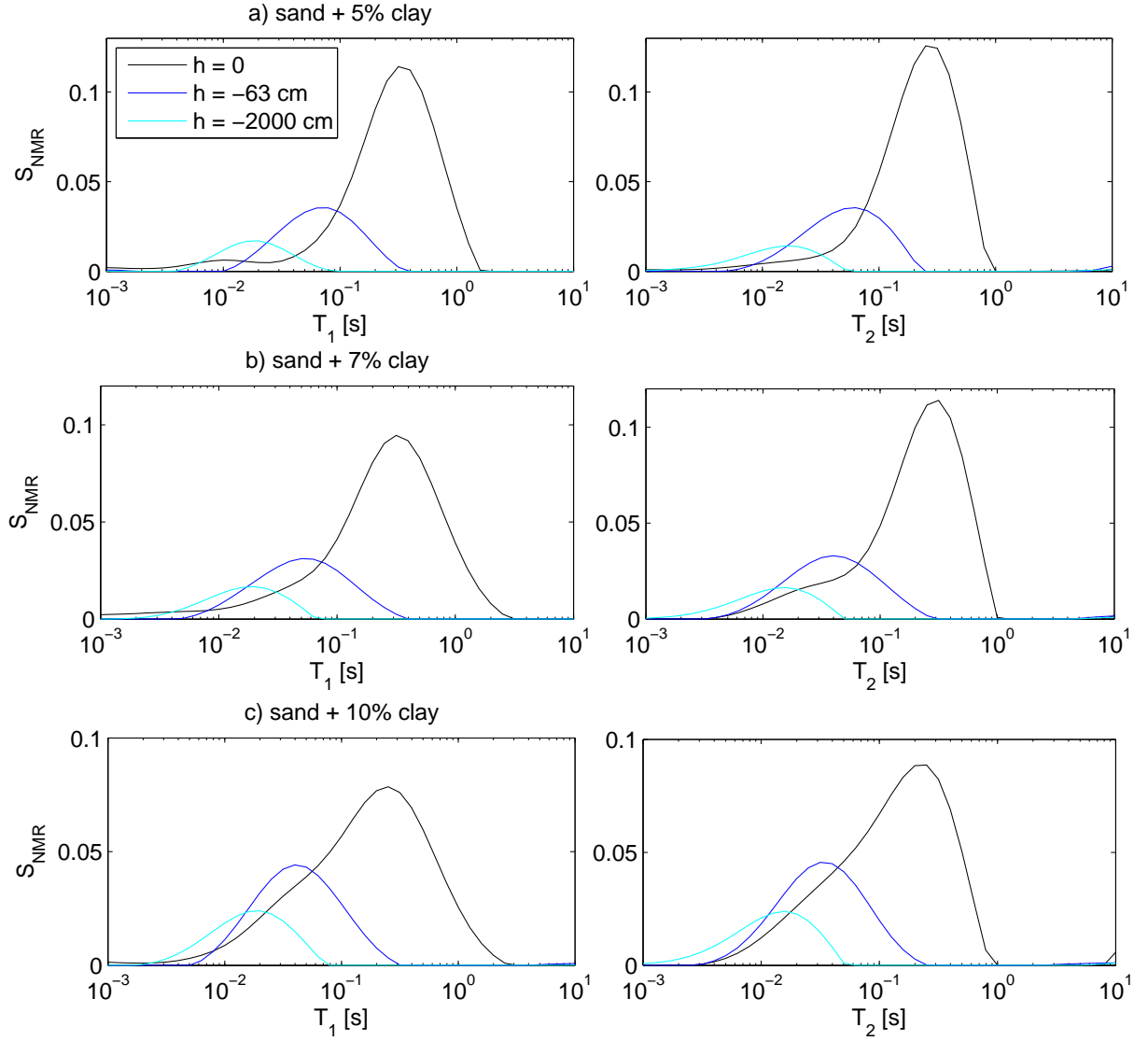


Figure A.6: NMR relaxation time distributions of artificial sand-clay mixtures at varying capillary pressure heads h , T_1 on the left and T_2 on the right hand side.

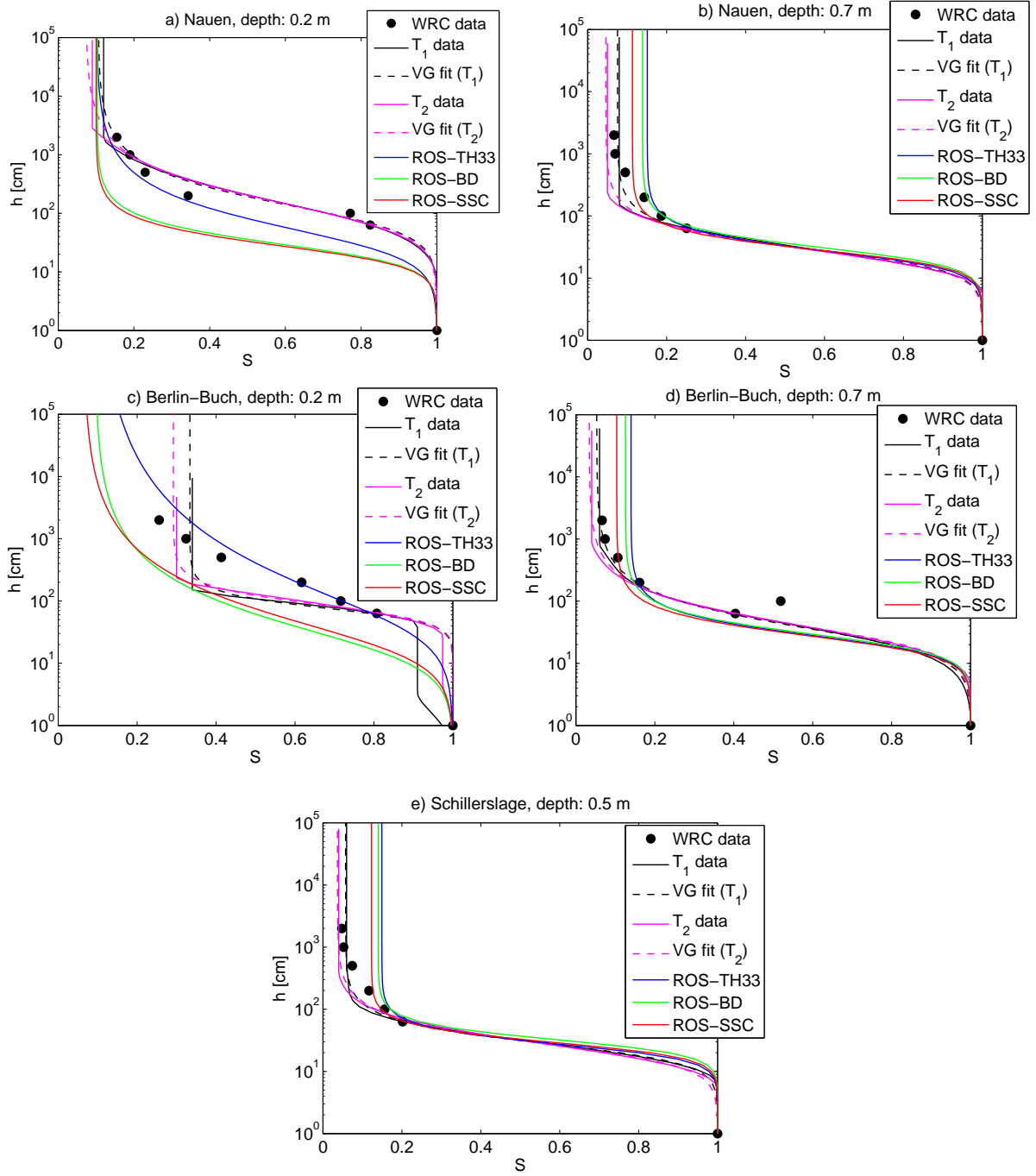


Figure A.7: WRC estimations from T_1 and T_2 distributions (black and magenta solid lines) and the corresponding fit after van Genuchten (1980) (black and magenta dashed lines) compared to WRC predictions by ROSETTA (Schaap et al., 2001) with prediction models ROS-SSC (red solid line), ROS-BD (green solid line), and ROS-TH33 (blue solid line), abbreviations are detailed in Tab2.1.

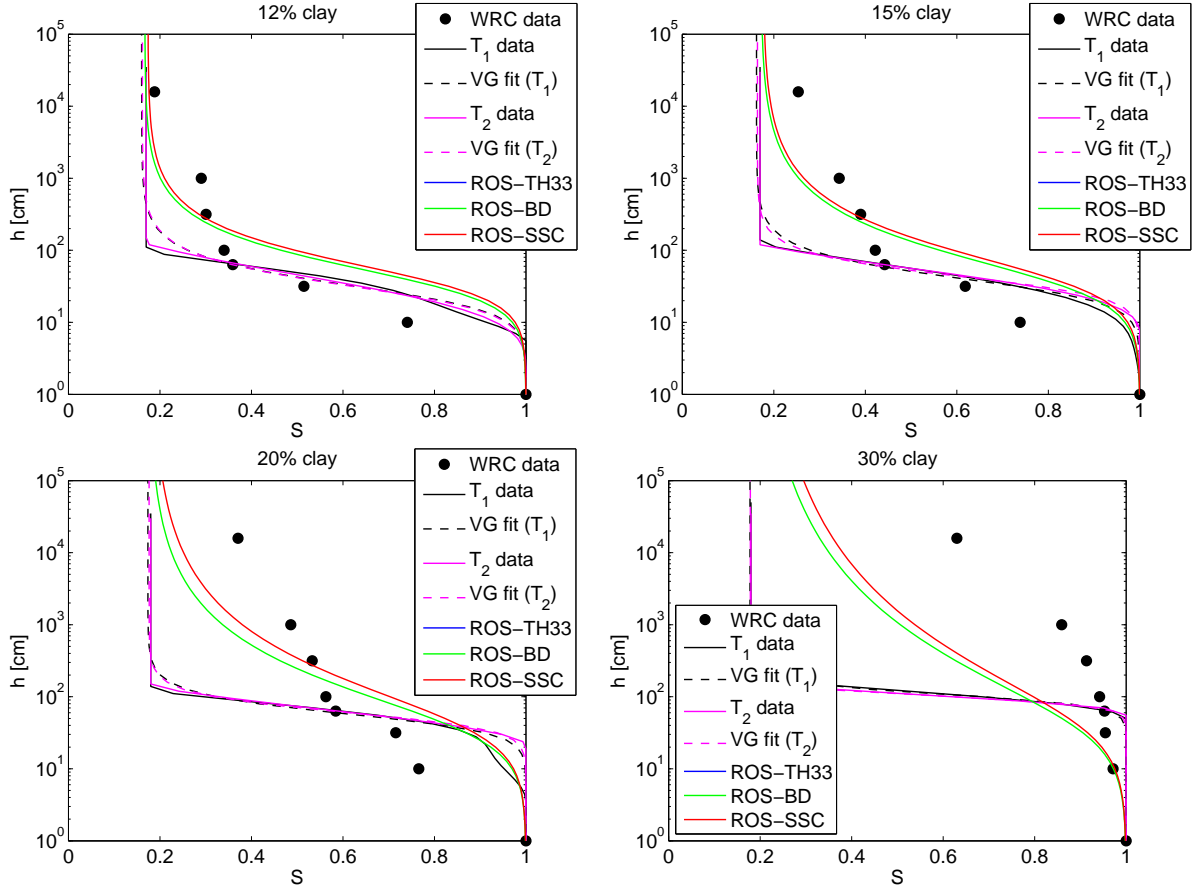


Figure A.8: WRC estimations from NMR T_1 and T_2 distributions (black and magenta solid lines) and the corresponding fit after van Genuchten (1980) of sand-clay mixtures from 12 to 30% CC compared to real WRC measurements (black circles) and WRC predictions by ROSETTA (Schaap et al., 2001) with prediction models ROS-TH33 (blue solid line), ROS-BD (green solid line) and ROS-SSC (red solid line), abbreviations are detailed in Tab2.1.

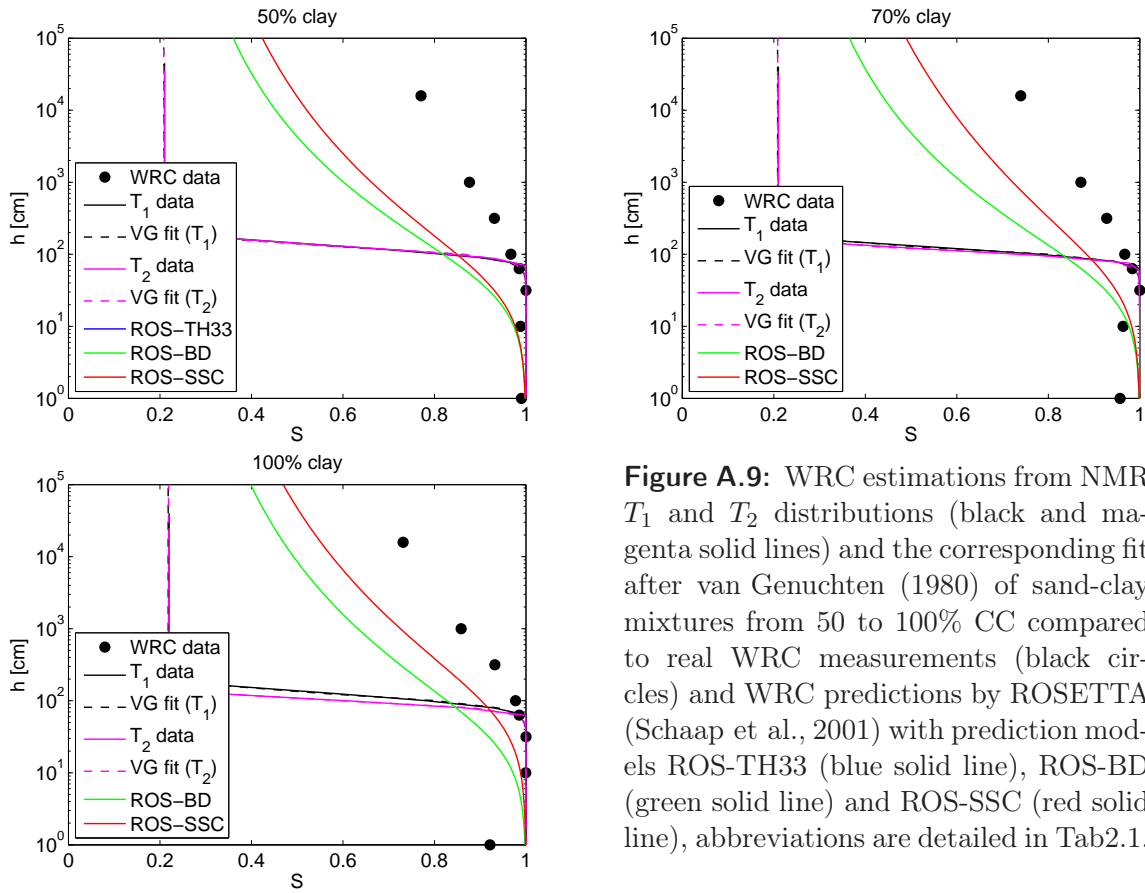


Figure A.9: WRC estimations from NMR T_1 and T_2 distributions (black and magenta solid lines) and the corresponding fit after van Genuchten (1980) of sand-clay mixtures from 50 to 100% CC compared to real WRC measurements (black circles) and WRC predictions by ROSETTA (Schaap et al., 2001) with prediction models ROS-TH33 (blue solid line), ROS-BD (green solid line) and ROS-SSC (red solid line), abbreviations are detailed in Tab2.1.

Appendix B

Appendix to Chapter 6

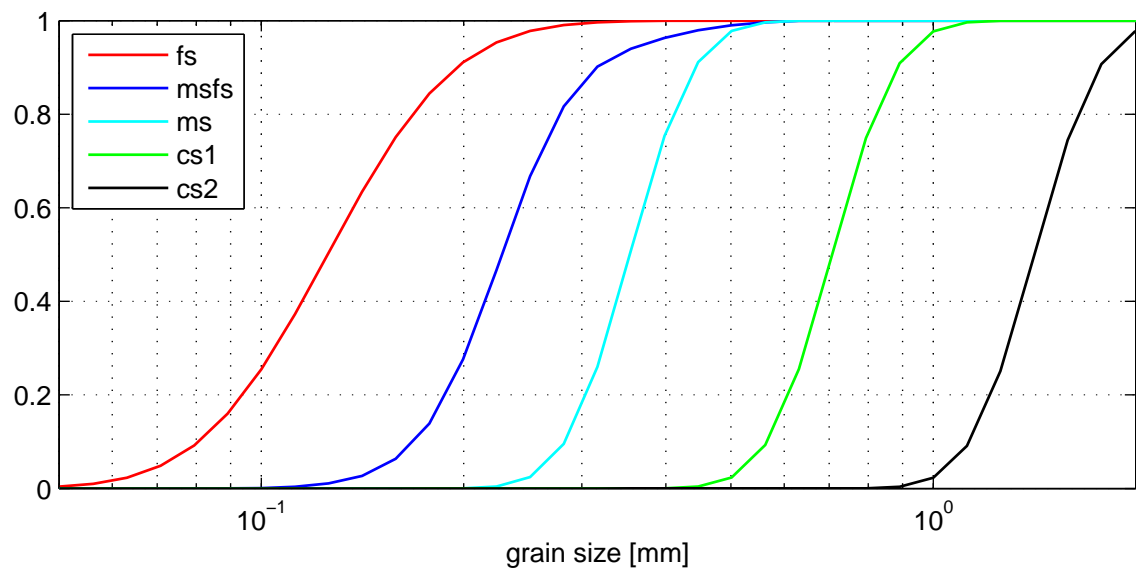


Figure B.1: Cumulative grain size distributions of the samples investigated with column experiments.

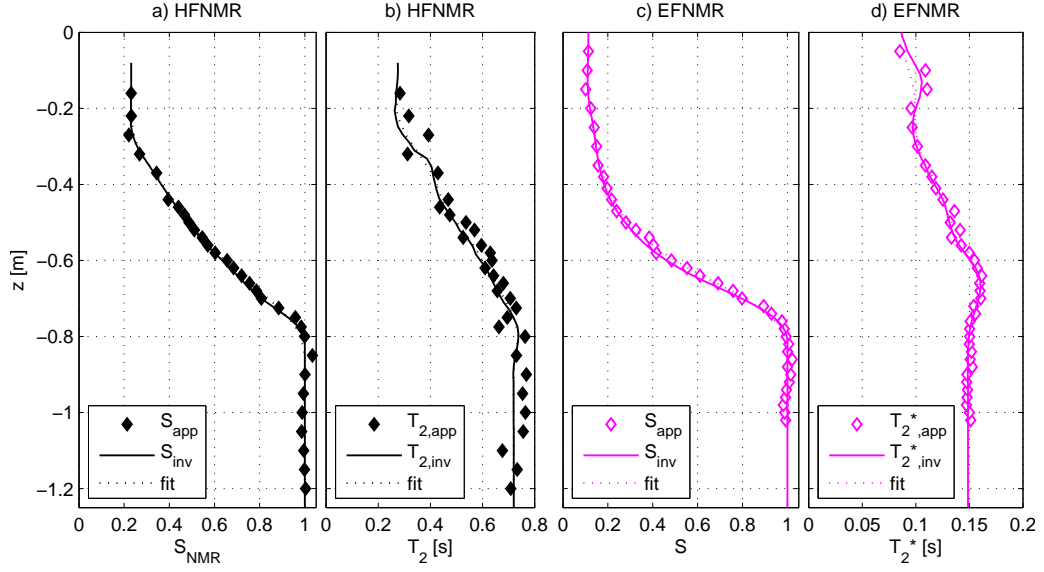


Figure B.2: Measured (S_{app} , $T_{2,app}$, and $T_{2,app}^*$) and inverted NMR results (S_{inv} , $T_{2,inv}$, and $T_{2,inv}^*$) for the fine sand sample fs, spatial distributions inside the column: HFNMR saturation degree (a) and T_2 times (b), EFNMR saturation degree (c) and T_2^* times (d).

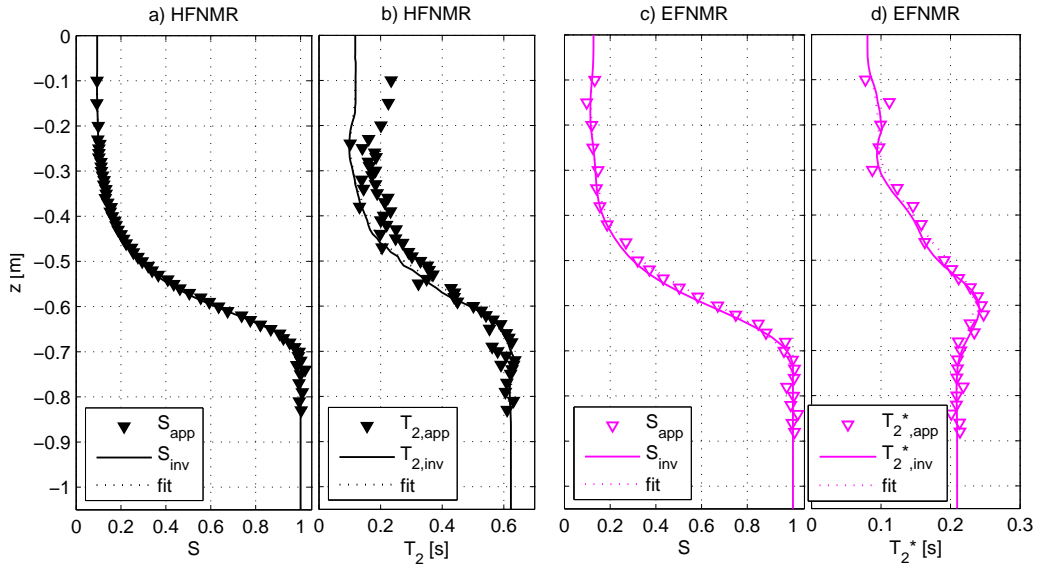


Figure B.3: Measured (S_{app} , $T_{2,app}$, and $T_{2,app}^*$) and inverted NMR results (S_{inv} , $T_{2,inv}$, and $T_{2,inv}^*$) for the medium and fine sand sample msfs, spatial distributions inside the column: HFNMR saturation degree (a) and T_2 times (b), EFNMR saturation degree (c) and T_2^* times (d).

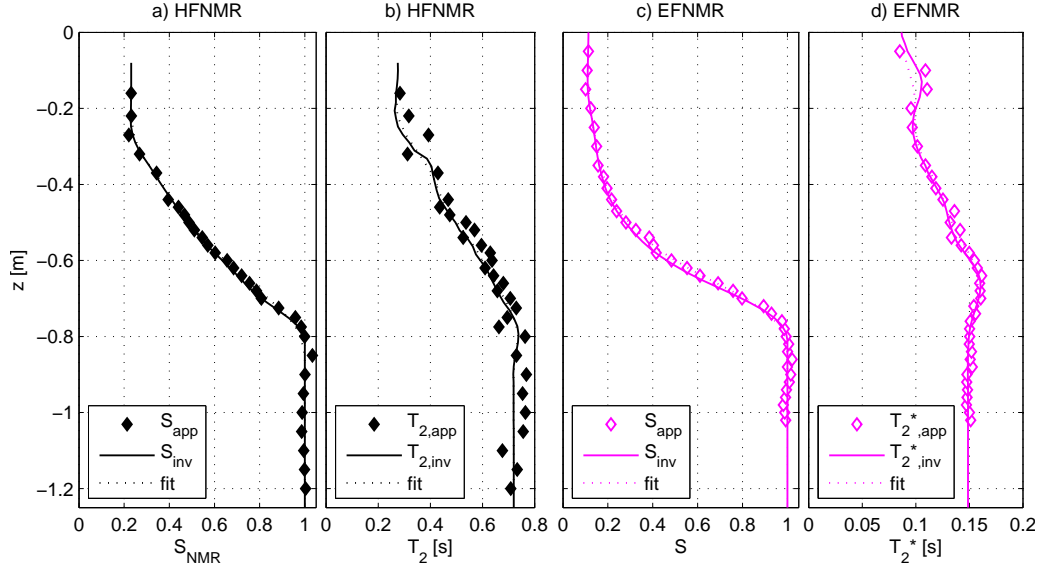


Figure B.4: Measured (S_{app} , $T_{2,app}$, and $T_{2,app}^*$) and inverted NMR results (S_{inv} , $T_{2,inv}$, and $T_{2,inv}^*$) for the medium sand sample ms, spatial distributions inside the column: HFNMR saturation degree (a) and T_2 times (b), EFNMR saturation degree (c) and T_2^* times (d).

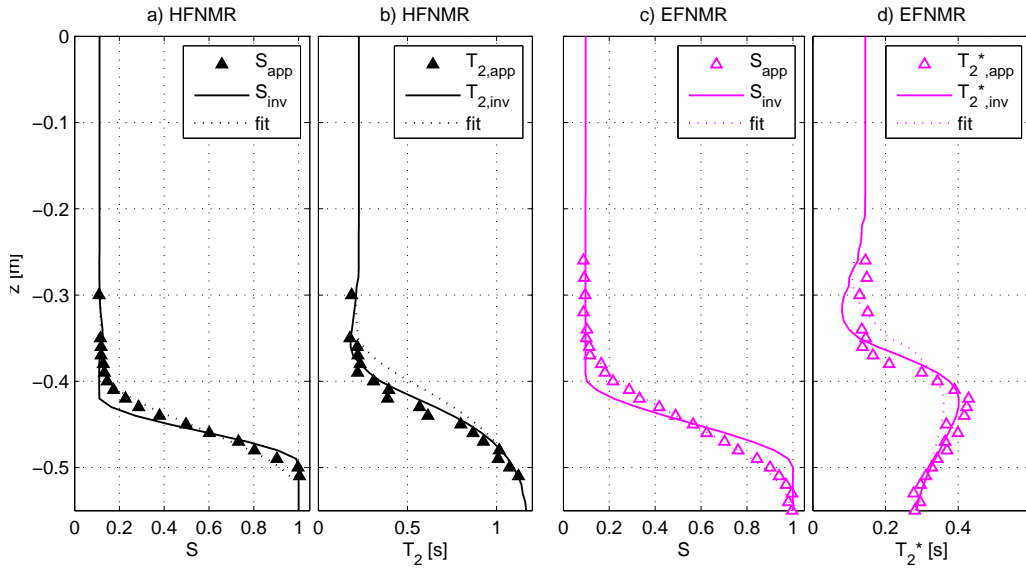


Figure B.5: Measured (S_{app} , $T_{2,app}$, and $T_{2,app}^*$) and inverted NMR results (S_{inv} , $T_{2,inv}$, and $T_{2,inv}^*$) for the coarse sand sample cs2, spatial distributions inside the column: HFNMR saturation degree (a) and T_2 times (b), EFNMR saturation degree (c) and T_2^* times (d).